Submitted to Physical Review

UCRL-19043
Preprint

cy. 2

RECEIVED
LAWRENCE
RADIATION LABORATORY

JUL 23 1969

LIBRARY AND
DOCUMENTS SECTION

ROTATING-FRAME NUCLEAR DOUBLE RESONANCE DYNAMICS: DIPOLAR FLUCTUATION SPECTRUM IN CaF_2

D. A. McArthur, E. L. Hahn, and R. E. Walstedt

July 1969

AEC Contract No. W-7405-eng-48

TWO-WEEK LOAN COPY

This is a Library Circulating Copy
which may be borrowed for two weeks.
For a personal retention copy, call
Tech. Info. Division, Ext. 5545

LAWRENCE RADIATION LABORATORY
UNIVERSITY of CALIFORNIA BERKELEY

cy. 2

UCRL-19043

DISCLAIMER

This document was prepared as an account of work sponsored by the United States Government. While this document is believed to contain correct information, neither the United States Government nor any agency thereof, nor the Regents of the University of California, nor any of their employees, makes any warranty, express or implied, or assumes any legal responsibility for the accuracy, completeness, or usefulness of any information, apparatus, product, or process disclosed, or represents that its use would not infringe privately owned rights. Reference herein to any specific commercial product, process, or service by its trade name, trademark, manufacturer, or otherwise, does not necessarily constitute or imply its endorsement, recommendation, or favoring by the United States Government or any agency thereof, or the Regents of the University of California. The views and opinions of authors expressed herein do not necessarily state or reflect those of the United States Government or any agency thereof or the Regents of the University of California.

UCRL-19043
Preprint

Rotating-Frame Nuclear Double Resonance Dynamics: Dipolar Fluctuation Spectrum in CaF_2**

by

D. A. McArthur*' and E. L. Hahn

Physics Department and Inorganic Materials Research
Division of Lawrence Radiation Laboratory,
University of California
Berkeley, California

and

R. E. Walstedt+

Bell Telephone Laboratories, Incorporated
Murray Hill, New Jersey

** Work supported in part by the National Science Foundation

* Now at Bell Telephone Laboratories, Incorporated, Holmdel, New Jersey.

' This work was submitted in partial fulfillment of the requirements for the Ph.D.

+ This work was initiated while the author was a Research Associate at the Physics Department, University of California, Berkeley, California.

ROTATING-FRAME NUCLEAR DOUBLE RESONANCE DYNAMICS: DIPOLAR FLUCTUATION SPECTRUM IN CaF_2 **

by

D. A. McArthur*' and E. L. Hahn
Physics Department and Inorganic Materials Research
Division of Lawrence Radiation Laboratory,
University of California
Berkeley, California

and

R. E. Walstedt+
Bell Telephone Laboratories, Incorporated
Murray Hill, New Jersey

ABSTRACT

A series of rotating-frame nuclear double-resonance experiments is reported in which the NMR of the rare isotope ^{43}Ca (natural abundance 0.13%) in CaF_2 is detected via the observable resonance signal of the abundant ^{19}F nuclei. The technique consists of (1) cooling the ^{19}F dipolar interaction energy reservoir by means of adiabatic demagnetization in the rotating frame, (2) coupling the rare ^{43}Ca to this cooled reservoir by means of a rotating magnetic field at or near the ^{43}Ca nuclear Larmor frequency, and (3) examining the final state of this reservoir by measuring the "dipolar" free induction

---

**Work supported in part by the National Science Foundation.

*Now at Bell Telephone Laboratories, Incorporated, Holmdel, New Jersey.

'This work was submitted in partial fulfillment of the requirements for the Ph.D.

+This work was initiated while the author was a Research Associate at the Physics Department, University of California, Berkeley, California.

signal following a $\pi/4$ rf pulse at the ^{19}F Larmor frequency. With this basic format, results have been obtained and are reported here for (a) the relative heat capacities of the ^{43}Ca rotating-frame Zeeman Hamiltonian and the ^{19}F dipolar Hamiltonian terms, (b) the cross-relaxation time for the ^{43}Ca-^{19}F energy-transfer process as a function of rotating-frame effective field strength and orientation, (c) transient oscillations of the ^{19}F dipolar spin-temperature upon application of an rf pulse at the ^{43}Ca resonance frequency, (d) the transverse (T_2) relaxation process of the ^{43}Ca nuclei, and (e) the spin-lattice relaxation time (T_1) of the ^{43}Ca nuclei. Theoretical expressions for results (a) and (b) are obtained using the well-known thermodynamic model to describe the state of the ^{19}F and ^{43}Ca spin systems. The ^{19}F-^{43}Ca dipolar coupling is treated as a perturbation to obtain a simple "golden rule" expression for the cross-relaxation rate. This model, first applied to nuclear double-resonance by Hartmann and Hahn, is combined here with the experimentally determined fluctuation spectrum of the ^{19}F-^{43}Ca coupling operator to yield calculated cross-relaxation rates in excellent agreement with the experimental results. The above mentioned fluctuation spectrum is found to be a very nearly exponential function of the rotating-frame ^{43}Ca Zeeman splitting over a range of cross-relaxation rates spanning nearly three orders of magnitude for two distinct orientations of the applied field relative to the crystal axes and to be essentially

independent of the orientation of the rotating-frame effective field. This rather surprising spectral form is crucial to the successful calculation of the results we find, and also leads to satisfactory agreement between theory and experiment for results (c) and (d). The transient oscillation phenomena (c) are the rotating-frame analogy of the pulsed dc-field experiments carried out by Strombotne and Hahn. A density-matrix perturbation expansion technique similar to that used by the latter authors is employed here to explain our results. The form of the ^{43}Ca transverse decay process (d) is calculated by means of the Anderson-Weiss model theory; the exponential decay time is closely approximated by a calculated result using the exponential fluctuation spectrum noted above, and the initial region of nonexponential behavior predicted by this model theory is clearly evident in our results. ^{43}Ca T_1 values (e) were obtained at 300°K and at 355°K with a variety of field orientations in the (110) plane of the crystal axes. The T_1 process is found to be isotropic and to have a temperature-dependence suggesting that it is quadrupolar in origin. The temperature-dependence of T_1 is in reasonable accord with the Van Kranendonk theory.

I. INTRODUCTION

A high-sensitivity nuclear double-resonance technique has been introduced[1] in which the precessing magnetization of an abundant nuclear species is slowly destroyed by causing it to interact with a second system of nuclei of low abundance. This interaction takes place under the influence of rotating magnetic fields applied simultaneously at the respective Larmor frequencies of the two nuclear species involved. Evaluation of the coupling strength (or relaxation time) for the exchange of energy between two sets of nuclei leads to an estimate of 10^{14} - 10^{16} nuclear magnetons as the minimum number that can be detected by the technique. This technique was shown experimentally to have a high sensitivity, but the sample studied contained nuclear spins of moderate (~7 percent) abundance. The theory was found to be approximately correct in this first experiment and in later applications[2] of double resonance in systems of rarer concentrations, but it has not been tested in quantitative detail from the point of view of nonequilibrium conditions, and where the double resonance experiment is considered while off resonance as well as at exact resonance.

It is desirable to study double resonance dynamics in terms of an experiment on a system where pure magnetic coupling is dominant, and where quantitative predictions concerning the nuclear double-resonance dynamics can be made and tested. In this paper we present the results of such a study, in which the NMR of the rare isotope ^{43}Ca (fractional abundance $\cong 1.3\times10^{-3}$)

is observed via the easily detected resonance of the 100 percent abundant ^{19}F nuclear spin system in a single crystal of CaF_2. Instead of the double irradiation, spin-locking method applied in Reference 1, the experimentally simpler double resonance scheme (suggested there) of adiabatic demagnetization in the rotating frame (ADRF)[3] was adapted with only a slight sacrifice in sensitivity. With the latter approach the experiment consists of the following steps. First, ADRF is carried out on the abundant species, defined as A-spins, resulting in a state of low spin-temperature represented by the secular dipolar interaction Hamiltonian term as a thermal reservoir. This energy reservoir is unperturbed by other spin-Hamiltonian terms[4] in the absence of radio-frequency irradiation and the low spin-reservoir temperature established by ADRF persists for a spin-lattice relaxation time of the order of T_1. A thermodynamic analysis of this experiment was demonstrated by Slichter and Holton,[3] whose careful work gave further validation to the rotating-frame spin-temperature concept originally advanced and demonstrated by Redfield.[5] Following ADRF, the cooled A-spin dipolar reservoir can be brought into thermal contact with the rare spin species, defined as B-spins, by applying a rotating field H_1 at the B-spin Larmor frequency. By pulsing H_1 on and off, or by rotary saturation,[5] an energy influx into the A-spin reservoir can be generated via the B nuclei, leading to a more rapid warm-up rate for the associated spin-temperature. This accelerated

relaxation of the A-spin temperature is detected by monitoring the A-spin NMR signal following the B-spin irradiation sequence; only through observation of the A signal is it possible to determine the B-spin behavior throughout this investigation. A preliminary report of our results with this scheme has been published.[2]

Within the framework of the approach we have outlined, an interesting variety of NMR properties of the ^{43}Ca - ^{19}F spin systems can be investigated which have implications that extend beyond the quest for ultimate sensitivity for detecting rare nuclear spins. In particular we report a series of experiments in which the central and recurrent theme is the dipolar fluctuation spectrum of the abundant ^{19}F nuclear spins, or, more precisely, of the dipolar operator which couples these nuclei to a rare ^{43}Ca spin moment. This spectrum is subject to direct measurement here and provides valuable insight, because successful calculations of such a spectrum are not available. Further, the present studies probe the thermodynamical nature of the rotating-frame A-B spin system energy transfer process, clearly demonstrated by the results given by Lurie and Slichter.[6] These authors showed that the relative heat capacities of coupled spin-systems are accessible to experimental measurement independent of any theory of A-B coupling rates or spin-lattice relaxation, provided, however, that the B-spin system is not too low in abundance. Such heat capacity measurements are also carried out here as a

necessary adjunct to our other experimental objectives.

Our main goal at the outset is to investigate the time-constant (τ_{AB}) for energy exchange between rare and abundant nuclei as an extension of the thermodynamic (spin-temperature) model of rotating-frame dynamics, and to compare the results with quantitative calculations. For this purpose the CaF_2 system provides a favorable case in a number of respects. The ^{43}Ca nuclear moment is small enough so that its dipolar coupling with the surrounding ^{19}F can be considered weak compared with the ^{19}F - ^{19}F coupling. Thus the A-B coupling operator can be successfully treated as a perturbation, leading to an exponential relaxation process.(7) Also, the ^{43}Ca nuclei are sufficiently dilute so that interactions among them may be safely neglected in calculating their resonance properties. At the same time the ^{43}Ca dilution is not too small, so that signals several orders of magnitude above the detection threshold are available, and no impediment is presented to a double-resonance study ranging over wide signal amplitude conditions which might be grossly unfavorable from the standpoint of sensitivity.

Calculation of the cross-relaxation time constant τ_{AB} is carried out by means of density-matrix perturbation theory.(8,9,10) In the ADRF case τ_{AB}^{-1} is essentially the rate at which transitions are excited between the rotating-frame Zeeman levels of the B-spin by the A-B dipolar coupling operator, which in turn is being randomly modulated by flip-flop interactions

among the A-spins, specified by a spin-spin interaction time constant T_{2A}. With a B-spin Zeeman splitting $\omega_{eB} = \gamma_B H_e$, where H_e is the rotating frame effective field, $\tau_{AB}^{-1}(\omega_{eB})$ is simply proportional to the spectral density of the perturbation operator at frequency ω_{eB}. As noted above, it is generally not feasible to calculate such a spectral density function directly. Instead, one ususally resorts to the assumption of a mathematically convenient form (e.g., Gaussian), with amplitude and width parameters determined by the method of moments.[11,12,13] In the present work the spectral form is obtainable directly from measured values of $\tau_{AB}^{-1}(\omega_{eB})$, which are found to vary as an exponentially decreasing function of ω_{eB}. With this experimentally determined spectrum, the calculation of $\tau_{AB}(\omega_{eB})$ can be carried out without any arbitrary assumptions. As a result, theory and experiment are found to be in excellent accord. The details of these calculations as well as the elements of the thermodynamic model of rotating frame double resonance are summarized in Section II in a form suitable for the interpretation of our experiments. Experimental data for the relaxation times τ_{AB} and for the heat capacity of the rare spins in an applied rf field are given in Section IV, where a series of pulsed double-resonance experiments are reported.

Double resonance measurements were also carried out in which the B-spin energy reservoir was continuously heated by means of rotary saturation.[5] These experiments are described in Section V. Here an audio-frequency modulation of the static

field $\underline{H}_o$ at frequencies $\sim\omega_{eB}$ causes absorptive transitions between the B-spin rotating frame Zeeman levels. By adopting a simple BPP[14] theory of audio saturation we extract additional data for the cross-coupling time τ_{AB} which parallels that of Section IV. A detailed examination of audio-resonance linewidths was also carried out, and it is interesting to compare these results with the work of Franz and Slichter[15] on rotary saturation of the ^{19}F spins in CaF_2. These authors successfully explained their results with a theory based on spin quantization in a second rotating frame, rotating at the frequency of applied audio modulation about an axis parallel to the effective field $\underline{H}_e$ in the first rotating frame. The conditions of high audio saturation required for this approach are also encountered in our work, and a corresponding expression for the audio lineshape is derived for the rare-spin case. Interestingly, this expression is asymptotically approached by the BPP[14] theory at high saturation levels.

In addition to the pulsed rf field and rotary saturation methods of Sections IV and V, we demonstrate in Section VI a third double-resonance technique which steps beyond the confines of the thermodynamic reservoir model. This is based upon the oscillatory behavior of the A-B coupling energy that persists for a time $\sim T_{2A}$ during the application of an rf pulse at or near the B-spin Larmor frequency. These oscillations, which occur at frequency ω_{eB}, display the rotating-frame analogy of the

pulsed-d.c. field transient oscillations investigated earlier.[16] An analysis of this effect is given in which the density matrix equation of motion is integrated over the time duration of the rf pulse, including terms up to second order in the A-B coupling operator. Employed as a double-resonance technique in detecting the B-system, this phenomenon gives the greatest A-spin heating effect with π-pulses applied at exact resonance to the B-nuclei at a rate $\sim 1/T_{2A}$. Under these conditions one obtains a double resonance interaction comparable in effectiveness to the methods discussed in Sections IV and V.

In a further development of the ADRF method, we show in Sections VII and VIII, respectively, how these ideas may be employed to investigate the spin-spin (T_{2B}) and spin-lattice (T_{1B}) relaxation processes of rare nuclei. T_{1B} for $^{43}Ca:CaF_2$ is found to be quite long ($\sim$200 sec) with a temperature dependence indicating that it is quadrupolar in origin. The T_{2B} results are particularly important in corroborating the measured values of τ_{AB}, since $\tau_{AB} \rightarrow T_{2B}$ as $\omega_{eB} \rightarrow 0$. In this connection the measured values of T_{2B} are further supplemented by the closely related audio linewidths presented in Section V. Since the short correlation time condition is only marginally acceptable in assessing the quantity T_{2B}, the full spin-spin relaxation process is compared with a calculated relaxation function obtained from the Anderson-Weiss[13]

model. Again, the fluctuation spectrum determined from the $\tau_{AB}(\omega_{eB})$ results of Section IV is crucial in a successful application of this model theory, as is demonstrated by a comparison with the usual assumption of a Gaussian fluctuation spectrum. Recently, systematic discrepancies have been noted[17] between experimental ESR and NMR linewidths and values calculated on the Anderson-Weiss theory assuming a cut-off Lorentzian lineshape model. Interestingly, these discrepancies are in the same direction as would be found here under this assumption. To our knowledge the present work constitutes the only case where a directly measured fluctuation spectrum is available for comparison of experimental and calculated linewidths.

II. THERMODYNAMIC MODEL

In this section we use the thermodynamic model to derive a set of equations with which to interpret our double-resonance experiments. Our approach, which is similar to that of previous investigators,[1,2] starts with the system Hamiltonian and applies the spin-temperature approximation to describe the thermodynamic state of both nuclear spin-systems; also, the extreme line narrowing second-order relaxation assumption is made to calculate the rate of energy exchange between the two systems. However, our experimental results require the analysis of two spin reservoirs which are not generally in thermal equilibrium with one another; and considerations relating to nonequilibrium transient effects such

as spin diffusion and incompletely damped spin-spin interactions will be taken up after introduction of the thermodynamic model. Because our objective is to give an entirely quantitative account of these experiments, we make a careful examination of a number of assumptions essential to a quantitative theory of this sort.

Although the equations will be couched in general form, we will of course have in mind the application to a single crystal of CaF_2, with the 100 percent abundant ^{19}F nuclei ($I = 1/2, \gamma/2\pi = 4.0055$ kHz/G.) as the "A" spin NMR system observed directly, and the 0.13 percent abundant ^{43}Ca ($I = 7/2, \gamma/2\pi = 0.2865$ kHz/G.) as the rare "B" spin NMR which is observed only indirectly through the intermediary A-spins. With these two species in mind, we assume throughout that inhomogeneous broadening, magnetic or quadrupolar, is totally absent.[18]

A. The Hamiltonian

We retain only those terms in the Hamiltonian $\mathcal{H}$ which are necessary for the description of the rotating frame double-resonance process in a large magnetic field $\underline{H}_o$. Therefore we take

$$\mathcal{H} = \mathcal{H}_d^{AA} + \mathcal{H}_z^B + \mathcal{H}_{rf}^B(t) + \mathcal{H}_d^{AB} + \mathcal{H}_{aud}^B(t) + \mathcal{H}_{SL}^A + \mathcal{H}_{SL}^B. \quad (1)$$

The first term

$$\mathcal{H}_d^{AA} = \sum_{i>j} A_{ij}(I_{zi}I_{zj} - 1/4\ I_{+i}I_{-j} - 1/4\ I_{-i}I_{+j})$$

is the secular or zero-frequency term of the dipolar interaction among the A nuclei $\underline{I}_i$. This term provides a large A-spin energy reservoir, the state of which is examined by observing the associated "dipolar" free-precession signal.[19] All of the nonsecular (high-frequency) A-A dipolar terms, as well as the A-spin Zeeman coupling, are strongly decoupled from $\mathcal{H}_d^{AA}$ and are omitted.[4] The second and third terms (in frequency units),

$$\mathcal{H}_z^B + \mathcal{H}_{rf}^B(t) = -\gamma_B[H_oS_z+H_1S_x\cos\omega t+H_1S_y\sin\omega t],$$

describe the coupling of an isolated B-spin $\underline{S}$ with the applied d.c. and rotating fields H_o and H_1, respectively. They are representative of the B-spin energy reservoir. We consider an isolated B-spin not only for the sake of simplicity, but also to emphasize that the B-spins can be assumed to act independently of one another. Dipolar coupling among the very dilute B-spins is neglected, since a rough estimate of the corresponding time constant for this coupling (see Appendix A) is extremely long compared to the time scale in which measurements are made in this system. The fourth term,

$$\mathcal{H}_d^{AB} = S_z \sum_j B_j I_{zj},$$

describes the secular dipolar coupling between a given B-spin and neighboring A-spins. This term provides the essential thermal link whereby energy is coupled between the A and B-spin system . The coefficients A_{ij} and B_j are the usual dipolar interaction coefficients where the subscripts express the lattice coordinates of the A-spins concerned.

The fifth term,

$$\mathcal{H}_{aud}^{B}(t) = -\gamma_B H_a S_z \cos(\omega_a t),$$

represents the B-spin coupling with an applied audio-frequency modulation field H_a that imposes rotary saturation[5] to enhance the detection efficiency and to study B-spin rotating-frame resonance properties in a particular kind of double resonance experiment to be described more fully below. The A-spin interaction with $\mathcal{H}_a$ is omitted, since it commutes with all the foregoing Hamiltonian terms which describe the A system. $\mathcal{H}_{SL}^{A}$ represents the spin-lattice interaction of the A nuclei, or more precisely, the coupling of the operator $\mathcal{H}_d^{AA}$ with time-dependent modes of the lattice coordinates. We shall not delve into the detailed nature of $\mathcal{H}_{SL}^{A}$, which involves coupling with stray paramagnetic impurities together with spin diffusion among the A-spins. The effects of $\mathcal{H}_{SL}^{A}$ will simply

be represented by an empirical relaxation time T_{1A} in our model. Finally, $\mathcal{H}_{SL}^{B}$ represents the spin-lattice interaction of the B-nuclei. The associated laboratory frame relaxation process will be schematically represented by a relaxation time T_{1B}. This relaxation process appears to be dominated by quadrupolar Raman scattering of thermal phonons and is quite weak ($T_{1B} \sim 200$ sec). Because of this, T_{1B} is considered to have a negligible effect on our double-resonance phenomena and is omitted in the rotating frame considerations to follow. Further discussion of T_{1B} is deferred to Section VIII.

B. Density Matrix in the Rotating Frame

We examine the properties of the double resonance Hamiltonian Equation (1) using the equation of motion $i\dot{\rho} = [\mathcal{H},\rho]$ of the spin-system density matrix ρ. This equation is transformed to a reference frame rotating at a frequency ω with respect to B-spin coordinates and tilted at an angle θ so as to place the axis of quantization along the rotating-frame "effective field," as shown in Figure 1. This is accomplished by the transformed density matrix

$$\rho_R = R\rho R^{\dagger}$$

where $R = \exp(i\theta S_y)\exp(-i\omega t S_z)$. The equation of motion for ρ_R is then

$$i\dot{\rho}_R = [\mathcal{H}_R,\rho_R] \qquad (2)$$

with

$$\mathcal{H}_R = \mathcal{H}_d^{AA} - \gamma_B H_e S_Z + (S_Z \cos\theta - S_X \sin\theta) \sum_i B_i I_{zi}$$

$$- \gamma_B H_a \cos(\omega_a t)(S_Z \cos\theta - S_X \sin\theta). \qquad (3)$$

The effective field $H_e = \hat{i}H_1 + \hat{k}\Delta H$ defines the direction in space of the new Z-axis of B-spin quantization, where $\Delta H = H_o - \omega/\gamma_B$. The X-axis is perpendicular to the Z-axis and lies in the rotating frame x-z plane (see Figure 1). θ is the angle between H_e and the laboratory z-axis so that $\cos\theta = \Delta H/H_e$ and $\sin\theta = H_1/H_e$. The transformation effects a correspondence between terms of Equations (1) and (3) as follows:

$$\mathcal{H}_z^B + \mathcal{H}_{rf}^B(t) \rightarrow \gamma_B H_e S_Z; \; \mathcal{H}_d^{AB} \rightarrow (S_Z \cos\theta - S_X \sin\theta) \sum_j B_j I_{zj};$$

and

$$\mathcal{H}_{aud}^B(t) \rightarrow \gamma_B H_a \cos(\omega_a t)(S_Z \cos\theta - S_X \sin\theta).$$

In the representation of Equations (2) and (3) the Hamiltonian has become explicitly time-independent (ignoring for the present the effects of the audio-irradiation term). It has the simple structure of A- and B-spin energy reservoirs coupled by a perturbation

$$\mathcal{H}_p = (S_Z \cos\theta - S_X \sin\theta) \sum_j B_j I_{zj}. \tag{4}$$

If the effective Zeeman splitting $\omega_{eB} = \gamma_B H_e$ is adjusted to be within the spectral width of A-spin dipolar fluctuation ($\gamma_B H_e \sim \gamma_A H_{LA}$, where the A-spin local field H_{LA} is defined below) then $\mathcal{H}_p$ will cause transitions between the energy levels of the terms $-\omega_{eB} S_Z$ and allow an energy transfer between the two spin systems.

Following Redfield[5] and succeeding investigators,[1,3,6,7,19] we employ a spin-temperature description of the states of both spin-systems with a density matrix of the form

$$\rho_R(\mathrm{eq}) = \exp\left[-\hbar \mathcal{H}_d^{AA}/kT_A + \hbar\omega_{eB} S_Z/kT_B\right] \Big/ \mathrm{Tr}\, \exp\left[\hbar \mathcal{H}_d^{AA}/kT_A + \hbar\omega_{eB} S_Z/kT_B\right]. \tag{5}$$

This formulation requires that the state of both spin systems must be specified by a temperature, which requires internal thermal equilibrium for the A system. In turn this imposes a unique temperature for the B spins, a point to be examined later in further detail. We use Equation (5) in its high-temperature form:

$$\rho_R(\text{eq.}) \cong \frac{1}{\mathrm{Tr}(1)} + \frac{\hbar\omega_{eB}S_Z}{kT_B\mathrm{Tr}(1)} - \frac{\hbar \mathcal{H}_d^{AA}}{kT_A\mathrm{Tr}(1)} , \tag{6}$$

to express the energy content of the A- and B-spin reservoirs, and subsequently derive the energy transfer equations. From $E_A = \hbar\,\mathrm{Tr}[\mathcal{H}_d^{AA}\rho_R(\text{eq.})]$ and $E_B = -\hbar\omega_{eB}N_B\mathrm{Tr}[S_Z\rho_R(\text{eq.})]$ we find

$$E_A = -\frac{N_A\hbar^2\gamma_A^2 I(I+1)H_{LA}^2}{3kT_A} , \tag{7a}$$

and

$$E_B = -\frac{N_B\hbar^2\omega_{eB}^2 S(S+1)}{3kT_B} , \tag{7b}$$

where N_A and N_B are the total number per c.c. of each type of nucleus in the specimen; and the A-spin local dipolar field H_{LA} has the conventional definition $H_{LA}^2 = \mathrm{Tr}(\mathcal{H}_d^{AA})^2/\mathrm{Tr}\left\{\gamma_A^2 \sum_i I_{zi}^2\right\}$. The energy content represented by the coupling term $\mathcal{H}_p$ is omitted here as always negligibly small compared with E_A.

C. Double Resonance Equations

The A-B relaxation equation may be simply derived by viewing E_B as the energy of a macroscopic magnetization M_B in the applied field H_e, i.e., $E_B = -M_BH_e$. The relaxation of M_B via the perturbation $\mathcal{H}_p$ takes place in much the same fashion as in a magnetic dipole spin-lattice relaxation process.

The $\Delta m = \pm 1$ transition rates between the B system m-levels are given by $W^{AB}_{m,m+1} = (1/2)\tau^{-1}_{AB}[I(I+1) - m(m+1)]$ where the m-levels are established from the Hamiltonian term $-\omega_{eB}S_Z$, and

$$\frac{d}{dt} M_B(T_B) = - 1/\tau_{AB}[M_B(T_B) - M_B(T_A)] \qquad (8)$$

In Equation (8) M_B is relaxed toward a value corresponding to the instantaneous A-spin temperature T_A. Therefore we may express conservation of energy by the relation $\dot{E}_A + \dot{E}_B = 0$, or

$$\dot{E}_A = - H_e/\tau_{AB}[M_B(T_B) - M_B(T_A)]. \qquad (9)$$

Equations (8) and (9) express the A-B energy transfer process only, and we must add to them terms which represent the saturating effect of the audio-irradiation field H_a (B-spins) and spin-lattice relaxation (A-spins), respectively. We treat the audio absorption in the rotating field H_e in exact analogy to the case of rf absorption in a laboratory field H_o. In the perturbation limit (i.e., for H_a smaller than the audio-resonant linewidth), the effect of H_a may be expressed as a fractional rate of decay $1/\tau_a$ of the magnetization M_B, where[14,19]

$$1/\tau_a = \frac{\omega_a}{\omega_{eB}} \omega^2_{1a}\pi f_a(\omega_a). \qquad (10)$$

$f_a(\omega_a)$ is the normalized audio-lineshape function and $\omega_{1a} = 1/2\ \gamma_B H_a \sin\theta$. Adding the term $-M_B(T_B)/\tau_a$ to the right-hand side of Equation (8) and expressing the results in terms of inverse spin temperatures ($\beta_B \equiv T_B^{-1}, \beta_A \equiv T_A^{-1}$) using Equation (7b) we find

$$\frac{d}{dt}\beta_B = -(\beta_B-\beta_A)/\tau_{AB} - \beta_B/\tau_a. \qquad (11a)$$

Similarly we add a phenomenological spin-lattice relaxation term $-(E_A(T_A)) - E_A(T_L))/T_{1A}$ to Equation (9), which with the aid of Equations (7a) and (7b) becomes

$$\frac{d}{dt}\beta_A = -\ \varepsilon(\beta_A-\beta_B)/\tau_{AB} - (\beta_A-\beta_L)/T_{1A}, \qquad (11b)$$

where

$$\varepsilon = \frac{N_B\omega_{eB}^2 S(S+1)}{N_A\gamma_A^2 H_{LA}^2 I(I+1)} \qquad (12)$$

is the ratio of heat capacities of the B- and A-spin reservoirs and β_L is the inverse lattice temperature. Equations (11) give a complete description of the double resonance dynamics under investigation here. As noted above the B system spin-lattice relaxation time term which included T_{1B} has been omitted from Equation (11a), primarily because T_{1B} is extremely long and has a negligible effect on the double-resonance experiments.

Equations (11) may be seen to represent the behavior of the system of energy reservoirs shown in Figure 2, where the coupling between reservoirs is labelled by the corresponding time-constant. The audio generator is effectively a reservoir at infinite temperature, since the B-spin coupling with it tends to produce total saturation of M_B. This pictorial representation allows a simple visualization of the two types of double resonance considered here. First, in the rotary saturation method the rotating field (H_1) and the audio-irradiation field (H_a) are applied simultaneously in a single pulse long enough to increase measurably the A-spin temperature T_A. During this time, energy flows from the audio generator via the B-spins into the A-spin reservoir to cause the observed increase in T_A. After an initial transient the B-spins reach a quasi-equilibrium state in which (setting $\dot{\beta}_B = 0$ in Equation (11a)) $\beta_B \cong (\tau_a/(\tau_{AB}+\tau_a))\beta_A$. For strong audio irradiation we have $\tau_a \ll \tau_{AB}$ and $\beta_B \cong 0$. With the assumption that $\beta_L \ll \beta_A$, which applies throughout our work, we find

$$\frac{d}{dt}\beta_A \cong -\left(\frac{\varepsilon}{\tau_{AB}} + T_{1A}\right)\beta_A .$$

Thus, the warm-up rate of the A-spin is increased under these conditions by the double-resonance rate contribution ε/τ_{AB}, which is the largest one observable with the methods considered in this section.

In the pulse method the audio generator is not used ($\tau_a = \infty$), and the rotating field H_1 is repeatedly turned on and off, alternately connecting and disconnecting the B- and A-spin reservoirs. If complete A-B equilibrium is reached during each "pulse" of H_1, and the B-spin reservoir is brought to infinite temperature (i.e., $M_B = 0$) between pulses, then T_A is increased by a factor $(1+\varepsilon)$ for each pulse applied. After many pulses a cumulative and measurable increase in T_A is produced. The net heat input to the A-spin reservoir in this technique is equal to the work done on the B-spin system in turning off H_1. The thermodynamics of the pulse method have been investigated in detail by Lurie and Slichter.[6] Although this technique is not in principle as potent in heating the A-spins as the rotary saturation method, it is useful for the present work in that it allows a detailed study of the A-B thermal equilibrium process.

To complete the theory we need only to find an expression for τ_{AB} in terms of the Hamiltonian parameters (Equation (3)). This we do under the assumption of short correlation times by means of the master equation for the time rate of change of the density matrix.[10] This formulation, combined with the spin-temperature assumption used here, gives an A-B coupling relation of the form of Equation (11a), with

$$\frac{1}{\tau_{AB}} = \frac{1}{\mathrm{Tr}S_Z^2} \int_0^\infty d\tau \; \mathrm{Tr}\left\{ S_Z \left[\mathcal{H}_p(0), [\mathcal{H}_p(\tau), S_Z] \right] \right\}, \qquad (13)$$

where

$$\mathcal{H}_p(\tau) = T\mathcal{H}_p T^{\dagger}$$

with

$$T = \exp\left[\left(\mathcal{H}_d^{AA} - \omega_{eB} S_Z\right) i\tau\right].$$

Upon evaluating Tr_B (where $Tr \equiv Tr_A Tr_B$) in Equation (10) we find

$$\frac{1}{\tau_{AB}} = \sin^2\theta \langle \Delta\omega^2 \rangle_{AB}$$

$$\cdot \int_0^{\infty} d\tau \cos \omega_{eB}\tau \left\{ \frac{Tr_A \left(\sum_j B_j I_{zj}\right) e^{i\mathcal{H}_d^{AA}\tau} \left(\sum_j B_j I_{zj}\right) e^{-i\mathcal{H}_d^{AA}\tau}}{Tr_A \left[\sum_j B_j I_{zj}\right]^2} \right\} \tag{14}$$

Here $\langle \Delta\omega^2 \rangle_{AB}$ is the Van Vleck[20] second moment of the B-magnetic resonance line, and the quantity in braces is the autocorrelation function $a(\tau)$ of the operator $\sum_j B_j I_{zj}$. $a(\tau)$ can be found in principle by expanding the exponential operators in Equation (14) to obtain a series in even powers of τ. In practice it is

feasible to calculate only the coefficients of τ^2 and possibly τ^4 in this fashion, with the consequence that one usually reports to the assumption of a mathematically convenient form for $a(\tau)$ with which to carry through the calculation. Here instead we use the experimentally determined form $1/\tau_{AB}(\omega_{eB}) \simeq e^{-\alpha\omega_{eB}}$, to be justified later (Section IV), as a basis for our calculations. From the Fourier transform of Equation (14) it follows that

$$a(\tau) = \left(1+\tau^2/\tau_c^2\right)^{-1}, \tag{15}$$

and we identify α as the correlation time τ_c. By equating the τ^2 terms in power series expansions of Equations (14) and (15) we find

$$\frac{1}{\tau_c^2} = -\frac{1}{2}\,\frac{\mathrm{Tr}\left[\mathcal{H}_d^{AA},\ \sum_j B_j I_{zj}\right]^2}{\mathrm{Tr}\left[\sum_j B_j I_{zj}\right]^2} \quad . \tag{16}$$

Equation (14) now simplifies to

$$\frac{1}{\tau_{AB}} = \frac{\pi}{2}\sin^2\theta\langle\Delta\omega^2\rangle_{AB}\tau_c e^{-\omega_{eB}\tau_c}, \tag{17}$$

where the parameters $\langle\Delta\omega^2\rangle_{AB}$ and τ_c can be calculated to high accuracy from the known dipolar coupling coefficients.

Combining Equations (11) with τ_{AB}, as calculated above, we are now equipped with an essentially complete formulation of rotating-frame double resonance dynamics for CaF_2. Calculated values of τ_c and τ_{AB} are tabulated in Section IV where they are compared with experimental data. On the whole the simple formulation developed here is found to give a reasonable account of our results. Since these calculations depend so heavily on the fast correlation and spin-temperature assumptions, we close this section with a detailed examination of these matters.

D. Fast-Correlation and Spin Temperature Approximations

The condition for validity of the fast-correlation approximation may be simply expressed here as

$$\tau_{AB} >> \tau_c .$$

We see from Equation (17) that this condition is most severely tested for $\theta = \pi/2$ with small values of ω_{eB}, i.e., as $e^{-\omega_{eB}\tau_c} \rightarrow 1$ to give the shortest possible τ_{AB} value. In the experiments of Section IV the conditions which favor a short τ_{AB} are that of $\underline{H}_o$ along the $\langle 111 \rangle$ crystalline axes and with $\omega_{eB}/2\pi = 2$ kHz. For this extreme, we find $\tau_c \cong 80$ μsec and $\tau_{AB} \cong 500$ μsec, which meets the above requirement reasonably well. Throughout the range of experimental conditions encountered, then, the experimental values of τ_{AB} and τ_c satisfy the inequality $\tau_c/\tau_{AB} \leq 0.16$. As a result, the transient behavior investigated in Section VI will affect

only negligible fraction ($\sim\tau_c/\tau_{AB}$) of the relaxation process. Furthermore, the deviation from a simple exponential due to these transients is found in any case to be less than 3 percent of the exponential term, and is therefore of negligible importance to our results.

The spin temperature assumptions are expected to hold for nuclear spin energy reservoirs possessing internal thermal equilibrium, and this also requires $\tau_{AB} >> \tau_c \sim T_{2A}$. The maintenance of thermal equilibrium among the A-spins depends upon spin diffusion to carry away excess energy from the double resonance "heating centers" (i.e., B-spin sites). To establish a criterion for this "rapid diffusion" limit, we require that during one double-resonance relaxation time constant $T_{DR} = \tau_{AB}/\varepsilon$, the spin diffusion process must be complete in a sphere of volume n_B^{-1}, where n_B is the volume density of B-spins. For this purpose we assume isotropic diffusion in a continuum of diffusivity D, for which in time t a point-source disturbance would be expected to propagate a distance $r \simeq (Dt)^{1/2}$. Thus we require a spin-diffusion time constant $\tau_{SD} \sim r_B^2/D << \tau_{AB}/\varepsilon$, where $4\pi r_B^3/3 = n_B^{-1}$. For the case of ^{43}Ca in CaF_2 we have $r_B = 7a$, where a is the $^{19}F - {}^{19}F$ near-neighbor distance. The calculations of Lowe and Gade[21] give $D = 0.14(\hbar\gamma_A^2/a)$ for the s.c. lattice, from which we find $\tau_{SD} \cong 11$ msec. This we compare with the data given below which give a minimum value $\tau_{AB}/\varepsilon \gtrsim 100$ msec, so the condition $\tau_{AB}/\varepsilon >> \tau_{SD}$ is obeyed as required. It

is interesting to note that $\tau_{SD}/\tau_{DR} \propto n_B^{1/3}$, so that the criterion $\tau_{SD}/T_{DR} << 1$ improves as the rare nuclei under investigation become more dilute.

Although the CaF_2 system satisfies the simple criterion of rapid spin-diffusion set forth above, we may need to impose an even more stringent requirement to guarantee the validity of Equation (11a), since this equation demands, in effect, that the A-nuclei <u>in the immediate neighborhood of each B spin</u> reflect the bulk A-spin temperature. A detailed theoretical examination of the latter situation is extremely difficult, because the diffusion model, although it has been applied to this problem by Slusher and Hahn[2], breaks down when considering the small scale of the distances between a rare spin and its immediate neighbors. We shall not probe this question further, but instead develop a simple <u>experimental</u> criterion to determine the presence of spin-diffusion "inhibition" of the τ_{AB} process. Using Equation (14) it is easily shown that the area

$$A = \int_0^\infty \tau_{AB}^{-1}(\omega_{eB})d\omega_{eB} \qquad (18)$$

under the rate "spectrum" curve is given simply by $A = \pi/2\langle\Delta\omega^2\rangle_{AB}\sin^2\theta$, independent of the functional form of $a(\tau)$. With accurately calculated values of $\langle\Delta\omega^2\rangle_{AB}$, comparison of calculated and experimental values of A is a sensitive test

for spin-diffusion effects, which always tend to reduce the value of A. This criterion is applied to the τ_{AB} data presented in Section IV, where spin-diffusion effects are estimated to be small.

In addition to the requirements of local A-spin temperature equilibrium the thermodynamic model, Equations (11) also demand that the population of the B-spin (rotating frame) m-states be describable by a Boltzman distribution, i.e., by a spin termperature. Whereas in abundant spin systems this situation is maintained by mutual spin-flips, here the B-B dipolar interactions are much too weak to be effective during the A-B equilibration time (see Appendix A). Instead, we depend upon the nature of the A-B coupling to maintain a B-spin temperature. With the form of $W^{AB}_{m,m+1}$ given above (see Equation (8)) the B-spin relaxation has the convenient property that if the m-state populations are initially in a Boltzman distribution, they will remain so at all points in time. Thus, although the B-spins behave totally independently of one another, they may be considered to possess an effective internal "thermal equilibrium."

Breakdown of this simple picture will occur in principle if higher order rate processes having a more complicated m-dependence than $W^{AB}_{m,m+1}$ given above become important. This would result if the "fast correlation" assumption used to calculate τ_{AB} is not strictly valid. The next higher

order perturbation terms give rate contributions of the order of τ_c/τ_{AB}^2 with m-dependences including m^3 and m^4 terms. These terms are smaller than the lowest order $W_{m,m+1}^{AB}$ by a factor $\delta \sim \tau_c/\tau_{AB} \lesssim 0.16$, so that such higher-order terms are expected to be small here, but perhaps not entirely negligible. The effects of these higher order terms on our experimental results are expected to be (a) an increase in the relaxation rate over that given by Equation (14) by a fractional amount $\sim\delta$, and (b) a deviation from the simple exponential behavior assumed in Equation (8) by an amount $\sim\delta^2 < 0.03$, which is essentially unobservable here. This matter is discussed further along with the results presented in Section IV.

III. EXPERIMENTAL APPARATUS AND TECHNIQUE

A. The Equipment

A block diagram of the double-resonance apparatus is shown in Figure (3). It consists essentially of four parts, the A-frequency transmitter and receiver, the B-frequency rf power system, the audio power system, and the magnet and field-regulation system (not shown). The A system is basically a medium-power coherent pulsed NMR setup in which the output from an 11 MHz crystal-stabilized master oscillator is fed simultaneously to a gated power amplifier and a phase detector at the output of the receiver. From the phase-detector the

video A-signal is further amplified and then monitored with a boxcar integrator and strip-chart recorder. Special features were incorporated into the A-rf power system to allow the waveform to be abruptly phase-shifted and then slowly turned off to carry out the ADRF preparation of the A-spin system.

The B-rf power system consists of a tunable gated power amplifier driven by a Hewlett-Packard model 606A VFO. This system was arranged to cover a band of frequencies centered on the ^{43}Ca Larmor frequency of ~787 kHz. A specially designed gated amplifier was used to supply radio frequency power either in a series of short bursts for the case of pulsed double-resonance or in one burst of good (~1 percent) amplitude stability lasting for a second or more for the rotary-saturation double-resonance case. Finally, the audiofrequency saturation field was supplied by a conventional high-fidelity power amplifier driven by a Hewlett-Packard model 202C audio oscillator. All of the timing and pulse-modulation waveforms were derived from Tektronix 160-series pulse and waveform generators (not shown in Figure 3).

A specially designed NMR head shown in Figure 4 was used to fulfill the requirements of providing rf magnetic fields perpendicular to $\underline{H}_o$ at two widely separated frequencies as well as a crossed-coil transmitter-receiver system to function at the A-spin frequency. In addition, the audio field

parallel to $\underline{H}_o$ was generated by a pair of coils situated in the plane of the magnet pole faces. The A-rf power was applied to a pair of Helmholtz coils having a horizontal axis as shown in Figure 4, giving a linearly polarized magnetic field of good homogeneity over the sample volume. The B-spin rf field was generated in a vertical-axis solenoid. The latter coil was wound with an inner diameter just large enough to accommodate the cylindrical CaF_2 specimen and of sufficient length-to-diameter ratio to give the extremely high rf homogeneity (better than 1 percent over the sample volume) required for the rotary-saturation experiments. This same coil was alternately used as the A-spin receiver coil, for which purpose the central portion of the coil covering the sample volume was tapped with the two receiver leads shown in the figure. Switching between these two coil functions was accomplished by means of a relay (see Figure 3). In the B-rf mode the coil taps are left open-circuited and the top of the coil is connected to the B-transmitter outputs as the inductive part of a tuned load. For the A-spin receiver mode both ends and one of the taps of the coil are grounded with the other tap fed to the receiver input, thus forming a low-inductance, high-Q tank coil suitable for the tuning at the higher A-spin Larmor frequency. Another set of contacts on the same relay was used to switch on the audio irradiation, by alternately connecting the audio coils to the amplifier output or to ground.

In order to carry out the measurements of T_{1B} at elevated temperatures reported in Section VIII, the NMR head in Figure 4 was enclosed in an insulated box through which a stream of heated air was passed. The sample temperature was monitored with a copper-constantan thermocouple junction glued to a slot cut in the side of it, using a reference junction at ice temperature. With this simple arrangement temperatures up to 355°K could be maintained to within ±2°K.

The dc magnetic field was supplied by a 12-inch electromagnet using a Varian V-2100 current-regulated power supply. The field was NMR-controlled in order to maintain the long-term stability required for these experiments. This was accomplished with a Varian F-8 Gaussmeter and liquid proton sample, combined with a frequency source stable to within three parts in 10^6 over several hours time. The source consisted of a Gertsch FM-6 frequency meter followed by a Gertsch FM-5 frequency divider. With the field properly set and locked to the proton resonance with the F-8, the ^{19}F resonance condition was maintained with this scheme to within three parts in 10^5 or approximately 10 percent of the ^{19}F linewidth. The residual drift was small enough to be a negligible factor in the overall stability of the ^{19}F signal.

B. The Specimen

The specimen used throughout this investigation was a cylindrical single crystal of CaF_2 with cylinder axis

approximately parallel to the [110] direction, supplied by the Harshaw Chemical Company. Under close scrutiny with back-reflection Laue photographs, the cylinder axis as measured at the cylinder end faces was found to be displaced from (110) orientation by 5 ±1° toward the (100) direction and 3 ±1° toward the (111) direction. To minimize the orientation error in the comparison of theory to experiment all theoretical curves shown here include the 5° and 3° average misorientation.

In orienting the crystal axes relative to the field $\underline{H}_o$, the vertical rotation axis was set within ±0.5 degrees of parallelism with the magnet pole faces, and the rotation angle Ω about this axis was resettable to ±0.5 degree. The angles Ω which bring H_o nearest the (100), (110), and (111) directions were determined from the Ω-dependence of T_{2A}, making use of the fact that $T_{2A}(\Omega)$ is extremal for these field directions. By recording $T_{2A}(\Omega)$, $\Omega(111)$ and $\Omega(110)$ were measured to ±1 degree, giving an angular separation $\Omega(111) - \Omega(110)$ within experimental error of the theoretical value. We note that the slight misorientation of crystal axis described above would not materially affect this angular separation.

The spin-lattice relaxation rates of the F^{19} Zeeman and dipolar Hamiltonian terms are somewhat accidental properties of CaF_2 crystals available, since they depend on the inclusion of stray paramagnetic impurities during the crystal-growing

process. The crystal used for this work was chosen in part because the relaxation times (T_{1A}(Zeeman) = 10 sec and T_{1A}(dipolar) = 4.1 sec) were well suited to the experiment. Although no detailed analysis of the T_{1A}'s was carried out nor were the paramagnetic impurities identified, it is thought that these impurities were dilute enough to play no significant role in the double-resonance properties of the crystal. For example, Bloembergen[22] has reported a shorter T_{1A}(Zeeman) for a specimen of CaF_2 containing 10 ppm Fe, suggesting a ^{43}Ca-to-paramagnetic impurity ratio of 100 or more for the present specimen.

C. Preparing and Monitoring the ADRF State

All the experiments reported here followed a similar pattern of A-spin preparation, B-spin irradiation and manipulation and subsequent reexamination of the A spins. We give a brief description of the A-spin portion of this cycle which was uniform throughout the investigation. To prepare the "cooled" A-spin dipolar reservoir a variety of techniques are available.[1,3,19,23] We selected a procedure of spin-locking the A-spin magnetization followed by rotating-frame adiabatic demagnetization (ADRF). The corresponding A-rf irradiation sequence is shown in Figure 5. It consists of pulsing on an rf field $H_1(A) >> H_{LA}$ at the exact ^{19}F Larmor frequency, phase-shifting this waveform by $\pi/2$ after an equivalent $\pi/2$ pulse

time [$t_w = \pi/(2\gamma_A H_1(A))$] so as to bring $H_1(A)$ parallel to the A-spin magnetization in the x-y plane, i.e., to produce the spin-locked condition, and finally to turn off $H_1(A)$ isentropically, thus reducing the A-spin dipolar temperature to an initial value $T_{Ai} \simeq (H_{LA}/H_o)T_L$. In the present case $T_{Ai} \simeq 0.1°K$. To ensure the isentropic character of the above process, $H_1(A)$ is turned off in a time $t_{ADRF} >> T_{2A} \sim 50$ μsec. Uniform results were found for turnoff times of 10 msec or greater.

In order to check the efficiency of A-spin cooling as well as to monitor T_A at any time after ADRF, the A-spin dipolar free induction signal excited by a $\theta \cong 45°$ rf pulse was observed as shown in Figure 5. With good cooling efficiency one expects a dipolar signal of the order of half the maximum Zeeman free induction amplitude obtainable with a $\pi/2$ pulse; this was found to be the case with the A-spin preparation scheme used.

If the B-spins are not excited following ADRF, then the dipolar signal amplitude $S_D \propto T_A^{-1}$ simply decays toward ~0 (since $T_{Ai} << T_L$) with a relaxation time of T_{1A} (dipolar). This decay process was found to be exponential within experimental error, giving the 4.1 second dipolar relaxation time quoted in III B. As T_A relaxes toward T_L following ADRF, the A-spin magnetization is also recovering toward its thermal-equilibrium value. Thus a 45° pulse will in general excite a free-induction

signal of combined Zeeman and dipolar character. Fortunately, these two signals are out of phase[19] by $\pi/2$, and the dipolar signal of interest can be selected by adjusting the phase-detector to be in exact quadrature with the Zeeman component.

In performing double resonance measurements, the timing sequence of Figure 5 was used in which a time of the order of T_{1A} (dipolar) is allowed between ADRF and the 45° monitoring pulse for the B-spin irradiation to be applied. The dipolar signal from each such cycle is integrated in one-shot fashion to produce a momentary deflection of the recorder pen, which is then returned to a zero-output position by a relay mechanism. The cycles were repeated at intervals of several T_{1A} (Zeeman) or approximately 30 seconds. The zero of signal is found by omitting the $\pi/2$ phase shift from the preparation sequence, resulting in a complete inhibition of dipolar cooling. Any reduction of signal amplitude as a result of B-spin irradiation is then interpreted as a double-resonance effect. The detailed procedures for extracting double resonance data from signal deflections are discussed in the experimental sections which follow.

IV. PULSED DOUBLE RESONANCE

Pulsed double resonance measurements were carried out under a wide variety of experimental conditions in order to test our simple dynamical formulation (Equations (11)) as thoroughly as possible. In this type of measurement a train

of N identical, equally-spaced square pulses of H_1 are applied during the B-spin irradiation time interval of Figure 5. A sample of this waveform is shown in Figure 6. During each pulse the A-B system thermal equilibrium proceeds according to Equations (11). By varying the pulse width τ from 0 to ~3 τ_{AB}, a quantitative study of this process can be carried out. During each pulse of H_1 a macroscopic B-spin magnetization $\underline{M}_B$ is developed along the rotating frame effective field H_e. At the end of the pulse the transverse component $M_B \sin\theta$ is dissipated in a T_2-decay, but the longitudinal component $M_B \cos\theta$ persists in general for a time T_{1B}, thus imposing an initial condition on the next A-B coupling period. In order to avoid the associated complications in the data analysis for $\theta \neq \pi/2$ and render the action of all pulses identical, a "comb" of ten B-rf saturating pulses was applied before each double-resonance pulse (not shown in Figure 6). The pulses in the saturating comb were spaced by ~4 T_{2B} to make them act independently and were adjusted in length to have a maximum effect of attenuating M_B. In this way the $M_B = 0$ condition is guaranteed at the onset of each A-B contact period. The saturating combs also produce an attenuation of the A-spin thermal order that is small except for small f_{eB}, where N is very large, as discussed in Section VI. This is accounted for in the data analysis in a simple manner described below.[24]

Let us now utilize Equations (11) to calculate the behavior of β_A during the first pulse of Figure 6: $0 \leq t \leq \tau$. We note that the audio field H_a is not used here ($\tau_a^{-1} = 0$) and that the T_L^{-1} term in Equation (11b) is negligible throughout. By differentiation and substitution we first convert Equations (11) to an equivalent second-order differential equation involving only β_A:

$$\frac{d^2\beta_A}{dt^2} + \left[\frac{(1+\varepsilon)}{\tau_{AB}} + \frac{1}{T_{1A}}\right]\frac{d\beta_A}{dt} + \tau_{AB}^{-1}T_{1A}^{-1}\beta_A = 0. \qquad (19)$$

This equation has solutions of the form

$$\beta_A(t) = \beta_{A+}e^{-\alpha_+ t} + \beta_{A-}e^{-\alpha_- t} \qquad (20)$$

where

$$\alpha_\pm = \frac{1}{2}\left[\frac{1+\varepsilon}{\tau_{AB}} + \frac{1}{T_{1A}}\right] \pm \frac{1}{2}\left[\left[\frac{1+\varepsilon}{\tau_{AB}} + \frac{1}{T_{1A}}\right]^2 - \tau_{AB}^{-1}T_{1A}^{-1}\right]^{1/2}. \qquad (21)$$

The values of $\beta_{A\pm}$ are determined by the initial conditions $\beta_A(0) = \beta_{Ai}$ and $M_B(0) = 0$, where β_{Ai} is the inverse A-spin temperature immediately following ADRF. With these initial conditions we find

$$\beta_{A\pm} = \pm \frac{\beta_{Ai}\left[\frac{\varepsilon}{\tau_{AB}} + \frac{1}{T_{1A}} - \alpha_{\mp}\right]}{(\alpha_+ - \alpha_-)} . \qquad (22)$$

For the sake of clarity in the following discussion we shall expand the exact expression in Equations (21) and (22) keeping only first-order terms in $\tau_{AB}/T_{1A} \leq 0.1$. Errors incurred in this procedure will be of the order of 1 percent. We emphasize, however, that the exact expressions quoted were used for the data-analysis computer program.[25]

In expanded form, then, Equations (21) and (22) become

$$\alpha_+ \simeq \frac{1+\varepsilon}{\tau_{AB}} + \frac{\varepsilon}{(1+\varepsilon)T_{1A}} , \quad \alpha_- \simeq \frac{1}{(1+\varepsilon)T_{1A}} \qquad (23a)$$

and

$$\beta_{A+} = \frac{\beta_{Ai}}{1+\eta} , \quad \beta_{A-} = \frac{\eta\beta_{Ai}}{1+\eta} \qquad (23b)$$

with

$$\eta = \frac{\varepsilon(1 + \varepsilon + 2\tau_{AB}/T_{1A})}{(1+\varepsilon)} .$$

During the interval $\tau \leq t \leq \tau_0 + \tau$ the A-spins simply continue to undergo spin-lattice relaxation giving $\beta_A(\tau+\tau_0) = \beta_A(\tau)\exp(-\tau_0/T_{1A})$. Combining this relation with Equations (17), (18), and (19) we find with some algebraic manipulation

$$\beta_A(\tau+\tau_0) = \beta_{Ai} e^{-(\tau+\tau_0)/T_{1A}} f_{s.p.} \left[e^{\varepsilon\tau/\left((1+\varepsilon)T_{1A}\right)} \frac{(1+\eta e^{-\alpha\tau})}{(1+\eta)} \right] , \tag{24}$$

where

$$\alpha = \alpha_+ - \alpha_- = \frac{1+\varepsilon}{\tau_{AB}} - \frac{(1-\varepsilon)}{(1+\varepsilon)} \frac{1}{T_{1A}} .$$

Equation (24) has been written so as to separate clearly the double-resonance effect on $\beta_A(\tau+\tau_0)$, represented by the bracketed expression, from the normal T_{1A} decay function $e^{-(\tau+\tau_0)/T_{1A}}$ corresponding to the total B-rf cycle period $\tau + \tau_0$. In addition the factor $f_{s.p.} \lesssim 1$ has been inserted to represent the effect on β_A of the saturating comb, which diminishes β_A for each comb applied. We note that the quantity in brackets reduces for $\tau_{AB} << T_{1A}$ to what one would calculate by letting $T_{1A} \to \infty$ in Equation (19),

$[\ ] \to \left(1+\varepsilon e^{-(1+\varepsilon)\tau/\tau_{AB}}\right)(1+\varepsilon)^{-1}$, as it must.

We now extend the above consideration to a train of N pulses, using for example the expression for $\beta_A(\tau+\tau_0)$ in Equation (24) and $M_B = 0$ as the initial conditions for the second pulse, etc. In this way we find for β_A at the end of the pulsing sequence ($t = N(\tau+\tau_0)$ in Figure 6),

$$\beta_A\left[N(\tau+\tau_0)\right] = \beta_{Ai} e^{-N(\tau+\tau_0)/T_{1A}} (f_{s.p.})^N$$

$$\cdot \left[e^{N\varepsilon\tau/\left[(1+\varepsilon)T_{1A}\right]} \frac{(1+\eta e^{-\alpha\tau})^N}{(1+\eta)^N} \right]. \quad (25)$$

The A-spin monitoring pulse is applied immediately following the B-spin pulse train giving a dipolar signal $S_D[N(\tau+\tau_0)] \propto \beta_A[N(\tau+\tau_0)]$. In taking data this signal is compared with a reference signal $S_D(\text{ref.}) \propto \beta_A(\text{ref.})$ obtained by simply omitting the double-resonance pulse train from the cycle of Figure 5, so that $\beta_A(\text{ref.}) = \beta_{Ai} f_{s.p.}^N e^{-N(\tau+\tau_0)/T_{1A}}$. Each data point thus consists of the measured ratio $S_D[N(\tau+\tau_0)]/S_D(\text{ref.})$, which with Equation (25) becomes

$$\frac{S_D\left[N(\tau+\tau_0)\right]}{S_D(\text{ref.})} = \frac{\beta_A\left[N(\tau+\tau_0)\right]}{\beta_A(\text{ref.})} = e^{N\varepsilon\tau/\left[(1+\varepsilon)T_{1A}\right]} \frac{(1+\eta e^{-\alpha\tau})^N}{(1+\eta)^N} . \quad (26)$$

Experimental data for each set of conditions (orientation of crystal axes, ω_{eB}, and θ) were taken by measuring $S_D(N(\tau+\tau_0))/S_D(\text{ref.})$ at fifteen equally spaced τ-values $\tau_{max}/15 \leq \tau \leq \tau_{max}$, where $\tau_{max} \geq 3\tau_{AB}$. N was chosen to give a convenient range of dipolar signal variation and ran from as few as seven pulses up to about forty for the small-ε cases.

The B rf amplitude variation was held to a negligible amount with regulated power supplies and ω_{eB} was measured before and after each data set to within $\pm 2\pi\times 50\ \text{sec}^{-1}$ with the audio-resonance technique of the following section. Two values of $S_D[N(\tau+\tau_0)]$ were measured and averaged, and each set of data was then fitted to the exact counterpart of Equation (26) in the least-squares sense using an IBM 1620II computer, yielding experimental values for τ_{AB} and ε (the measured value $T_{1A} = 4.1$ sec was assumed throughout). In all cases the data were found to be consistent with the exponential decay factor $e^{-\alpha\tau}$ of Equation (26) to within the experimental scatter. Computed values of ε and τ_{AB} were found to be independent of N and of τ_{max} for $\tau_{max} \geq 3\tau_{AB}$.

Measured values of ε are plotted as a function of $f_{eB} \equiv (\omega_{eB}/2\pi)$ for $\underline{H}_o||[111]$ and $\underline{H}_o||[110]$ with $\theta = \pi/2$ in Figure 7, where the solid lines shown are plots of Equation (12) derived in Section II, i.e.,

$$\varepsilon = Cf_{eB}^2, \tag{27}$$

with

$$C = \frac{4\pi^2 \times 10^6 N_B S(S+1)}{N_A \gamma_A^2 H_{LA}^2 I(I+1)} ,$$

where f_{eB} is in kHz. For this purpose the isotopic abundance of Ca^{43} (= $2N_B/N_A$) was taken to be[26] 1.3×10^{-3} and the lattice sums in the expression for H_{LA}^2 were evaluated to 1 percent accuracy by computer. For the data of Figure 7 the saturating pulses were omitted, since M_B is entirely destroyed between pulses by the transverse decay process. The data points here are seen to follow the expected square-law dependence very closely, but with a slightly smaller coefficient of f_{eB}^2 than calculated. The calculated curves include the slight misorientation of the crystal discussed in Section III. The data of Figure 7 have been fitted to Equation (27) in the least-squares sense with the values of C so determined summarized in Table I. The ratios C_{exp}/C_{calc} are given in Table I and are seen to be nearly the same for both orientations. This suggests an error of +3.5 percent in the nominal isotopic abundance of ^{43}Ca, which is well within the error limits of previous determinations.[26]

Measurements of $\varepsilon(f_{eB})$ were also taken using saturating pulses with $H_o||(111)$ and $\theta = \pi/2$, $\pi/3$, $\pi/4$, and $\pi/6$. These data which were taken over the same frequency range as those

of Figure 7, are independent of θ, but deviate slightly from the f_{eB}^2 law for $f_{eB} < 4$ kHz. The latter effect is thought to be a spurious one associated with the saturating pulses, specifically that there may be a small difference in the effect of these pulses with and without the B rf measuring pulses. The effects of such a small difference would be intensified at low f_{eB} by the larger number of pulses applied in order to get a measurable effect. Fitting the $f_{eB} \geq 4$ kHz data to a power law $C = f_{eB}^n$, the values $C = 1.05\times10^{-3}$ $(\text{kHz})^{-2}$ and $n = 2.025$ are obtained. These are within experimental error of the no-saturating-pulse values, giving a satisfactory consistency between the two types of measurement.

The measured values of τ_{AB}^{-1} corresponding to the ε results of Figure 7 are plotted against $f_{1B}(\equiv \gamma_B H_1/2\pi)$ in Figure 8. Noting that $\tau_{AB} \to T_{2B}$ as $f_{1B} \to 0$, we also plot in Figure 8 values of $\tau_{AB}^{-1}(0)$ derived from measured values of T_{2B} (see Section VII). For both orientations the data are seen to vary quite closely as $\exp(-2\pi\alpha f_{1B})$; it is on this basis that the (Fourier transform) autocorrelation function was taken to be of the form of Equation (17), with the subsequent identification of α as τ_c. There is no a priori reason to expect this type of behavior, but it forms a convenient empirical framework with which to discuss our data. On the above basis, theoretical curves for τ_{AB}^{-1} vs. f_{1B} are obtained from Equations (16)

and (17) and are shown as the solid lines in Figures 8 and 9. Again, the lattice sums in the expression for $\langle \Delta\omega^2 \rangle_{AB}$ and τ_c were evaluated (including measured crystalline misorientation) to 1 percent accuracy by computer.

Deviations between this ad hoc theoretical form and the experimental data are seen to be of the order of or less than 15 percent. This is remarkably good, considering that there are no adjustable parameters once the form of the spectrum is fixed. The slopes of the calculated exponential spectra (i.e., τ_c) agree within 2 percent of the experimental values.

Data for τ_{AB} corresponding to the saturating-pulse ε-values discussed above were taken with $\underline{H}_o || [111]$ for four values of θ. These are plotted against f_{eB} in Figure 9. The solid lines shown are least-squares straight-line computer fits to the data points for each value of θ. The theoretical curve for $\theta = \pi/2$ plotted in Figure 8b is shown here as a dashed line. Agreement with the $\theta = \pi/2$ data is substantially the same as without saturating pulses. Behavior for $\theta \neq \pi/2$ is essentially unchanged with the curves shifted down corresponding to the factor $\sin^2\theta$ of Equation (17) and with minor variations in the slope (τ_c). A precise examination of the θ-dependence of the τ_{AB} spectrum may be made with the spectral area A defined in Section II (Equation (18)). Using the straight-line fits shown in Figure 9 to evaluate the experimental areas, we obtain the plot of A vs. $\sin^2\theta$ shown

in Figure 10. The $\sin^2\theta$ law is seen to hold within experimental error.

From the above results and discussion we conclude that the theory of the τ_{AB} process developed in Section II is basically correct, with an approximately exponential fluctuation spectrum, and with spin-diffusion effects largely absent. In the remainder of this section we turn our attention to the latter effect and to other more detailed matters relating to these data.

First we make a closer examination of the $\theta = \pi/2$ data of Figure 8, since these data are the most complete and accurate. It is seen that (a) in both cases the data points fall systematically below the theoretical curve, (b) that they do not form a perfectly straight line, but are slightly concave upward, and (c) for $\underline{H}_o || [110]$ the $f_{1B} = 0$ data point falls slightly below the intercept of a straight line through the other data. Considering effect (c) first, this "flattening" effect seems to be absent for the [111] data. However, the (111) point for $\tau_{AB}^{-1}(0)$ may actually lie somewhat lower than shown as suggested by the audio linewidth data of the next section, which gives a value of T_{2B} (dipolar) about 10 percent smaller than the T_{2B} measurements. As to the origin of this effect, it is very likely an intrinsic property of the actual fluctuation spectrum. Differentiation of Equation (14) with respect to ω_{eB} shows that the slope of the spectrum vanishes

at $\omega_{eB} = 0$ if

$$\int_0^\infty \tau^2 a(\tau) d\tau$$

is finite. Since the latter would seem to be a reasonable assumption, we then expect a leveling off of τ_{AB}^{-1} at low frequencies. The $\tau_{AB}^{-1}(0)$ data points indicate that this effect is of the order of 10 to 20 percent. Effect (b) is suggestive of spin-diffusion limiting of the τ_{AB} process, since the data is seen to bend downward just in the region (3-7 kHz) of maximum A-B system energy transfer ($\propto \varepsilon/\tau_{AB}$) which is also plotted in Figure 8. Such a conclusion is not supported by the data of Figure 9, however, where the slight curvature is seen to be present at all θ-values. A spin-diffusion effect would be expected to diminish at the smaller θ-values, where the rate of energy transfer is greatly reduced. Of course, it is possible that this curvature is simply an intrinsic feature of the spectrum. A third possibility is that the τ_{AB}^{-1} values rise upward at lower frequencies because of the onset of higher-order contributions to the rate. Such effects are expected to be smaller than the simple "golden rule" process by a ratio of roughly τ_c/τ_{AB}. This ratio shows a definite increase at lower frequencies and has a maximum value of about 0.15 for the [111] data of Figure 9. The

maximum ratio τ_c/τ_{AB} is smaller for $\underline{H}_o||[110]$ by a factor of almost 3, so that one expects a much smaller curvature for this orientation. Though this does not seem to be the case, the data are really not accurate enough to resolve this question. We can neither confirm nor deny the presence of these higher-order processes from these results. Finally, as to effect (a), this would seem to be the clearest indication of spin-diffusion limiting obtainable from the present data. By fitting straight-line segments to the spectra of Figures 8 and 9 we obtain estimates of the experimental spectral area A defined by Equation (18). These are compared with calculated values $A = (\pi/2)\langle\Delta\omega^2\rangle_{AB}\sin^2\theta$ in Table II, where they are seen to be smaller by amounts of the order of the estimated experimental uncertainty ~10 percent. The major source of uncertainty in the experimental A-values arises from the paucity of data in the 0 - 2 kHz region, where a great deal of the area is located. Nonetheless, this is taken to be evidence for a small, but definite amount of spin-diffusion inhibition of the τ_{AB} process. The effect was slight enough so that no change in the functional form (e.g., Equation 26) used to analyze the data was found. The experimental areas A from **Figure** 9 are also tabulated and compared with theory in Table II, where a similar area discrepancy is found, though the data are not as accurate. Interestingly, we find here a trend of less area discrepancy at smaller angles and smaller τ_{AB}^{-1} rates, as would be expected for a spin-diffusion inhibition effect. Also listed in Table II are the

TABLE I

Orientation		θ	C(calculated)	C_{exp}/C_{calc}
Figure 7	[110]	$\frac{\pi}{2}$	$0.505\times10^{-3}(\text{kHz})^{-2}$	0.96 ±.03
	[111]	$\frac{\pi}{2}$	$1.066\times10^{-3}(\text{kHz})^{-2}$	0.97 ±.03

TABLE II

Orientation		θ	A(calculated)	A_{meas}/A_{calc}	τ_c(calc)	τ_c(meas)
(Figure 8a)	[110]	$\frac{\pi}{2}$	$4.26\times10^{7}(\text{sec})^{-2}$	0.89	58 μsec	57 ±.5 μsec
(Figure 8b)	[111]	$\frac{\pi}{2}$	$5.61\times10^{7}(\text{sec})^{-2}$	0.92	77 μsec	78 ±1 μsec
(Figure 9)	[111]	$\frac{\pi}{2}$	$5.61\times10^{7}(\text{sec})^{-2}$	0.84	77 μsec	80 ±1 μsec
	[111]	$\frac{\pi}{3}$	$4.21\times10^{7}(\text{sec})^{-2}$	0.86	77 μsec	79 ±1 μsec
	[111]	$\frac{\pi}{4}$	$2.50\times10^{7}(\text{sec})^{-2}$	0.87	77 μsec	76 ±1 μsec
	[111]	$\frac{\pi}{6}$	$1.35\times10^{7}(\text{sec})^{-2}$	0.99	77 μsec	76 ±1 μsec

calculated and measured correlation times τ_c from the slopes of the semilog spectral plots. Although these may be affected by spin-diffusion and other small effects, agreement between theory and experiment is seen to be excellent.

V. ROTARY SATURATION DOUBLE RESONANCE (RSDR)

In this section we study an alternative scheme for carrying out rotating frame double resonance experiments, in which the B-spin energy reservoir is continuously heated by means of rotary saturation[5,15] as opposed to the pulse modulation method of the previous section. The RSDR method has the advantages of a greater potential double-resonance rate of A-spin heating and a greater precision in determining the rare-spin Larmor frequency. It is also useful for making accurate measurements of the rotating frame effective field H_e.

In this technique a single burst of B-rf field H_1 is applied to the specimen (following ADRF preparation of the A-nuclei) for a time τ_B of the order of T_{1A} or shorter if the double-resonance effect is strong (see Figure 11). During this period the rotating-frame effective field H_e is established in accordance with Equation (3). Simultaneously with the burst of H_1, the audio-frequency field $H_a \cos \omega_a t$ is applied parallel to $\underline{H}_o$. If ω_a is set equal or near to the rotary-saturation resonance frequency $\omega_{eB} = \gamma_B H_e$, the component $H_a \sin \theta$ of audio field at right angles to $\underline{H}_e$ will cause a net absorption of energy by the B-spins. The energy influx is then passed on to

the A-nuclei by the τ_{AB} process (see Figure 2) and produces a measurable increase in T_A.

It is possible to observe two different types of double resonance spectra with this method. In the first, illustrated in Figure 12, the A-spin signal S_D is monitored while the frequency ω at which H_1 is applied is stepped through the region of the B-spin Larmor frequency $\gamma_B H_o$. The audio frequency ω_a as well as the fields H_a, H_1, and H_o are kept constant. For $\omega_a \lesssim \gamma_B H_1$ the rotary-saturation resonance condition is most nearly satisfied for $\omega = \gamma_B H_o$, giving rise to the spectrum having a single peak of A-spin heating in Figure 12. For $\omega_a > \gamma_B H_1$ the audio-resonance condition will be satisfied for two values of ω symmetrically displaced from $\gamma_B H_o$ according to the formula $\omega_\pm = \gamma_B H_o \pm \sqrt{\omega_a^2 - \gamma_B^2 H_1^2}$. This condition leads to the double peak in Figure 12. The data of Figure 12 may be used in conjunction with the measured Larmor frequency of the ^{19}F nuclei in the same applied field H_o to determine γ_B. The result is $\gamma_B/2\pi = 0.28657 \pm 0.00004$ kHz/gauss or (0.035 ±0.02) percent larger than the value $\gamma(^{43}Ca)/2\pi = 0.28647 \pm 0.00003$ kHz/gauss determined by Jeffries[27] for the Ca^{2+} ion in solution. This disparity, although poorly resolved here, is ascribed to variations in the ^{43}Ca chemical shift between aqueous solution and the crystalline environment of the Ca^{2+} ion in CaF_2.[28]

In contrast to Figure 12 we may observe the rotary-saturation spectrum by sweeping the frequency ω_a with all other parameters fixed. An example of this is shown in Figure 13. Such a spectrum is useful for determining the value of H_e as well as to investigate sources of rotating-frame line broadening. We note that the effect of secular dipolar coupling terms on the rotary saturation spectrum is quite different in the present case of rare nuclei from that for abundant spin systems. Here, because of the absence of interactions between B-spins and because of the relatively weak A-B coupling, we expect a very nearly symmetrical absorption line centered at frequency ω_{eB} for effective fields such that $\omega_{eB}T_{2B} >> 1$ where $1/T_{2B} = \pi/2 \langle\Delta\omega^2\rangle_{AB}\tau_c$. This inequality holds throughout the present work. In contrast, the rotary saturation spectrum of the ^{19}F in CaF_2[15] is asymmetrical and shifted to higher frequencies for $H_e \lesssim H_{LA}$.

The process of rotating-frame audio-energy absorption has been described in detail.[5,15] This process is closely analogous to conventional laboratory-frame NMR absorption, with the roles of dc magnetic field, rf magnetic field, and T_1 played here by H_e, $H_a \sin\theta$, and τ_{AB}, respectively. As discussed in Section II the rotary saturation process may be characterized by a saturation time-constant τ_a given by Equation (10). We note that the factor ω_a/ω_{eB} in Equation (10) is the only source of asymmetry in the audio-absorption spectrum.

It gives rise to at most a 6 percent shift in the audio-resonance peak in the present work.

With the above formulation the RSDR method may be used to measure values of the fundamental double-resonance rate ε/τ_{AB} of the spin-temperature model of Section II.[29] For $\varepsilon << 1$ and weak A spin-lattice coupling $(T_{1A}(\tau_{AB}^{-1} + \tau_a^{-1}) >> 1)$ an approximate solution to the coupled Equations (11) may be obtained by setting $\dot{\beta}_B = 0$ and substituting the resulting expression $\beta_B = (\tau_a/(\tau_a+\tau_{AB}))\beta_A$ into Equation (11b) to find the double-resonance contribution to the decay rate of β_A

$$\frac{d}{dt}\beta_A \cong -\left[\frac{\varepsilon}{(\tau_a+\tau_{AB})} + \frac{1}{T_{1A}}\right]\beta_A. \qquad (28)$$

Equation (28) is sufficiently accurate to describe the bulk of the results presented in this section. Data for the rate contribution $\varepsilon/(\tau_a+\tau_{AB})$ was obtained by comparing the A-spin dipolar signal $S_D(\tau_B) = S_{D0}\exp[-\varepsilon\tau_B/(\tau_a+\tau_{AB}) - \tau_B/T_{1A}]$, obtained with a pulse of H_1, H_a of duration τ_B, with a reference signal $S_D(\text{ref.}) = S_{D0}e^{-\tau_B/T_{1A}}$ obtained by simply omitting the pulses of H_1 and H_a from the timing sequence of Figure 5. The resulting ratios $S_D(\tau_B)/S_D(\text{ref.}) = e^{-\varepsilon\tau_B/(\tau_a+\tau_{AB})}$ were found to vary exponentially with τ_B as expected, giving experimental values of the double resonance rate $T_{AB}^{-1} = \varepsilon/(\tau_a+\tau_{AB})$, which may be written

$$\frac{1}{T_{AB}} = (\varepsilon/\tau_{AB}) \frac{S}{1+S} , \qquad (29)$$

where $S = \tau_{AB}/\tau_a$ is the conventionally defined saturation parameter. The strongest double-resonance effect is obtained for large values of ω_{1a} in Equation (10) such that $\tau_a << \tau_{AB}$, or $S >> 1$, for which $T_{AB} \rightarrow \tau_{AB}/\varepsilon$.

Since the high saturation level condition $S >> 1$ could not always be maintained, use was made of the H_a^2 dependence of S in order to extract values of τ_{AB}/ε from the data. For this purpose the induced voltage V_{sc} across a search coil placed near the CaF_2 specimen was taken as a measure of H_a. This procedure was necessary because H_a was found to be a complicated function of audio-coil current and frequency on account of proximity to the magnet pole faces. In an independent calibration the relation $V_{sc} = \kappa\omega_a H_a$ (κ = constant) was found to be satisfied to within 2 percent. Combining this expression with Equations (10) and (29) gives

$$V_{sc}^2 T_{AB} = K + V_{sc}^2 \tau_{AB}/\varepsilon \qquad (30)$$

where the form of the constant K is irrelevant to the present discussion. By plotting measured values of $V_{sc}^2 T_{AB}$ against V_{sc}^2, τ_{AB}/ε is obtained as the slope of the resulting straight line. Figure 14 shows such a plot for ^{43}Ca in CaF_2 with

$\underline{H}_o||[111]$, $\theta = \pi/4$, and $f_{eB} = 8.0$ kHz, yielding $\tau_{AB}/\varepsilon = 0.40$ sec. At the top of the plot an experimental scale of values for the saturation parameter S is shown, where we note $S = V_{sc}^2 \tau_{AB}/\varepsilon K$ in the notation of Equation (30). These values of S, derived from the straight-line interpretation of the data of Figure 14, are to be compared with an estimate of $S = \tau_{AB}/\tau_a$ based on Equation (10) using a Lorentzian lineshape function

$$f_a(\omega_a) = \left[T_{2a}^*/\pi\right]\left[1 + (\omega_a-\omega_{eB})^2 T_{2a}^{*2}\right]^{-1}. \qquad (31)$$

At exact resonance we find the familiar result $S = \omega_{1a}^2 T_{2a}^* \tau_{AB}$. With a rough calibration of H_a using the search coil and measured values of τ_{AB} and T_{2a}^* (see below), this formula gives S-values within 20 percent of the experimental ones. The saturation levels given in Figure 14 are typical of those encountered in the RSDR studies reported here.

Experimental values of τ_{AB}/ε were obtained in the above fashion for a variety of θ- and f_{eB}-values with $\underline{H}_o||[111]$. In order to compare these results with the plots of τ_{AB}^{-1} vs. f_{eB} obtained by the pulse method of Section IV (Figures 8 and 9), the τ_{AB}/ε data were first multiplied by corresponding ε-values taken from the experimental calibration of ε vs. f_{eB} given in Figure 7. Since the ε data are quite accurate, a negligible error is introduced by this step. The τ_{AB} values derived in

this fashion were then inverted and plotted on a semilogarithmic scale vs. f_{eB} in Figure 15. The straight line fits to the pulse-method data of Figure 9 for corresponding θ-values are drawn in for comparison. A good corresponence with the exponential τ_{AB}^{-1} rate "spectrum" displayed by the pulse-method data is seen to hold, with the exception of the $\theta = \pi/2$, $f_{eB} = 4$ kHz data point, which lies well below the corresponding data of Figures 9 and 8b. This discrepancy may well be a result of spin-diffusion limiting, which is expected to be most severe for these values of angle and frequency. Moreover, the bottleneck effect is expected to be greater in the rotary saturation method, since the peak energy transfer condition now persists for the entire duration of B-spin irradiation time, rather than only briefly at the beginning of each pulse as in the method of Section IV. For example, the experimental rate of A-spin heating T_A d/dt (T_A^{-1}) for $\theta = \pi/2$, $f_{eB} = 4$ kHz is found to be ~6.6 sec^{-1} with RSDR as compared with ~2.3 sec^{-1} in the corresponding pulse measurement of Figure 8b, leading undoubtedly to intensified spin-diffusion limiting in the former case. The $\theta = \pi/4$, $\pi/6$ data points also tend to pass beneath the pulse data at $f_{eB} = 4$ kHz, but overall agreement is within the experimental scatter.

An investigation of audio-frequency linewidths such as displayed in Figure 13 was carried out in conjunction with the RSDR measurements of this section. These linewidth results

supplement the T_{2B} measurements of Section VII and reveal the presence of a small quadrupolar broadening of the ^{43}Ca NMR line, an effect not observable by other means.

Experimental linewidth data were taken by varying ω_a with the parameters H_1, H_a, and θ at fixed values (see Figure 13). These data were reduced by first correcting the raw RSDR data for the effect of T_{1A} and other small effects associated with the exact solution of Equations (11) in the present circumstances,[25] and then fitting the values of T_{AB} so obtained to Equation (29), where S is proportional to $f_a(\omega_a)$ in the formulation of Equation (10). Lineshape data were computer-fitted to an assumed Lorentian form for $f_a(\omega_a)$ (Equation (31)) in the least-squares sense, giving a reasonable representation of the data in all cases. Results for the measured half-width at half-minimum for $\underline{H_o}||[111]$ are plotted against f_{eB} for three different values of θ in Figure 16.

The various sources of audio-line broadening may be examined with the rotating-frame Hamiltonian Equation (3). To this we add a term to represent stray quadrupole couplings. Assuming these are small compared to $\bar{\gamma}_B H_e$, the one secular term may be written in the laboratory frame as $\mathcal{H}_B^Q = AS_z^2$. In the tilted reference frame of Equation (3) this becomes $\mathcal{H}_{BR}^Q = 0.5\ A(3\cos^2\theta - 1)S_Z^2$ neglecting (rotating-frame) nonsecular terms. The coefficient A is proportional to the ^{43}Ca quadrupole

moment and to the electric field gradient at a given B-spin site. In considerations to follow we treat A as a random variable with (for convenience) a Gaussian distribution of values over the B-spin sites of the crystal.

With a total Hamiltonian $\mathcal{H}_R + \mathcal{H}^Q_{BR}$ we identify four sources of audio-line broadening:

(a) Homogeneous dipolar broadening from the third ($\cos\theta$) term in Equation (3). This term (with $\theta = 0$) is primarily responsible for the T_{2B} decay process studied in Section VII. It is modulated in time by the $\mathcal{H}^{AA}_d$ coupling, giving rise to an essentially Lorentzian line of half-width $\cos^2\theta/T_{2B}$.

(b) An effective "lifetime" broadening from the nonsecular fourth ($\sin\theta$) term of $\mathcal{H}_R$. This term is responsible for the τ_{AB} process as shown in Section II. Here we estimate its effect on the audio linewidth by noting that it would cause an audio "free-precession decay" of exponential form with time constant $2\tau_{AB}$. The factor 2 occurs because the perturbation acts effectively for only half of the time on a moment precessing about the Z-axis. This effect alone would therefore give a Lorentzian line of half-width $1/2\tau_{AB}$.

(c) Inhomogeneous broadening from stray quadrupole couplings to be discussed in detail below.

(d) Broadening from inhomogeneities in the applied Brf field H_1. This effect was minimized with a special

coil design discussed in Section III. Correspondingly no linewidth contribution $\propto H_1$ was observed and we place an upper limit of $\sim 2\times10^{-3}\ H_1$ on rf inhomogeneity. Droop and ripple on the B-rf pulses were negligible.

With the above considerations in mind, then, we examine the audio-linewidth data shown in Figure 16.

The $\theta = \pi/2$ data show a roughly constant linewidth $\cong$ 120 Hz over the frequency range studied. Since the homogeneous broadening term $\propto \cos^2\theta$ vanishes for this case, the major contribution is attributed to stray quadrupole couplings. It is notable that the lifetime-broadening term (solid line for $\theta = \pi/2$) is apparently absent from the data. The reason for this is not understood.

In Section VII the quadrupolar broadening in evidence here is found to affect the decay time T_{2B} primarily through its contribution to the second moment M_2^Q. In order to relate the measured audio-resonance half-width to M_2^Q, it is necessary to adopt some model of the quadrupolar-broadened audio lineshape $g_Q(\omega)$. Since $g_Q(\omega)$ is found to be approximately Lorentzian, the simplest such model would be a cut-off Lorentzian, with the half-width and cut-off point determined by calculated second and fourth moments. We reject this model as unsatisfactory here for two reasons. First, it is found to misrepresent the calculated sixth moment by about an order of magnitude. Second, it has been found[17] to systematically underestimate

the half-width of dynamically broadened resonance lines by a factor of two or three. An alternative two-parameter model is developed in Appendix B, based on the assumed form $\exp[c(a - \sqrt{a^2+t^2})]$ for the Fourier transform of $g_Q(\omega)$. The constants c and a are easily related to M_2^Q and M_4^Q, leading to a sixth moment very nearly equal to a calculated estimate. Moreover, the resulting $g_Q(\omega)$ is found for the parameters c and a so determined to be very nearly Lorentzian over frequencies ranging by twice the half-width from center. These points are illustrated in detail in Appendix B. The relation between M_2^Q and the measured half-width $\Delta\omega_{half}$ is found there to be $M_2^Q = 1.40(\Delta\omega_{half})^2$. With the observed value $\Delta\omega_{half} = 2\pi\times120\ \mathrm{sec}^{-1}$, we obtain $M_2^Q(\theta = \pi/2) = 8.0\times10^5\ \mathrm{sec}^{-2}$. This result will be utilized in Section VII to interpret measured T_{2B} values.

For $\theta = \pi/4$ and $\pi/6$ the predominant linewidth contribution comes from the homogeneous $\cos^2\theta/T_{2B}$ term. The quadrupolar contribution is greatly reduced at these angles owing to the θ-dependence of $M_2^Q(\propto(1-3\cos^2\theta)^2)$. Solid lines are plotted in Figure 16 showing a combined estimate of dipolar and quadrupolar contributions summed with the $(2\tau_{AB})^{-1}$ term. Again the latter term does not appear to be present in the data, though it is not clearly resolved. The $\cos^2\theta/T_{2B}$ term was evaluated using experimental data for T_{2B} given in Section VII, with the quadrupolar correction calculated with the scheme developed there. This correction amounts to ~1.5 percent

and < 1 percent of the dipolar part for $\theta = \pi/4$ and $\pi/6$ respectively. The $\theta = \pi/4$ results suggest that T_{2B} is slightly longer for $H_o || [111]$ than the value found in Section VII, though the agreement is within experimental uncertainty.

The simple BPP theory [14] of saturation summarized by Equations (10) and (29) has been found to give a satisfactory account of the rotary-saturation phenomena investigated here, even at relatively high saturation levels $S = \tau_{AB}/\tau_a >> 1$. On the other hand Franz and Slichter[15] gave a good account of ^{19}F rotary saturation phenomena in CaF_2 by describing the state of the nuclear spins with a spin-temperature in the <u>second</u> rotating frame, i.e., in a frame rotating about the Z-axis at frequency ω_a. We show here that the latter description for our rare-spin case leads to an audio-absorption spectrum that is approached asymptotically by the BPP result at high saturation levels.

There are two important differences between the rare and abundant spin cases considered. First, there is no dipolar "local field" for the rare spins because their like-spin coupling is negligibly weak. Second, there is only negligible coupling with the lattice directly, and the A-spins become an effective "lattice" with longitudinal and transverse

"spin-lattice" relaxation times τ_{AB} and $T_{2a} = T_{2B}/\cos^2\theta$, respectively (ignoring questions of inhomogeneous broadening). Under these circumstances the problem of dynamic equilibrium in the second rotating frame becomes closely analogous to the case of rotating frame equilibrium with anisotropic spin-lattice relaxation considered by Abragam. We take his results over directly[29] to find an equilibrium magnetization along the audio-"effective field" $\underline{H}_{ea} = \hat{i}'H_{1a} + \hat{k}\Delta H_a$ given by

$$M_{oa} = \frac{M_o \Delta H_a H_{ea} T_{2a}^2}{\left(\Delta H_a^2 T_{2a}^2 + H_{1a}^2 \tau_{AB} T_{2a}\right)} \tag{32}$$

where $\Delta H_a = (\omega_a - \omega_{eB})/\gamma_B$, and $M_o = M_B(T_A)$ as defined in Equation (8). $\hat{k}$ and $\hat{i}'$ are unit vectors along the Z-axis and along an axis $\perp \hat{k}$ and rotating at a frequency ω_a, respectively. With Equation (32) we evaluate the steady-state energy influx to the A-spins as $H_e(M_o - M_Z)/\tau_{AB}$ with $M_Z = M_{oa}\Delta H_a/H_{ea}$. Equating this expression to $d/dt\ E_A = -\ E_A/T_{AB}$, we find

$$\frac{1}{T_{AB}} = \frac{\varepsilon \omega_{1a}^2 T_{2a}}{\Delta\omega_a^2 T_{2a}^2 + \omega_{1a}^2 T_{2a} \tau_{AB}} \tag{33}$$

for the audio-lineshape function under extreme saturation conditions, where $\Delta\omega_a = \gamma_B \Delta H_a$. For comparison we write out Equation (29) for a Lorentzian lineshape (Equation (31)):

$$\frac{1}{T_{AB}} = \frac{\varepsilon\omega_{1a}^2 T_{2a}}{1 + \Delta\omega_{1a}^2 T_{2a}^2 + \omega_{1a}^2 T_{2a}\tau_{AB}} \qquad (34)$$

In the limit of extreme saturation $\omega_{1a}^2 T_{2a}\tau_{AB} >> 1$, so that Equation (34) approaches Equation (33) asymptotically. Thus the assumption of spin quantization in the second rotating frame introduces no significant modification of the simple BPP theory in the present case.

VI. TRANSIENT OSCILLATIONS IN THE ROTATING FRAME

In performing the pulsed double-resonance experiments it was noted that the initial behavior of the rotating-frame magnetization M_B consisted (at large f_{1B}) of a small step function accompanied by short-lived (lifetime $\sim\tau_c$) oscillations of similar magnitude at frequency f_{1B}. Physically, these phenomena represent the change in the energy of the Hamiltonian term H_d^{AB} (Equation (1)) in response to the rf field H_1. They are closely analogous to the oscillatory behavior of the laboratory magnetization in response to a pulsed dc field investigated by Strombotne and Hahn.[16] In this section we develop an approximate theory for these oscillations and show that they constitute in principle a powerful method of nuclear double resonance quite distinct from those discussed in earlier sections of the paper. The B-spin irradiation sequence is as shown in Figure 6.

To calculate the initial behavior of M_B upon application of an rf pulse we begin with the rotating-frame Hamiltonian Equation (3), omitting the irrelevant audio term and assume throughout that H_1 is applied at exact resonance ($\theta = \pi/2$). Thus Equation (3) becomes

$$\mathcal{H}_R = \mathcal{H}_d^{AA} - \omega_{1B} S_Z + S_X \sum_i B_i I_{zi}. \tag{35}$$

In the absence of $H_1 (\omega_{1B} = 0)$ the remaining two terms of Equation (35) achieve thermal equilibrium as a composite dipolar energy reservoir in a time of the order of τ_c. We represent this (initial) state of the combined A- and B-spin dipolar terms with a density matrix

$$\rho_{Ri} \cong \frac{1}{Tr(1)} - \frac{\hbar}{kT_{Ai} Tr(1)} \left[\mathcal{H}_d^{AA} + S_X \sum_i B_i I_{zi} \right], \tag{36}$$

using the high-temperature approximation as in Equation (6) with an initial spin-temperature T_{Ai}. After the pulse field H_1 is applied, ρ_R develops in time according to Equation (2) with an initial value given by Equation (36). Since $\mathcal{H}_R$ is explicitly time-independent, the formal solution to Equation (2) is found immediately to be

$$\rho_R(t) = e^{i\mathcal{H}_R t} \rho_{Ri} e^{-i\mathcal{H}_R t}. \tag{37}$$

It follows from (37) that the total rotating-frame nuclear spin energy is conserved during the pulse, i.e.,

$$\langle \mathcal{H}_R \rangle = \mathrm{Tr}\left[\rho_R(t)\mathcal{H}_R\right] = \langle \mathcal{H}_R \rangle_i = \mathrm{Tr}(\rho_{Ri}\mathcal{H}_R). \tag{38}$$

At the end of the pulse, however, an amount of work $\omega_{1B}\langle S_Z \rangle$ is done on the system in turning off H_1, leaving a final nuclear spin energy

$$\langle \mathcal{H}_R \rangle_f = \mathrm{Tr}\left[\rho_R(\tau)\left(\mathcal{H}_d^{AA} + S_X \sum_i B_i I_{zi}\right)\right] \tag{39}$$

where τ is the pulse width. The increase in nuclear spin energy, $\langle \mathcal{H}_R \rangle_f - \langle \mathcal{H}_R \rangle_i$, leads, upon application of many pulses, to a measurable increase in T_A. The experiments performed to observe this effect were of the same format as those of Section IV, with the pulses used being shorter ($\tau \sim \tau_c \ll \tau_{AB}$) and with many more of them required

$$\left(N \sim \frac{\mathrm{Tr}\left(\mathcal{H}_d^{AA}\right)^2}{N_B \mathrm{Tr}\left(\mathcal{H}_d^{AB}\right)^2} \sim 10^3 \right)$$

to produce a measurable effect.

As the exact formal expression for $\rho_R(\tau)$ (Equation (37)) is not suitable for a practical calculation of

$\langle H_R \rangle_f$, we use a perturbation expansion of $\rho_R(\tau)$ to second order in the A-B interaction H_p (Equation (4)) to find an approximate expression for $\rho_R(\tau)$. Standard techniques give

$$\rho_R(\tau) \cong T(\tau)\left\{\rho_{Ri} - i\int_0^\tau dt'[H_p(t'),\rho_{Ri}] - \int_0^\tau dt' \int_0^{t'} dt''\left[H_p(t'),[H_p(t'-t''),\rho_{Ri}]\right]\right\}T^\dagger(\tau) \tag{40}$$

where $H_p(t) = T(t)H_pT^\dagger(t)$ and $T(t) = e^{i(H_d^{AA}-\omega_{1B}S_Z)t}$. This expansion is valid under the same "extreme narrowing" assumption used to derive Equation (13), with the additional requirement that $\tau/\tau_{AB} << 1$. Combining Equations (39) and (40) and using the definitions of the correlation function a(t) (Equation (14)) and ρ_{Ri} (Equation (36)), we obtain

$$\langle H_R \rangle_f = -\frac{\hbar}{kT_{Ai}Tr(1)}\left[Tr\left(H_d^{AA}\right)^2 + Tr(H_p)^2F(\tau)\right] \tag{41}$$

with

$$F(\tau) = a(\tau)\cos(\omega_{1B}\tau) - 2\int_0^\tau dt' \cos(\omega_{1B}t')\frac{da(t')}{dt'} + \int_0^\tau dt' \int_0^{t'} dt'' \cos(\omega_{1B}t'')\frac{d^2a(t'')}{dt''^2}. \tag{42}$$

We may now claculate the change in T_A caused by a single rf pulse by observing that the nuclear spins will revert in a time $\sim\tau_c$ to a thermal equilibrium state with energy $\langle H_R \rangle_f$ and spin-temperature T_{Af} (analogous to Equation (36)) following the end of the pulse. The latter quantities are related by

$$\langle H_R \rangle_f = \frac{-\hbar}{kT_{Af}\mathrm{Tr}(1)} \left[\mathrm{Tr}\left(H_d^{AA}\right)^2 + \mathrm{Tr}(H_p)^2 \right]. \qquad (43)$$

By equating expressions (41) and (43) the fractional decrease in A-spin signal S_D per pulse is found to be

$$\delta(\tau) = 1 - \frac{T_{Ai}}{T_{Af}} = \frac{N_B \mathrm{Tr}(H_p)^2}{\mathrm{Tr}\left(H_d^{AA}\right)^2} \left(1 - F(\tau)\right), \qquad (44)$$

where the factor N_B has been inserted to obtain the effect of all B-spins in the crystal. $\delta(\tau)$ is seen to consist of a fixed parameter $N_B\mathrm{Tr}(H_p^2)/\mathrm{Tr}(H_d^{AA})^2$ multiplying a time-varying function $(1 - F(\tau))$ which is (initially) of order unity. The multiplying parameter is easily evaluated for CaF_2 with $\underline{H}_o||[111]$ to be 1.07×10^{-3}. Of the three terms of $F(\tau)$, the first two are purely oscillatory and decay to zero or a relatively small value in a time $\sim\tau_c$. The third term is also oscillatory for $\tau \sim \tau_c$, but for $\tau >> \tau_c$ its slope approaches ε/τ_{AB}. This is not surprising because Equation (40) is an approximation to the exact formal solution of the entire A-B

cross-relaxation process, and therefore must contain the beginning of the exponential τ_{AB} equilibrium process. The asymptotic behavior of this final term represents the onset of the exponential approach to A-B equilibrium contained in Equation (11).

To compare the oscillations with the exponential process we set apart the term of Equation (44) which is $\propto \tau$ and define a new function $O(t)$:

$$\delta(\tau) = 1.07\times10^{-3}O(\tau) + \frac{\varepsilon\tau}{\tau_{AB}} \qquad (45)$$

$O(t)$ is a function which is ~ 1 for $\tau \sim \tau_c$ and contains oscillatory terms at frequency ω_{1B} which decay in a time $\sim\tau_c$. The first term of Equation (45) has at large f_{1B} the step-plus-oscillation form noted earlier and represents purely the effect of the H_1 pulse on the thermodynamic state of the A-B coupling term ($\mathcal{H}_p$). Thermodynamic reservoir calculations show that including $\mathcal{H}_p$ in the calculation of Section II changes the theoretical value of ε only by a fractional amount

$$\sim \mathrm{Tr}\left\{\left(\mathcal{H}_d^{AB}\right)^2\right\} \Big/ \mathrm{Tr}\left\{\left(\mathcal{H}_d^{AA}\right)^2\right\} \sim 0.1\%.$$

Therefore the step behavior characteristic of the short time solution (Equation (44)) vanishes for long times $\tau \gg \tau_c$ when all perturbation terms are taken into account.

Data for the oscillation effect has been taken for $\omega_{1B}/2\pi$ = 12.6 kHz and 2.43 kHz. Values of $\delta(\tau)$ were obtained from A-spin signals $S_D(N,\tau)$ and S_{Do} measured with and without a train of N pulses, respectively, using the formula $S_D(N,\tau)/S_{Do} = (1 - \delta(\tau))^N \cong e^{-N\delta(\tau)}$. Experimental plots of δ vs. τ are shown in Figures 17(a) and (b) for the cases mentioned. The solid lines drawn are obtained from machine calculations of $1 - F(\tau)$, using Equation (42). The 12.6 kHz data of Figure 17(a) clearly demonstrate the structure of Equation (45) with the step, slope, and oscillation amplitude in good accord with the theory. Again, the experimentally determined form of a(t) is crucial in the successful calculation of this effect. The 2.43 kHz data of Figure 17(b) is in poorer agreement, mainly because the range of τ values (0.9 msec) is of the order of $\tau_{AB} \sim 0.5$ msec. A significant improvement in agreement here is achieved by simply replacing the final term in Equation (45) with its full exponential form given in the previous paragraph (solid line in Figure(17b)). The residual discrepancy may result from the extreme narrowing assumption being only marginal here ($\tau_{AB}/\tau_c \sim 4$).

We conclude this section by noting that the initial behavior of M_B studied here may be employed as a double-resonance technique with a comparable effectiveness to those of Sections IV and V. For very large values of ω_{1B} ($\omega_{1B}\tau_c >> 1$) one has for $\tau << \tau_c$, $\delta(\tau) \cong 1.07\times10^{-3}$ $(1 - \cos \omega_{1B}\tau)$.

Adjusting $\omega_{1B}\tau = \pi$ and making use of the rapid recovery of the thermodynamic equilibrium following a pulse by applying pulses at a rate $R \sim \tau_c^{-1}$, one can in principle obtain double-resonance rates of the order of $R\delta(\pi/\omega_{1B}) \sim 20\ \mathrm{sec}^{-1}$. It is noteworthy that this estimate is about twice the maximum values of ε/τ_{AB} for the CaF_2 system, the latter being the strongest effect obtainable by the technique of Sections II-IV. It is easy to show that these two double-resonance schemes, although quite different at the level of detailed physics involved, have in general a comparable sensitivity independent of the nuclear moments and crystalline structure parameters.

VII. MEASUREMENT OF T_{2B}

The decay function of the unobservable rare-spin free precession signal can be experimentally determined in a simple and reliable fashion using a modified version of the pulsed double-resonance method of Section IV. In this section we present a simple formulation of this technique and apply it to the measurement of T_{2B} for ^{43}Ca in CaF_2. The ^{43}Ca T_2 process is virtually identical with the τ_{AB} process of Section II for $\theta = \pi/2$ in the limit $\omega_{eB} \to 0$. Such a correspondence is required physically, because the decay time (τ_{AB}) of M_B must approach T_{2B} for $H_1 \to 0$. As commented in Section II, the extreme narrowing assumption for this case is marginal. We therefore treat the full T_{2B} decay process with the motional narrowing model of Anderson and Weiss.[13]

The measurements are carried out with the B rf pulsing sequence of Figure 6 applied during the B-spin irradiation time of Figure 5. Using a fixed number N of pulses as before, the pulse width τ is now adjusted so that complete A-B thermal equilibrium is achieved during each pulse ($\tau >> \tau_{AB}$), in order to simplify the data analysis. The pulse spacing τ_o is made small enough so that the decay of M_B between pulses is incomplete, thus forming an initial condition for the next pulse. Since the Brf waveform is coherent from pulse to pulse, each pulse will immediately "lock" the residual precessing M_B vector from the preceding pulse along H_1, and A-B thermal equilibration will begin again via Equations (11). The frequency ω of the Brf must, of course, be adjusted to equal $\gamma_B H_o$ within a small fraction of $1/T_{2B}$ for the scheme to work smoothly. Under the above circumstances the A-spin warmup rate will be a function of the pulse separation τ_o and can be analyzed to determine the transverse decay function $f(\tau_o)$ that describes the behavior of M_B between pulses.

To find the value of β_A at the end of the pulsing sequence we may conveniently omit the T_{1A} term from Equations (11) and approximate its effect with the simple factor $\exp\{-[N\tau + (N-1)\tau_o]/T_{1A}\}$ which would apply in the absence of Brf. In doing this we are omitting a factor $\exp\{\varepsilon\tau/(1+\varepsilon)T_{1A}\}$ in the analysis. With $\varepsilon << 1$ and $\tau << T_{1A}$ this factor is very nearly unity. Equations (11) then reduce (with $\tau_a^{-1} = 0$) to

$$\frac{d}{dt}(\beta_A-\beta_B) = -(1+\varepsilon)(\beta_A-\beta_B)/\tau_{AB} \tag{46a}$$

and

$$\frac{d}{dt}(\beta_A+\varepsilon\beta_B) = 0 \tag{46b}$$

during each pulse. With $\tau >> \tau_{AB}$ we have $\beta_A = \beta_B = \beta_n$ at the end of the nth pulse from Equation (46a). Between pulses β_A is constant and β_B (i.e., M_B) decays by a factor $f(\tau_o)$. Equation (46b) then gives $\beta_{n-1}(1 + \varepsilon f(\tau_o)) = \beta_n(1+\varepsilon)$, $n > 1$. At $t = 0$, $\beta_B = 0$, giving $\beta_1 = \beta_{Ai}(1+\varepsilon)^{-1}$. Thus at the end of the pulsing sequence we find

$$\beta_N = \beta_A\left[N\tau + (N-1)\tau_o\right] = \beta_{Ai}\frac{\left[1 + \varepsilon f(\tau_o)\right]^{N-1}}{(1+\varepsilon)^N} \cdot e^{-[N\tau + (N-1)\tau_o]/T_{1A}} \tag{47}$$

including the approximate T_{1A} decay factor. Data is again taken by comparing the A-spin signal $S_D(N,\tau_o) \propto \beta_N$ with a reference signal $S_D(\text{ref.}) \propto \beta_{Ai}e^{-[N\tau + (N-1)\tau_0]/T_{1A}}$ obtained by omitting the pulses of H_1. Defining $\xi(N,\tau_o) = [S_D(N,\tau_o)/S_D(\text{ref.})]^{1/N}$, Equation (47) immediately gives

$\xi(N,\tau_o) = (1 + \varepsilon f(\tau_o))^{1-N^{-1}}(1+\varepsilon)^{-1}$. Making the reasonable assumption that $f(\infty) = 0$ we use the experiment itself to calibrate ε with $\xi(N,\infty) = (1+\varepsilon)^{-1}$. Expansion of $\xi(N,\tau_o)$ in powers of ε then gives

$$\frac{\xi(N,\tau_o)}{\xi(N,\infty)} - 1 = (1-N^{-1})\varepsilon f(\tau_o)[1 + O(10^{-3})], \qquad (48)$$

so that experimental data for $f(\tau_o)$ is obtained from the left-hand side of Equation (48).

Free induction decay data for ^{43}Ca in CaF_2 with $\underline{H}_o||[110]$ is shown in Figure 18 with the experimental parameters given in the figure caption. The solid line shown is a calculated curve of $f(\tau_o)$ using the Anderson-Weiss (A-W) model theory. The results of this theory may be taken over to the present situation with the following correspondence of notation: $\omega_p^2 \rightarrow \langle\Delta\omega^2\rangle_{AB}$; $\phi_{\Delta\omega}(\tau) \rightarrow a(\tau)$; $\phi(\tau) \rightarrow f(\tau)$, with the A-W notation on the left. The A-W expression for the free induction decay envelope is then

$$f(\tau_o) = \exp\left\{-\langle\Delta\omega^2\rangle_{AB}\int_0^{\tau_o} d\tau(\tau_o-\tau)a(\tau)\right\}. \qquad (49)$$

This decay function has zero slope at $\tau_o = 0$, and asymptotically approaches an exponential function

$$f(\tau_o) \propto \exp\left[-\langle\Delta\omega^2\rangle_{AB}\tau_o \int_0^\infty a(\tau)d\tau\right] \text{ as } \tau_o \to \infty .$$

Although the data of Figure 18 are uncorrected for quadrupolar broadening, we compare it with a calculated curve (solid line) using Equation (49) and $a(\tau)$ given by Equation (15) where τ_c is chosen (arbitrarily) to fit the exponential region of the data. The τ_c value so determined is within a few percent of the theoretical value. The initial curvature of the free induction data is clearly discernible and is well represented by the A-W model theory.

To make an accurate comparison of theory and experiment, we develop a procedure to correct measured T_{2B} values for the quadrupolar broadening effects revealed in the $\theta = \pi/2$ audio-linewidth studies of Section V. For this we use the relation between T_2 and the second and fourth moments M_2 and M_4 given by the A-W model theory, namely $T_2^{-1} = M_2/\omega_e$, where

$$\omega_e^{-1} = \int_0^\infty a(\tau)d\tau \text{ and } M_4 = 3M_2^2 - M_2 \left.\frac{d^2a(\tau)}{d\tau^2}\right|_{\tau=0} .$$

Using Equation (15) for $a(\tau)$ these relations combine to give

$$T_{2B}^2 = \frac{2}{\pi^2} \frac{\left(M_4 - 3M_2^2\right)}{M_2^3} \tag{50}$$

Equation (50) is valid within the framework of the A-W model for a purely exponential spectrum of dipolar fluctuations. We assume it to hold when small quadrupolar corrections to M_2 and M_4 are introduced. With a secular line-broadening Hamiltonian consisting of the terms $\mathcal{H}_d^{AB} + \mathcal{H}_d^{AA} + \mathcal{H}_Q^B$ from Sections II and V, the method of moments gives

$$M_2 = M_2^D + M_2^Q, \quad \left(M_2^D \equiv \langle \Delta\omega^2 \rangle_{AB}\right) \tag{51a}$$

$$M_4 = M_4^D + M_4^Q + 6M_2^Q M_2^D, \tag{51b}$$

where M_2^Q and M_4^Q are given in detail in Appendix B. Substituting Equations (51) into Equation (50) then yields

$$T_{2B}^2 = \frac{\left(T_{2B}^D\right)^2 + 2\left[M_4^Q - 3\left(M_2^Q\right)^2\right]\left[\pi^2\left(M_2^D\right)^3\right]^{-1}}{\left(1 + M_2^Q/M_2^D\right)^3} \tag{52}$$

where T_{2B}^D is the relaxation time from dipolar coupling only. The second term in the numerator is found on close examination to be negligibly small compared with $(T_{2B}^D)^2$. We therefore extract T_{2B}^D from the experimental data with the formula

$$T_{2B}^{D} = T_{2B}(\text{measured})\left[1 + M_2^Q/M_2^D\right]^{3/2} \qquad (53)$$

From the value $M_2^Q(\theta = \pi/2) = 8.0\times10^5\ \text{sec}^{-2}$ obtained in Section V we find $M_2^Q(\theta = 0) = 3.2\times10^6$. Calculated values of M_2^D for the exact crystal orientation described in Section III give, using Equation (53), correction factors $(1 + M_2^Q/M_2^D)^{3/2} = 1.13$ and 1.17 for $\underline{H}_o||[111]$ and [110], respectively.

The data and interpretation for the exponential part of $f(\tau_o)$ are summarized in Table III for the two crystal orientations studied. Theoretical values of T_{2B}^D are shown for a purely exponential spectrum (as indicated by the measured $\tau_{AB}^{-1}(\omega_{eB})$ values in Section IV) and for a contrasting Gaussian fluctuation spectrum. The corrected experimental values of T_{2B}^D are seen to lie between those corresponding to these two model spectra, but actually quite close to those for the exponential spectrum. This indicates that the spectra plotted in Figure (8) do not vary exponentially below $\omega_{eB}/2\pi = 2$ kHz, but level off and strike the $\omega_{eB} = 0$ axis below the exponential intercept by the fractional amount shown in the far right-hand column of Table III. We interpret this in turn to mean that $a(\tau)$ varies as Equation (15) out to several τ_c's, then diminishes more rapidly, so that the quantity

$$\int_0^\infty a(\tau)d\tau$$

measured by the T_2 decay is smaller by the factors 0.94([111]) and 0.82([110]) than for a purely Lorentzian $a(\tau)$.

The corrected experimental value of T_{2B}^D for $H_o||[111]$ has been compared with measured rotary saturation linewidths for $\theta = \pi/4$ and $\pi/6$ in Section V. For these angles the quadrupolar linewidth corrections are less than 2 percent, and the close agreement between T_{2B}^D as found here and the experimental audio linewidths lends support to our correction scheme for quadrupole effects based on Equation (53) and Appendix B.

TABLE III

H_o Along	Measured T_{2B}	T_{2B}^D values (μsec): Experiment corrected for quadrupolar broadening	Theory (exponential spectrum)	Theory (Gaussian spectrum)	$\frac{T_{2B}^D(\text{exponential})}{T_{2B}^D(\text{measured})}$
[111]	217 ±18	245	231	408	0.94
[110]	421 ±47	492	404	715	0.82

VIII. MEASUREMENT OF T_{1B}

In the double-resonance experiments of Sections IV-VII, the results do not depend on the ^{43}Ca spin-lattice relaxation time T_{1B} as long as $T_{1B} >> \tau_{AB}$. With a modified version of the pulsed double-resonance technique of Section IV, however, T_{1B} values satisfying this condition can be straightforwardly measured for rare spins of sufficiently large abundance. The T_1 measurement technique is described in this section, and experimental results for ^{43}Ca in CaF_2 are presented and discussed.

In contrast to the ^{19}F nuclei in our specimen, the ^{43}Ca spin-lattice relaxation process appears to be dominated by the intrinsic Raman scattering of phonons by the ^{43}Ca nuclear quadrupole moment, a process first studied rigorously by Van Kranendonk.[30] This conclusion is drawn from the measured temperature-dependence of T_{1B} and from the observation that the paramagnetic impurity relaxation mechanism is inhibited for ^{43}Ca by the weakness of spin-diffusion processes for such a rarefied nuclear species. In quadrupolar relaxation processes both $\Delta m = \pm 1$ and $\Delta m = \pm 2$ transitions are allowed according to the rate formulas

$$W_{m,m+1} = \frac{(2m+1)^2(S-m)(S+m+1)}{2S^2(2S-1)^2} W_1 \qquad (54a)$$

$$W_{m,m+2} = \frac{(S-m-1)(S+m+2)(S-m)(S+m+1)}{2S^2(2S-1)^2} W_2, \qquad (54b)$$

where W_1 and W_2 depend on the nuclear quadrupole moment Q and the properties of the crystal lattice vibrational spectrum.

Unless it happens accidentally that $W_1 = W_2$, the rates in Equations (54) will not automatically preserve a Boltzmann distribution among the m-levels. In the usual case of quadrupolar relaxation of abundant nuclear spins, the dipolar coupling between nuclear spins is usually strong enough to maintain internal thermal equilibrium. In the present rare-spin case, however, this mutual spin-flip equilibrium mechanism is severely inhibited; an estimate of its strength is developed below which indicates that for most of the ^{43}Ca spins in CaF_2 the internal thermalization time is considerably slower than T_{1B}. Consequently, the approach to spin-lattice equilibrium will in general consist of the sum of several different exponential decay terms. In practice we find only a single rate to be present. This is primarily because our relatively poor signal-to-noise ratio permitted observation of the T_{1B} process only through a single e^{-1} decay time. (It is quite possible that under better conditions, close examination of the decay process for several T_{1B}'s could reveal multiple exponential behavior.) Because the ^{43}Ca are, by preparation, initially in a Boltzmann distribution, there is reason to believe that the rates measured correspond to that condition.

The scheme for measuring T_{1B} consists of three steps, illustrated in Figure 19. These are (1) cooling the B-spins by contact with the cooled A-spin reservoir; (2) allowing the B-spins to relax for a variable time interval t_R; and (3) bringing the cooled B-spins back into contact with the saturated ($T_A = \infty$) A-spin reservoir and measuring the resulting A-spin cooling by means of the A-spin signal amplitude S_D. As the time t_R is increased from zero, the B-spin magnetization at the end of step 2 relaxes toward its spin-lattice equilibrium value, a process which is accompanied by an identical variation of the signal S_D measured in step 3. In order to generate appreciable A-spin cooling in step 3 it is necessary to make the B-spin heat capacity roughly comparable to that of the A-spins. This is accomplished by using very large effective fields $H_e (\varepsilon \propto H_e^2)$.

In step (1) $\underline{H}_e$ is applied at angle θ with respect to $\underline{H}_o$ for a time of several τ_{AB}'s giving an initial B-spin magnetization $M_{BZi} = C_B H_e \beta_{Ai}/(1+\varepsilon)$, where C_B is the B-spin Curie constant, and β_{Ai} is the inverse A-spin temperature following ADRF cooling. It is assumed that $\tau_{AB} << T_{1A}$, a requirement which is in competition with the requirement of large H_e. As H_1 is switched off abruptly, the component $M_{Bzi} = M_{BZi} \cos\theta$ of magnetization along $\underline{H}_o$ is preserved by energy conservation. As t_R is increased M_{Bz} relaxes toward its equilibrium value

$M_{Bzo} = C_B H_o/T_L$. The initial value of M_{Bz} is easily shown to be $M_{Bzi} \cong M_{Bzo} H_e \cos\theta/H_{LA}(1+\varepsilon)$. In the present experiments on CaF_2 we have $H_e \cong 52$ G., $H_{LA} = 0.855$ G., $\theta = \pi/4$, and $\varepsilon = 0.25$, giving $M_{Bzi} \cong 35\ M_{Bzo}$. For $t_R \leq T_{1B}$, then, we may assume M_{Bz} is relaxing effectively toward zero. Assuming the relaxation to be exponential, we have at the end of step (2) $M_{Bz}(t_R) = M_{Bzi} e^{-t_R/T_{1B}}$.

In step (3), M_{Bz} is projected back into the rotating frame on reapplication of H_1, giving $M_{BZ}(t_R) = M_{Bz}(t_R)\cos\theta$. When rotating frame thermal equilibrium is reestablished (having carefully saturated the A-spins so that $\beta_A(t_R) = 0$), the resulting A-spin dipolar signal is then given by

$$S_D = S_{Do} \frac{\varepsilon \cos^2\theta}{(1+\varepsilon)^2} e^{-t_R/T_{1B}}, \qquad (55)$$

where S_{Do} is the signal amplitude which would be found immediately following ADRF in step (1). As mentioned above it is advantageous to use large enough values of H_e to make $\varepsilon \sim 1$, thus maximizing S_D. This is easily accomplished for a given value of H_1 by adjusting $\Delta H = \omega/\gamma - H_o$. The practical limit of this procedure occurs when $\tau_{AB} = \tau_{AB(0)} e^{\gamma_B H_e \tau_c}/\sin^2\theta$ becomes comparable to T_{1A}. At this point one begins to lose magnetization in the thermal equilibrium processes of steps (1) and (3), and S_D drops sharply from the value given in Equation (55). With

the experimental parameters given above we have $S_D \cong 0.08\ S_{Do}$, and $\tau_{AB} \cong 0.7$ sec ($T_{1A} = 4.1$ sec), with $\underline{H}_o || [111]$.

A typical set of T_{1B} relaxation data taken as described above is shown in Figure 20, giving $T_{1B} = 202 \pm 19$ sec under the conditions shown. The relaxation interval t_R was varied in increments of 30 sec and was timed with a watch. Because the maximum signal-to-noise ratio was only 3 or 4, five measurements were averaged to obtain each data point in Figure 20. The straight line fit to the decay curve was then determined by computer using the least-squares method.

T_{1B} measurements have been performed at 300°K and at 355°K, using the heating arrangement described in Section III, and at a variety of orientations of crystal axes relative to $\underline{H}_o$. Parts (1) and (3) of the measurement process of Figure 19 were always carried out with $\underline{H}_o || [111]$ in order to have the best signal-to-noise ratio. For relaxation measurements at other orientations, the crystal was simply rotated by hand to the desired orientation at the beginning of the relaxation period and returned to the [111] direction at the end. These operations could be accomplished in less than a second, and thus make a negligible contribution to the scatter of the data. T_{1B} values were obtained under each set of conditions as described above. The results of all the T_{1B} measurements are plotted in Figure 21 on angular scales showing the three main symmetry axes. No anisotropy in T_{1B} which exceeds the

experimental scatter is seen at either temperature. There is, however, a significant change in the average T_{1B} (dashed line) between the two temperature values used.

We compare the temperature dependence of T_{1B} with the ionic model calculation of Van Kranendonk,[30] which gives

$$\frac{1}{T_1} \propto (T^*)^2 E(T^*), \tag{56}$$

where $T^* \equiv T/\theta_D$, θ_D is the Debye temperature, and $E(T^*)$ is a numerical function[30] which approaches unity for $T^* >> 1$. Using $\theta_D = 510°K$ for CaF_2 we find from Equation (56)

$$\left[\frac{T_1(355°K)}{T_1(300°K)}\right]_{theory} = 0.685, \tag{57}$$

in reasonable agreement with the experimental ratio

$$\left[\frac{T_1(355°K)_{exp}}{T_1(300°K)_{exp}}\right] = 0.72 \pm 0.13. \tag{58}$$

We note that, in addition to the acoustic phonon contribution to $1/T_{1B}$ calculated by Van Kranendonk, there exist potential contributions from optical phonons as discussed by Wikner, et. al.[31] and from the covalent admixture mechanism of Yosida

and Moriya.[32] No attempt has been made to estimate the relative rate contributions from these various mechanisms. However, since they all have similar (though not identical) temperature dependences, the comparison with Equation (56) is not an inappropriate one. For example, in a study of quadrupolar relaxation in rather highly covalent III-V compounds, Mieher[33] found good agreement with the temperature dependence given by Van Kranendonk's ionic model.

The observed isotropy of the ^{43}Ca spin-lattice relaxation in Figure 21 is not surprising, since no cubic system has been found to have an anisotropic quadrupolar spin-lattice relaxation rate. This has been found to be true experimentally in spite of calculated anisotropies in the coefficients W_1 and W_2 of Equations (54). Mieher[33] has noted that these anisotropies cancel out for a number of crystal structures with both the Van Kranendonk and Yosida-Moriya models <u>when W_1 and W_2 are combined to give the Boltzmann-distribution T_1 value</u>. As noted above it is just this thermal equilibrium rate which is apparently measured in this work, in spite of the absence of an effective thermalizing mechanism.

Finally, we examine the influence on the T_1 of ^{43}Ca of the paramagnetic ions which relax the ^{19}F nuclei. These are thought to be at least two orders of magnitude more dilute than the ^{43}Ca. On this basis the contribution of these ions to $1/T_{1B}$ would fall in the spin-diffusion limited regime discussed

by Khutsishvili[34] and others[35,36] for which the T_1 process is an exponential one with

$$1/T_1 = 8.5\ N_P C^{1/4} D^{3/4}. \qquad (59)$$

Here N_P is the concentration of paramagnetic ions in the crystal, D is the nuclear spin diffusion constant, and $C = (2/5)(\gamma_B \gamma_e \hbar)^2 \cdot S_P(S_P+1)\tau_e(1+\omega_{oB}^2\tau_e^2)^{-1}$ is the coefficient of r^{-6} in the (isotropic average) relaxation rate $1/T_1'$ of a B-spin interacting with a paramagnetic ion of moment $\gamma_e \hbar S_P$ and spin-lattice relaxation time τ_e at a distance r.

It is difficult to make a meaningful estimate of the spin-diffusion constant D for a system of rare nuclei, because the rate $1/\tau_{eq}$ at which a given nucleus approaches thermal equilibrium with its surrounding like nuclei is strongly dependent upon the exact spatial distribution of such neighbors. For a system as dilute as ^{43}Ca, one finds a distribution of τ_{eq} values ranging over several orders of magnitude. We deal with this problem in an approximate way by calculating an "average" value of τ_{eq} (of a sort to be discussed presently) and taking over Bloembergen's estimate[22] $D \cong b^2/50\ T_2$ to the present case with the correspondence $T_2 \rightarrow \tau_{eq}$ and $b \rightarrow (N_B)^{-1/3}$, where b represents the distance between neighboring nuclei. Thus $D_B \sim N_B^{-2/3}/50\ \tau_{eq}$.

A calculation of τ_{eq} for a given configuration of like-spin neighbors is carried out in Appendix A, based on the following model. An ensemble of identical systems is envisioned in which the nucleus S_o at the origin of coordinates has a nonzero average magnetization M_{zo} and all other (like) nuclei in the system have zero magnetization. We define $1/\tau_{eq}$ as the fractional rate of decay of M_{zo} at t = 0 due to mutual spin flips with its neighbors, i.e., the process whereby spin energy diffuses away from S_o to the bulk. Thus $1/\tau_{eq} = \left(M_{zo}^{-1}\ d/dt\ (M_{zo})\right)_{t=0}$ The dipolar coupling terms $C_{oi}S_{o\pm}S_{i\mp}$ with each neighbor i are entirely responsible for $d/dt\ (M_{zo})$, since these are the <u>only</u> high field secular coupling terms which do not commute with S_{oz}. In CaF_2 these ^{43}Ca-^{43}Ca terms are weak and are rapidly modulated by the ^{43}Ca-^{19}F dipolar interaction, which in turn is even more rapidly modulated by the ^{19}F-^{19}F dipolar coupling. We may therefore treat the $S_{o\pm}S_{i\mp}$ terms as perturbations, using the extreme narrowing approximation as incorporated into the master equation for the time rate of change of the density matrix. The result from Appendix A is

$$\frac{1}{\tau_{eq}} = \frac{4S(S+1)T_{2B}}{3} \sum_{i(occ)} C_{oi}^2 \qquad (60)$$

where the sum on i ranges over occupied neighbor sites, with $C_{oi} = -\gamma_B^2\hbar(1 - 3\cos^2\theta_{oi})/(4r_{oi}^3)$.

One must exercise caution in defining a suitable average of $1/\tau_{eq}$ to use for an estimate of D. For example, the familiar procedure of summing over all sites and multiplying by the isotopic fraction is inapplicable here, because such a sum is dominated by the first-neighbor contribution and does not represent the bulk behavior but rather that of "pairs" of only rare occurrence. Instead we proceed by observing that about 90 percent of the ^{43}Ca have no like neighbors in the first six neighbor shells. This is deduced from the probability $(1-f)^N$ that a given N sites of the crystal are unoccupied with a species of abundance f. For these 90 percent, which we take as representing the bulk behavior, we define

$$\langle 1/\tau_{eq}\rangle_{av} = \frac{4S(S+1)T_{2B}}{3} f \sum_{n=7}^{\infty} N_n \langle C_{on}^2\rangle_{av\ \theta} \qquad (61)$$

where $\langle C_{on}^2\rangle_{av\ \theta}$ is the isotropic average and N_n is the number of atoms in the nth neighbor shell. Upon evaluation of Equation (61) and substitution of CaF_2 parameter values we find $\langle 1/\tau_{eq}\rangle_{av} = 3.4\times10^{-4}\ sec^{-1}$.

This estimate is at best good to within an order of magnitude. With this reservation in mind we compare the paramagnetic ion contribution to T_{1B} with T_{1A} using Equation (59) and taking $D_A = a^2/50\ T_{2a}$, a = ^{19}F - ^{19}F distance, and $D_B = N_B^{-2/3}\langle 1/\tau_{eq}\rangle_{av}/50$, with $\langle 1/\tau_{eq}\rangle_{av}$ from Equation (61):

$$\frac{T_{1B}}{T_{1A}} = \left(\frac{\gamma_A}{\gamma_B}\right)^{1/2} \left[\frac{\left(1 + \tau_e^2\omega_{oB}^2\right)^{1/4}}{\left(1 + \tau_e^2\omega_{oA}^2\right)^{1/4}}\right] \frac{a^{3/2}N_B^{1/2}}{(T_{2A}\langle 1/\tau_{eq}\rangle)^{3/4}} \quad . \qquad (62)$$

The quantity in brackets is at least unity, so that with T_{2A} = 50 μsec and T_{1A}(Zeeman) ≅ 10 sec we find $T_{1B} \cong 2\times10^5$ sec as compared with measured values $T_{1B} \sim 2\times10^2$ sec. This estimate effectively rules out paramagnetic impurities as a source of ^{43}Ca spin-lattice relaxation, even with an order-of-magnitude error in our guess at D_B. We also note that $T_{1B}\langle 1/\tau_{eq}\rangle \ll 1$, so that the B-spins are on the whole decoupled from one another during a period of one spin-lattice relaxation time.

IX. CONCLUSIONS AND DISCUSSION

In concluding our presentation we emphasize three major points of our work:

(1) The thermodynamic model of nuclear double resonance dynamics developed a few years ago[1] and applied and tested here on the system CaF_2:^{43}Ca has proved highly successful in giving a quantitative description of our experimental results. Thus the spin-temperature description of nuclear spin energy reservoirs tested in a variety of ways by previous workers[1,5,7,15,19] has been extended to include behavior during dynamical energy transfer processes between dissimilar nuclei. Such processes have been shown here to exhibit simple exponential rate character for the system studied under the approximations of negligible spin-diffusion effects and rapid modulation of the dipolar coupling between rare and abundant nuclear spins. This simple rate behavior will presumably hold for any system under those experimental conditions where the A-B nuclear coupling is weak, i.e., for $\tau_{AB} \gg T_{2A}$, even if the condition $\langle \Delta\omega^2 \rangle_{AB} T_{2A}^2 \ll 1$ is violated. A system might be envisioned, for example, with a rare species having a considerably greater nuclear moment than the abundant species, giving $\langle \Delta\omega^2 \rangle_{AB} T_{2A}^2 > 1$. In such a case the simple rate character found here for all values of ω_{eB} will only occur in the tail of the fluctuation spectrum for which $\omega_{eB} T_{2A} \gg 1$. At lower frequencies ω_{eB} the oscillatory behavior studied in Section VI will merge with the τ_{AB} process, as has begun to happen in the data of Fig. 17a, and precise

calculations of the total energy transfer process will become enormously more complex. This picture will be further complicated by spin-diffusion limiting, which will become severe in a case where $\tau_{AB} < T_{2A}$.

(2) The present results give a precise calibration of the sensitivity of rotating frame nuclear double resonance for the system studied. Using the experimentally determined maximum double-resonance rate $(\varepsilon/\tau_{AB})_{max} = 10\ sec^{-1}$ and assuming conservatively that a 10% change in the ^{19}F signal level can be resolved, one arrives at a minimum detectable concentration of ^{43}Ca spins of $N_B/N_A = 1.6 \times 10^{-6}$ or about 8×10^{16} nuclei/c.c. One might anticipate an order-of magnitude improvement on this figure from working at lower temperatures and/or higher frequencies to improve the A-spin signal-to-noise ratio and another order of magnitude from using a crystal with a weaker spin-lattice relaxation process in order to increase the A-B system interaction time. These considerations have been discussed in Ref. 1.

The present results for sensitivity can be easily extrapolated to other spin-systems by appropriate changes in the parameters appearing in the fundamental double-resonance time-constant ε/τ_{AB}. However, a word of caution is in order regarding this procedure. As noted above, significant increases in the ratio T_{2A}/τ_{AB} will almost surely result in appreciable spin-diffusion inhibition of A-B system energy transfer. Spin-diffusion will then become a primary consideration for sensitivity.

Perhaps the most important result offered by the present work with regard to the detection of rare nuclei is the π-pulse double-resonance technique outlined in Section VI. This method is comparable in sensitivity to the RSDR scheme, but is far less dependent upon precise control of experimental parameters (i.e., H_1 and ω_a for RSDR) and is in general much easier to instrument in the case of a wide-ranging search for weak NMR or NQR lines.

(3) Our experimental determination of the fluctuation spectrum of the ^{19}F- ^{43}Ca dipolar coupling operator in CaF_2 is a result of considerable physical interest. The surprising outcome of exponential behavior displayed by these spectra in Figs. 8 and 9 was not anticipated here, nor was it elsewhere to the best of our knowledge. The exponential spectral form and associated Lorentzian autocorrelation function $a(\tau)$ were essential in calculating the double resonance interaction time-constant τ_{AB} in Section II, the oscillatory spin-temperature behavior with pulsed H_1 fields in Section VI, and the B-spin transverse relaxation time T_{2B} in Section VII, with satisfactory results in all cases.

As to the general validity of exponential spectral shape for operators of the form of the factor $\sum_i B_i I_{zi}$ occurring in the Hamiltonian term $\mathcal{H}_p$ (Eq.(4)), very little can be said on a rigorous basis without extensive further study. The clear-cut nature of this result is suggestive of a simple

under-lying physical mechanism, though none is advanced here. Apropos of these results, however, we make the following remarks. First, it is clear that the exponential form we find is not just an accidental quirk associated with a particular set of ^{19}F-^{19}F dipolar coupling coefficients, since this result holds with H_o along both the [110] and [111] crystalline axes of CaF_2, representing two rather widely different forms for $\mathcal{H}_d^{AA}$ (Eq.(1)). With $\underline{H_o}$ || [111] for example, all first-neighbor terms in $\mathcal{H}_d^{AA}$ vanish, whereas no first-neighbor terms vanish for $\underline{H_o}$ || [110]. We regret to say that the spectral form of $\mathcal{H}_p$ could not be checked with $\underline{H_o}$ || [100] owing to the extreme shortness of T_{2A}.

Secondly, although it is not clear that the present results can be extrapolated to paramagnetic systems with spin-spin interactions of nondipolar charcter (e.g., isotropic exchange), we find an interesting correspondence with the exchange-narrowed linewidth results given recently by Gulley et al[17]. These authors noted a systematic discrepancy between measured NMR and ESR linewidths [$(\Delta H)_M$] and theoretical values calculated with the cut-off Lorentzian model [$(\Delta H)_{CL}$] using known values of the second and fourth moments of the resonance lines studied. The observed discrepancies $(\Delta H)_M/(\Delta H)_{CL}$ ranged mainly from 2.1 to 2.8 with one value at 1.48. We note that the assumption of an exponential fluctuation spectrum in these systems (MnF_2, $KMnF_3$ and $RbMnF_3$) leads, on the Anderson-

Weiss model theory[13], to a calculated linewidth $(\Delta H)_{EXP}$ larger than the cut-off Lorentzian value by a ratio $(\Delta H)_{EXP}/(\Delta H)_{CL} = 2.4$ and is in reasonable agreement with the measured values. One can neither confirm nor deny on this basis that the coupling operators in these materials have exponential fluctuation spectra, but it does suggest the latter form as a good starting point in the estimate of exchange-narrowed linewidths in these and other paramagnetic systems.

Acknowledgments

The authors wish to thank Dr. L. R. Walker of Bell Telephone Laboratories for suggesting the functional form for the model lineshape function of Appendix B. One of the authors (D.A.M.) gratefully acknowledges the support of a National Science Foundation Graduate Fellowship during part of this work. This work was performed under the auspices of the United States Atomic Energy Commission.

APPENDIX A

THERMAL EQUILIBRATION AMONG RARE SPINS

We calculate the rate $(1/\tau_{eq})$ at which a given B-spin comes into thermal equilibrium with neighboring like nuclei using the following model. Consider an ensemble of identical systems in which the spin $\underline{S}_o$ situated at the origin possesses at $t = 0$ a nonequilibrium average magnetization $\langle S_{zo}\rangle$; the other like nuclei $\underline{S}_i$ are assumed to be distributed at random (with average concentration c) throughout the crystal lattice and to be initially at the thermal equilibrium $\langle S_{zi}\rangle_{t=0} = \langle S_{zi}\rangle_0$, $i \neq 0$. Each spin is further assumed to be in a Boltzmann distribution of Zeeman states over the ensemble. No rf fields are assumed to be present.

To simplify our manipulations we represent the dipolar field $\sum_i B_{ji} I_{zi}$ at the jth B-spin site due to the surrounding A-spins (see Equation (1)) as a randomly varying magnetic field $h_j(t)$. The h_j's will be assumed to have the rms value and autocorrelation function of the corresponding quantum-mechanical operator. With this semiclassical model the equation of motion for the density matrix σ of the B-spin system becomes

$$i\dot{\sigma} = \left[\mathcal{H}_{BB} - \gamma_B \sum_j h_j(t) S_{z_j}, \sigma\right], \qquad (A.1)$$

Appendix A - 2

where

$$H_{BB} = \sum_{i>j} C_{ij}(S_{+i}S_{-j}+S_{-i}S_{+j})$$

is the intra-B-spin coupling which acts to perturb the value of a given $\langle S_{z\,j}\rangle$. In order to apply the master equation[10] for the rate of change of σ we transform Equation (A.1) to an interaction representation defined as follows:

$$\sigma^* = B\sigma B^+ \tag{A.2}$$

with

$$B = \exp\left[-i\gamma_B \sum_j \int_0^t h_j(t')dt'\ S_{z\,j}\right].$$

Equation (A.1) is then transformed to

$$i\dot{\sigma}^* = \left[H^*_{BB}(t),\sigma^*\right], \tag{A.3}$$

where $H^*_{BB}(t)$ is the transform of H_{BB} given by Equation (A.2). We now apply the master equation to Equation (A.3), regarding $H^*_{BB}(t)$ as a rapidly modulated random variable, yielding

$$\dot{\sigma}^* = -\int_0^\infty \overline{\left[H^*_{BB}(t),\left[H^*_{BB}(t-\tau),(\sigma^*-\sigma_o)\right]\right]}d\tau. \tag{A.4}$$

Appendix A - 3

In Equation (A.4) the bar, which conventionally[10] means a trace over the thermal equilibrium distribution of lattice (or A-spin) states, is taken here as an ensemble average over the instantaneous distribution of h_j's.

We may use Equation (A.4) to obtain a formal expression for the fractional rate of decay of $[\langle S_{zo}\rangle_{t=0} - \langle S_{zo}\rangle_0]$, which we define to be $1/\tau_{eq}$, i.e., the result we are seeking. In the high-temperature approximation we write $\sigma = \sum_i c_i S_{zi}$ and $\sigma_o = \sum_i c_i(eq) S_{zi}$. It immediately follows from Equation (A.2) that $\sigma^* = \sigma$, and all terms of $\sigma^* - \sigma_o$ in Equation (A.4) vanish (initially) except for $(c_o - c_o(eq))S_{zo}$. Thus

$$\frac{1}{\tau_{eq}} = \left.\frac{\frac{d}{dt}\left[\langle S_{zo}\rangle - \langle S_{zo}\rangle_0\right]}{\left[\langle S_{zo}\rangle - \langle S_{zo}\rangle_0\right]}\right|_{t=0} = \frac{\left.\mathrm{Tr}(S_{zo}\dot{\sigma}^*)\right|_{t=0}}{\left(c_o - c_o(eq)\right)\mathrm{Tr}\left(S_{zo}^2\right)}$$

$$= -\frac{\overline{\int_0^\infty \mathrm{Tr}\left\{S_{zo}\left[H_{BB}^*(0), \left[H_{BB}^*(-\tau), S_{zo}\right]\right]\right\} d\tau}}{\mathrm{Tr}\left(S_{zo}^2\right)} . \qquad (A.5)$$

Carrying out the indicated commutator and trace operations, Equation (A.5) becomes

Appendix A - 4

$$\frac{1}{\tau_{eq}} = \frac{4}{3} S(S+1) \sum_j C_{oj}^2$$

$$\cdot \int_0^\infty d\tau \left\langle \exp\left[-i \int_0^\tau \gamma_B \left[h_o(t') - h_j(t')\right] dt' + C.C.\right\rangle_{av} \quad (A.6)$$

where the ensemble average is now indicated by the brackets $\langle\ \rangle_{av}$. We assume all the h_j's to be independent and to have the same mean square value $\langle h^2 \rangle$ and autocorrelation function $\langle h_j(\tau) h_j(0) \rangle_{av} = \langle h^2 \rangle a(\tau)$, where $a(0) = 1$. Then the fundamental procedure of the Anderson-Weiss calculation[13] may be used to evaluate the averages $\langle\ \rangle_{av}$ in Equation (A.6). The principal assumption is that the instantaneous distribution of h_j's is Gaussian; therefore the exponentials in Equation (A.6) also have Gaussian distributions. The averaging process is then carried out straightforwardly[13] to give

$$\frac{1}{\tau_{eq}} = \frac{8}{3} S(S+1) \sum_j C_{oj}^2 \int_0^\infty d\tau \left[\exp\left[-2\gamma_B^2 \int_0^\tau (\tau-\tau') a(\tau') d\tau\right]\right]$$

(A.7)

Appendix A - 5

With the assumption of a short correlation time, expressed here as $\gamma_B^2\langle h^2\rangle\tau_c^2 << 1$, the exponential function becomes $e^{-\pi\gamma_B^2\langle h^2\rangle\tau_c\tau}$ for $\tau >> \tau_c$, using the function $a(\tau)$ given by Equation (15). Finally, we identify $\pi/2\ \gamma_B^2\langle h^2\rangle\tau_c \cong 1/T_{2B}$ (see Equation (17) with $\theta = \pi/2$, $\omega_{eB} = 0$). Carrying out the integral in Equation (A.7) we find

$$\frac{1}{\tau_{eq}} = \frac{4S(S+1)}{3} T_{2B} \sum_j C_{oj}^2 \qquad (A.8)$$

as given in Section VIII. The sum over j is carried out over occupied neighbor sites only and will vary for rare nuclei over many orders of magnitude, depending on the configuration of like neighbors in the vicinity of a given B-spin.

APPENDIX B

We develop a lineshape model based on the function $f(t) = \exp[c(a - (a^2+t^2)^{1/2})]$ to represent the free-precession envelope, where the Fourier transform $g(\omega) = FT(f(t))$ gives the shape of the resonance line. The constants c and a are to be related to the moments M_2 and M_4 of $g(\omega)$, which are well-known[37] to be proportional to the second and fourth derivatives of f(t) at t = 0. The favorable properties of this model function are that all of its derivatives are finite at t = 0, all odd derivatives at t = 0 (and therefore odd moments) vanish, and $g(\omega)$ can be made very nearly Lorentzian or Gaussian in shape, depending on the values of c and a, with a continuous range of intermediate possibilities. The Fourier transform of f(t) is a tabulated Bessel function:

$$g(\omega) = \frac{(ac)e^{ac}K_1[a(\omega^2+c^2)^{1/2}]}{\pi(\omega^2+c^2)^{1/2}} \qquad \text{(B.1)}$$

By straightforward differentiation of f(t) we find for the first three even moments of $g(\omega)$:

$$M_2 = c/a$$

$$M_4 = 3\left(\frac{c}{a^3} + \frac{c^2}{a^2}\right) \qquad \text{(B.2)}$$

$$M_6 = 45\left(\frac{c}{a^5} + \frac{c^2}{a^4} + \frac{c^3}{3a^3}\right)$$

Appendix B - 2

It is convenient to express the moments in terms of ξ, the ratio of fourth to second moment squared ($M_4 = \xi M_2^2$), and the second moment itself. The ratio η of sixth to second moment cubed then becomes

$$\eta = \frac{M_6}{M_2^3} = 5[\xi^2-3\xi+3]. \tag{B.3}$$

We also have

$$a = \sqrt{3}\ [M_2(\xi-3)]^{-1/2}$$

and

$$c = \frac{\sqrt{3}\ M_2^{1/2}}{(\xi-3)^{1/2}}\ .$$

Introducing $\lambda = \sqrt{3}\ (\xi-3)^{-1/2}$, Equation (B.1) becomes

$$g(\omega) = \frac{\lambda^2 e^{\lambda^2} K_1\left[\lambda M_2^{-1/2}(\omega^2+\lambda^2 M_2)^{1/2}\right]}{\pi(\omega^2+\lambda^2 M_2)^{1/2}}\ . \tag{B.4}$$

The Lorentzian and Gaussian limits correspond to ($\xi \to \infty$, $\lambda \to 0$) and ($\xi \to 3$, $\lambda \to \infty$), respectively.

The above model is now applied to purely quadrupolar broadening of a resonance line, as is found for $\theta = \pi/2$ in the audio resonance studies of Section V. With a quadrupolar

Appendix B - 3

broadening operator $H^{Q}_{BR} = AS_Z^2(3\cos^2\theta-1)/2$, the method of moments gives for S = 7/2

$$M_2 = 3\langle A^2\rangle_{av}(3\cos^2\theta-1)^2$$

$$M_4 = 16.3\langle A^4\rangle_{av}(3\cos^2\theta-1)^4 \qquad \text{(B.5)}$$

$$M_6 = 1.41\times10^2\langle A^6\rangle_{av}(3\cos^2\theta-1)^6$$

where the averages are taken over all B-spin sites in the crystal. For want of more detailed knowlege of these averages, we assume in the present work a Gaussian distribution of $|A|$ values, giving $\langle A^4\rangle_{av} = 3\langle A^2\rangle_{av}$ and $\langle A^6\rangle_{av} = 15\langle A^2\rangle^3_{av}$. Thus we find from (B.5), $\xi = 5.42$ and $\eta = 78.0$. With the line-shape model Equation (B.3) gives $\eta = 80$ for $\xi = 5.42$ and is therefore an excellent representation of the calculated moments in this case. By contrast a cut-off Lorentzian model gives (with $\xi = 5.42$) an η-value more than an order of magnitude smaller.

With $\xi = 5.42$ we find $\lambda = 1.11$. The corresponding lineshape is plotted in Figure (B.1) in units of $\omega/(\lambda M_2^{1/2})$. For comparison a Lorentzian curve of equal half-width and amplitude at line center is also plotted (dashed curve). The model lineshape function is seen to be very nearly of Lorentzian shape near the center. The half-width at half-maximum is given by $\Delta\omega_{half} = 0.84\ M_2^{1/2}$, yielding $M_2 = 1.40\ (\Delta\omega_{half})^2$.

REFERENCES

1. S. R. Hartmann and E. L. Hahn, Phys. Rev. 128, 2042 (1962).
2. R. E. Walstedt, D. A. McArthur and E. L. Hahn, Physics Letters 15, 7 (1965); R. E. Slusher and E. L. Hahn, Phys. Rev. 166, 332 (1968).
3. C. P. Slichter and W. C. Holton, Phys. Rev. 122, 1701 (1961).
4. J. Phillippot, Phys. Rev. 133, A471 (1964).
5. A. G. Redfield, Phys. Rev. 98, 1787 (1955).
6. F. M. Lurie and C. P. Slichter, Phys. Rev. 133, A1108 (1964).
7. S. R. Hartmann and A. G. Anderson, Magnetic Resonance and Relaxation, edited by J. Smidt, Interscience Publishers, Inc., New York (1963); S. R. Hartmann, Phys. Rev. 133, A17 (1964); R. E. Walstedt, Phys. Rev. 138, A1096 (1965).
8. R. K. Wangsness and F. Bloch, Phys. Rev. 89, 728 (1953).
9. A. G. Redfield, IBM Journal 1, 19 (1957).
10. A. Abragam, The Principles of Nuclear Magnetism, (Oxford University Press, London, 1961) Chap. VIII.
11. A. G. Anderson, Phys. Rev. 115, 863 (1959).
12. L. J. F. Broer, Physica 10, 801 (1943).
13. P. W. Anderson and P. R. Weiss, Revs. Mod. Phys. 25, 269 (1953).
14. N. Bloembergen, E. M. Purcell and R. V. Pound, Phys. Rev. 73, 679 (1948).
15. J. R. Franz and C. P. Slichter, Phys. Rev. 148, 287 (1966).
16. R. L. Strombotne and E. L. Hahn, Phys. Rev. 133, A1616 (1964).
17. J. E. Gulley, B. G. Silbernagel and V. Jaccarino, Proc. of the Fourteenth Annual Conference on Magnetism and Magnetic Materials, New York (1968), J. Appl. Phys., to be published.

18. A small degree of ^{43}Ca quadrupolar broadening is found to be present in Section V, but is inessential for our present purposes.

19. The origin of the factor ω_a/ω_{eB} in Eq.(10) is not as clear in Ref. 14 as, for example, in Ref. 10, Ch. III.

20. J. H. Van Vleck, Phys. Rev. 74, 1168 (1948). The second moment due to like spins on a simple cubic lattice has been calculated by computer to at least 1% accuracy, yielding $M_2 \propto (\alpha^4 + \beta^4 + \gamma^4 - .195)$. This result differs by $\lesssim$ 5% from the result of Van Vleck ($M_2 \propto (\alpha^4+\beta^4+\gamma^4-.187)$).

21. I. J. Lowe and S. Gade, Phys. Rev. 156, 817 (1967). D. Tze and I. J. Lowe, Phys. Rev. 166, 292 (1968).

22. N. Bloembergen, Physica 15, 386 (1949).

23. J. Jeener and P. Broekaert, Phys. Rev. 157, 232 (1967).

24. An attempt was made for $\theta \neq 90°$ to fit the three parameters ε, τ_{AB} and $p \cong \cos^2\theta$ (corresponding to the B magnetization remaining at the beginning of the next pulse), but the 3 parameter iterations would not converge, perhaps because of the amount of experimental scatter.

25. D. A. McArthur, Thesis, University of California, (1967).

26. J. R. White and A. E. Cameron, Phys. Rev. 74, 991 (1948).

27. C. D. Jefferies, Phys. Rev. 90, 1130 (1953).

28. J. S. Waugh, L. M. Huber and U. Haeberlen, Phys. Rev. Letters 20, 180 (1968).

29. A. Abragam, The Principles of Nuclear Magnetism (Oxford University Press, London, 1961) Chap. XII, Eqs. (126) through (128).

30. J. van Kranendonk, Physica 20, 781 (1954).

31. E. G. Wikner, W. E. Blumberg and E. L. Hahn, Phys. Rev. 118, 631 (1960).

32. K. Yosida and T. Moriya, J. Phys. Soc. Japan 11, 33 (1956).

33. R. L. Mieher, Phys. Rev. 125, 1537 (1962).

34. G. R. Khutsishvili, Proc. Inst. Phys., Academy of Science of Georgia (U.S.S.R.) 4, 3 (1956).

35. P. G. De Gennes, J. Phys. Chem. Solids 7, 345 (1958).

36. W. E. Blumberg, Phys. Rev. 119, 79 (1960).

37. A. Abragam, The Principles of Nuclear Magnetism (Oxford University Press, London, 1961) Chap. IV.

FIGURE CAPTIONS

1. Definition of the B-spin effective field in the rotating frame, H_e, viewed from the xyz frame rotating about H_o at the B rf frequency ω. The Z-axis is the axis of quantization of the zero-order B-spin Hamiltonian. The X-axis lies in the x-z plane.
2. Thermodynamic reservoir model of the rare-spin double resonance process, showing spin temperatures for each reservoir and the associated coupling time constants.
3. Block diagram of the ADRF double resonance apparatus; audio coil and sample not shown; rf gating pulses provided by Tektronix pulse generators.
4. Arrangement of sample, audio Helmholtz coil, A rf Helmholtz coil, and solenoidal B rf transmitter coil. The small section of the B rf coil between the two taps serves as a receiver coil for A-spin signals.
5. A-spin irradiation sequence for preparation and monitoring of the ADRF state.
6. Time sequence of B rf irradiation for pulsed double resonance experiment, used during B-spin irradiation inteval of Fig. 5.
7. Ratios of heat capacities ε measured by pulsed ADRF double resonance in CaF_2. Solid lines are calculated curves of ε vs. f_{1B} (Eq.(12)) using atomic concentration of ^{43}Ca reported in reference 26, including the effect of measured crystalline misorientation on H_{LA}.

8a. Measured A-B system cross-relaxation rates τ_{AB}^{-1} as a function of f_{1B} ($\theta=\pi/2$) with $\underset{\sim}{H}_o \parallel$ [110]. The straight line shown is the calculated curve of τ_{AB}^{-1} vs. f_{1B} using Eq.(17), based only on the assumption of exponential dependence on f_{1B}. Bottom curve shows the maximum fractional rate of A-spin heating which occurs for each f_{1B} value in these experiments.

8b. Same as Fig. 8a except with $\underset{\sim}{H}_o \parallel$ [111].

9. Measured A-B system cross-relaxation rates τ_{AB}^{-1} as a function of f_{eB} for four values of θ, using B-spin saturating pulses between the double-resonance pulses of Fig. 6 with $\underset{\sim}{H}_o \parallel$ [111]. Solid lines shown are least-squares computer fits of exponential frequency dependence (Eq. (17)) to the data plots. The theoretical τ_{AB}^{-1} vs. f_{eB} curve shown in Fig. 8b is drawn in as a dashed line for comparison.

10. Dependence of the spectral area A (Eq. (18)) on θ, measured by pulsed ADRF double resonance, for $\underset{\sim}{H}_o \parallel$ [111]. Area data taken from rate spectra of Figs. 8b and 9. The straight line shown is a best fit to the experimental areas (See Table II) of the expected $A \propto \sin^2\theta$ law.

11. Pulses of H_1 and H_a applied during the B-spin irradiation interval of Fig. 5 in the RSDR experimental method.

12. Double resonance spectra taken with $\gamma_B H_1/2\pi$ = 1.29 kHz, H_a = 0.34G., and $\omega_a/2\pi$ = 2.0 kHz (open circles) and $\omega_a/2\pi$ = 1.3 kHz (closed circles). These parameters remained fixed while the frequency ω at which H_1 was applied was varied.

13. Rotary Saturation double resonance line observed by varying ω_a with parameters ω, H_a and H_1 fixed. The saturation parameter S was obtained from measured double resonance rates via Eq.(29). For these data H_1=8.44G, $\theta = \frac{\pi}{2}$, H_a = .085G and $\underset{\sim}{H}_o \parallel [111]$. The solid curve is a computer-fitted Lorentzian as described in the text.

14. Measurement of τ_{AB}/ε by the RSDR method. Experimental values of τ_{AB} (Eq.(29)) are plotted by means of Eq.(30) for $\underset{\sim}{H}_o \parallel [111]$, $\theta = \pi/4$, and f_{eB}=8kHz.

15. Measured A-B system cross relaxation rates τ_{AB}^{-1} as a function of f_{eB} for $\underset{\sim}{H}_o \parallel [111]$ and for three values of θ, obtained using the RSDR technique. Straight lines shown are least-squares fits to corresponding data of Fig. 9.

16. Rotating frame audio resonance linewidths $(2\pi T_{2a}^{*})^{-1}$ from Eq.(31) as a function of f_{eB} for three values of θ, obtained using RSDR technique. Solid lines shown are expected homogeneous $(\cos^2\theta/T_{2B})$ plus expected lifetime broadening $(\frac{1}{2}\tau_{AB}^{-1})$ contributions. Small quadrupolar corrections are included for $\theta = \pi/4$, $\pi/6$.

17. Plot of measured transient spin-temperature variation $\delta(\tau)$ (see Eq.(44)) as a function of τ with $\underset{\sim}{H}_o \parallel [111]$ and $\theta=\pi/2$ for (a) f_{1B}=12.6 kHz and (b) f_{1B}=2.43 kHz. Solid curves are calculated from Eqs.(44) and (42). Dashed curve in (b) is obtained by replacing linear $\varepsilon\tau/\tau_{AB}$ term in $F(\tau)$ with $\varepsilon[1-\exp(-(1+\varepsilon)\tau/\tau_{AB})]/(1+\varepsilon)$.

18. Plot of the B-spin free induction decay $f(\tau_o)$ as measured with the pulsed double resonance technique (see Eq.(48)), for $\underset{\sim}{H}_o \parallel [110]$, $\omega_{1B}/2\pi = 5.5$ kHz, $\tau = 25$ msec, and $N = 32$ B rf pulses. The solid curve shown is a fit of the Anderson-Weiss model to the $f(\tau_o)$ data (see Eq.(49)).

19. Experimental procedure for measuring B spin-lattice relaxation time T_{1B}, as a function of crystalline orientation. (a) shows the B-spin polarization process and varying B-spin relaxation interval t_R, while (b) shows the procedure for sampling the remaining B-spin magnetization M_{Bz} (t_R). The fixed parameters are $\theta=\pi/4$, $\omega_{eB}/2\pi = 15$ kHz and $\tau = 1$ sec, while t_R varies from 15 to 210 sec.

20. Plot of the measured spin-lattice relaxation of B-spin magnetization, for $\underset{\sim}{H}_o \parallel [111]$ and $T_L = 300°K$. The rms error bars shown are for the average of five measurements at each value of t_R, and the straight line shown is a least-squares fit to the data, yeilding $T_{1B} = 202 \pm 19$ sec.

21. Plot of measured ^{43}Ca spin-lattice relaxation time T_{1B} as a function of magnetic field orientation in the (110) plane of the crystal. The dashed lines show the average value of T_{1B} for (a) $T_L = 355°K$, $(T_{1B})_{av} = 169 \pm 25$ sec and (b) $T_L = 300°K$, $(T_{1B})_{av} = 236 \pm 27$ sec.

B.1 Model lineshape function (solid curve) plotted from Eq.(B.4) for $\lambda=1.11$ ($\xi=5.42$). For comparison a Lorentzian curve of equal half-width is also shown (dashed curve).

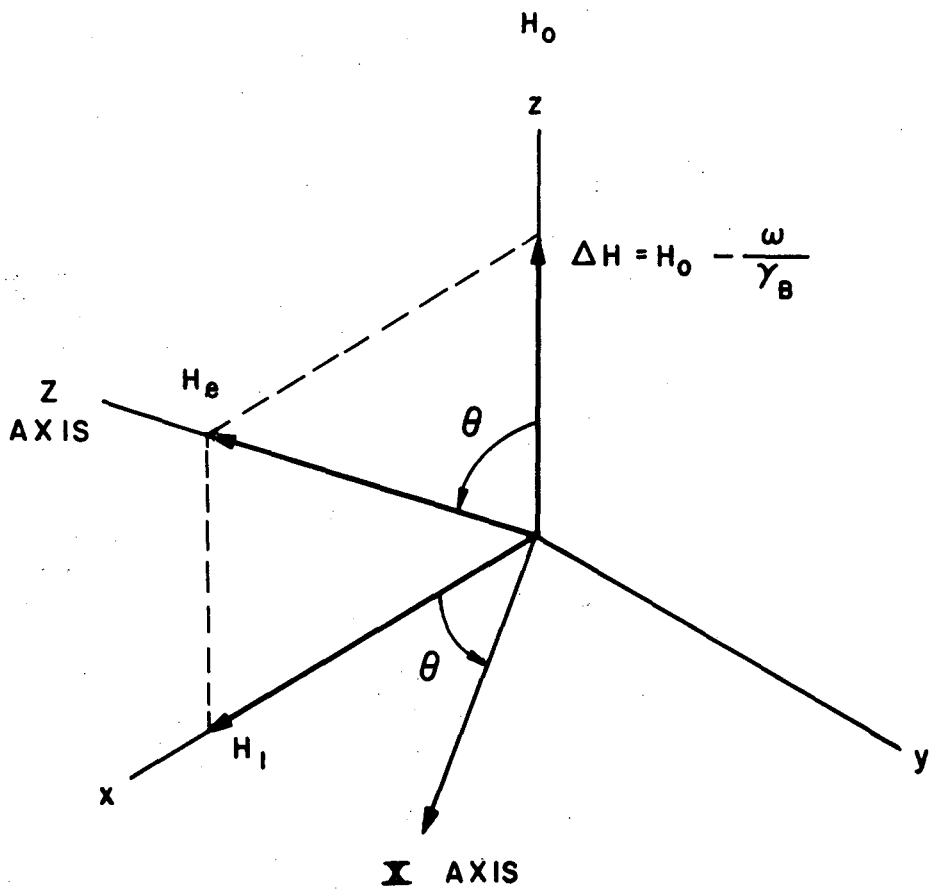
H_o
z
$\Delta H = H_o - \frac{\omega}{\gamma_B}$
Z
AXIS
H_e
θ
θ
H_1
x
y
X AXIS

FIG. 1

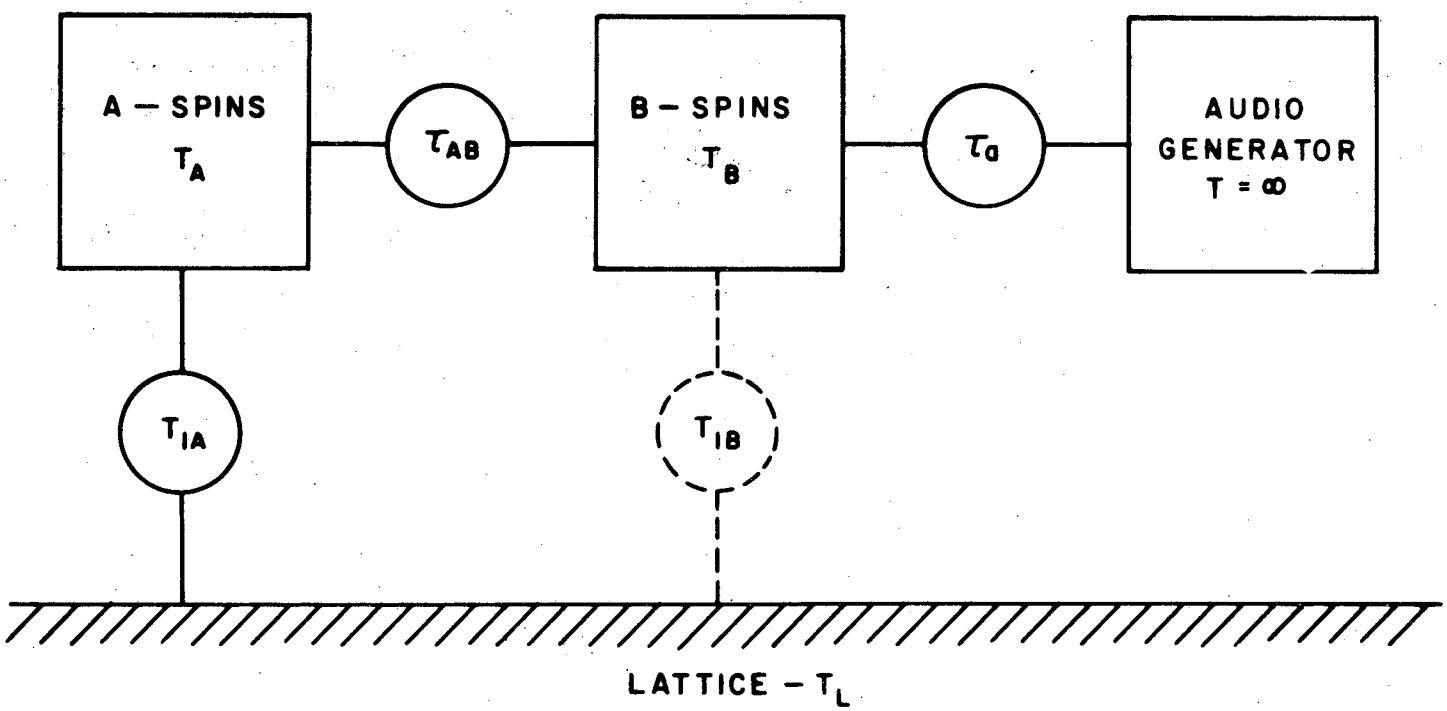
A — SPINS
T_A
τ_{AB}
B — SPINS
T_B
τ_a
AUDIO
GENERATOR
$T = \infty$
T_{1A}
T_{1B}
LATTICE — T_L

FIG. 2

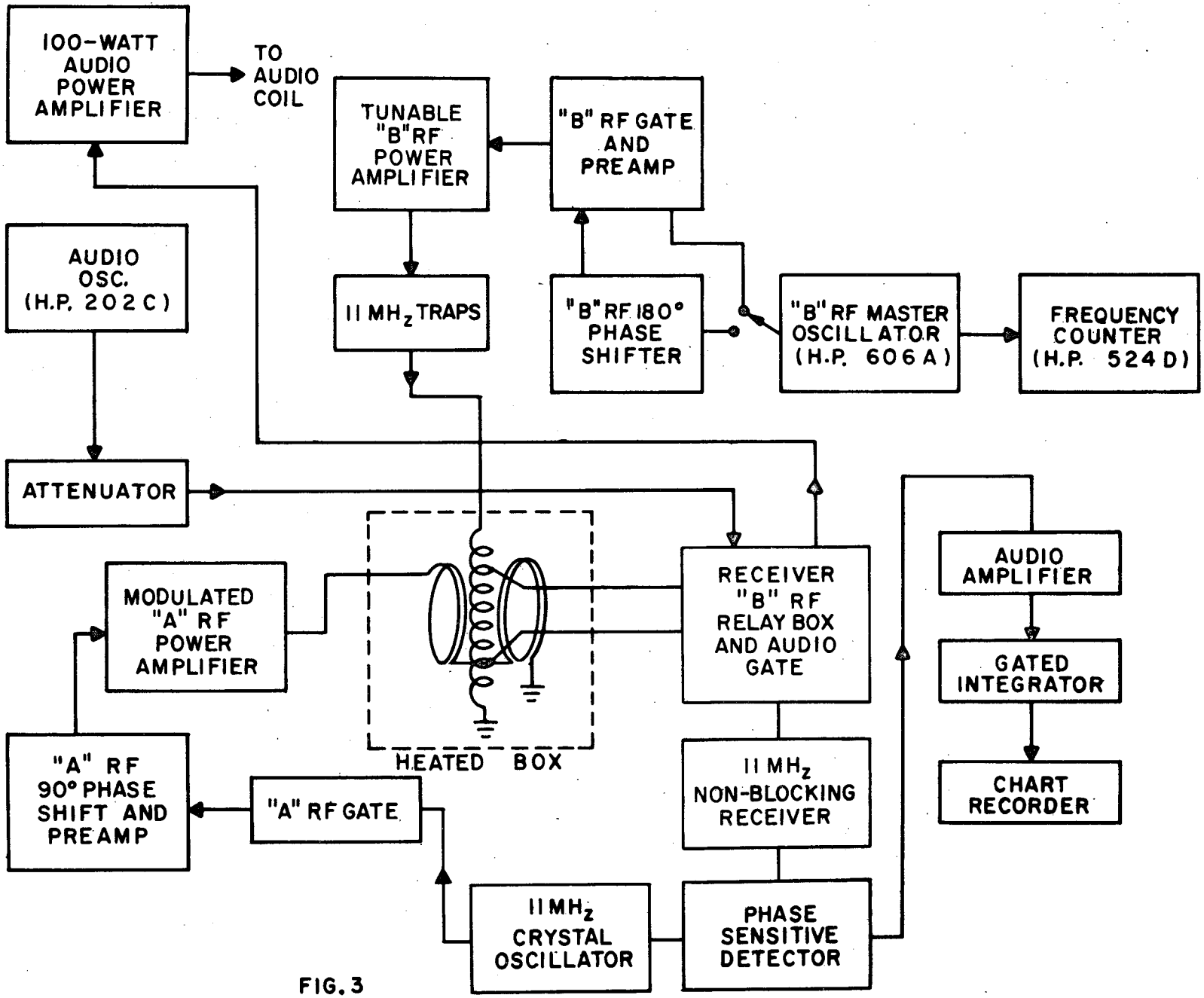
100-WATT AUDIO POWER AMPLIFIER
TO AUDIO COIL
TUNABLE "B" RF POWER AMPLIFIER
"B" RF GATE AND PREAMP
AUDIO OSC. (H.P. 202 C)
11 MHz TRAPS
"B" RF 180° PHASE SHIFTER
"B" RF MASTER OSCILLATOR (H.P. 606 A)
FREQUENCY COUNTER (H.P. 524 D)
ATTENUATOR
MODULATED "A" RF POWER AMPLIFIER
RECEIVER "B" RF RELAY BOX AND AUDIO GATE
AUDIO AMPLIFIER
GATED INTEGRATOR
CHART RECORDER
HEATED BOX
"A" RF 90° PHASE SHIFT AND PREAMP
"A" RF GATE
11 MHz NON-BLOCKING RECEIVER
11 MHz CRYSTAL OSCILLATOR
PHASE SENSITIVE DETECTOR

FIG. 3

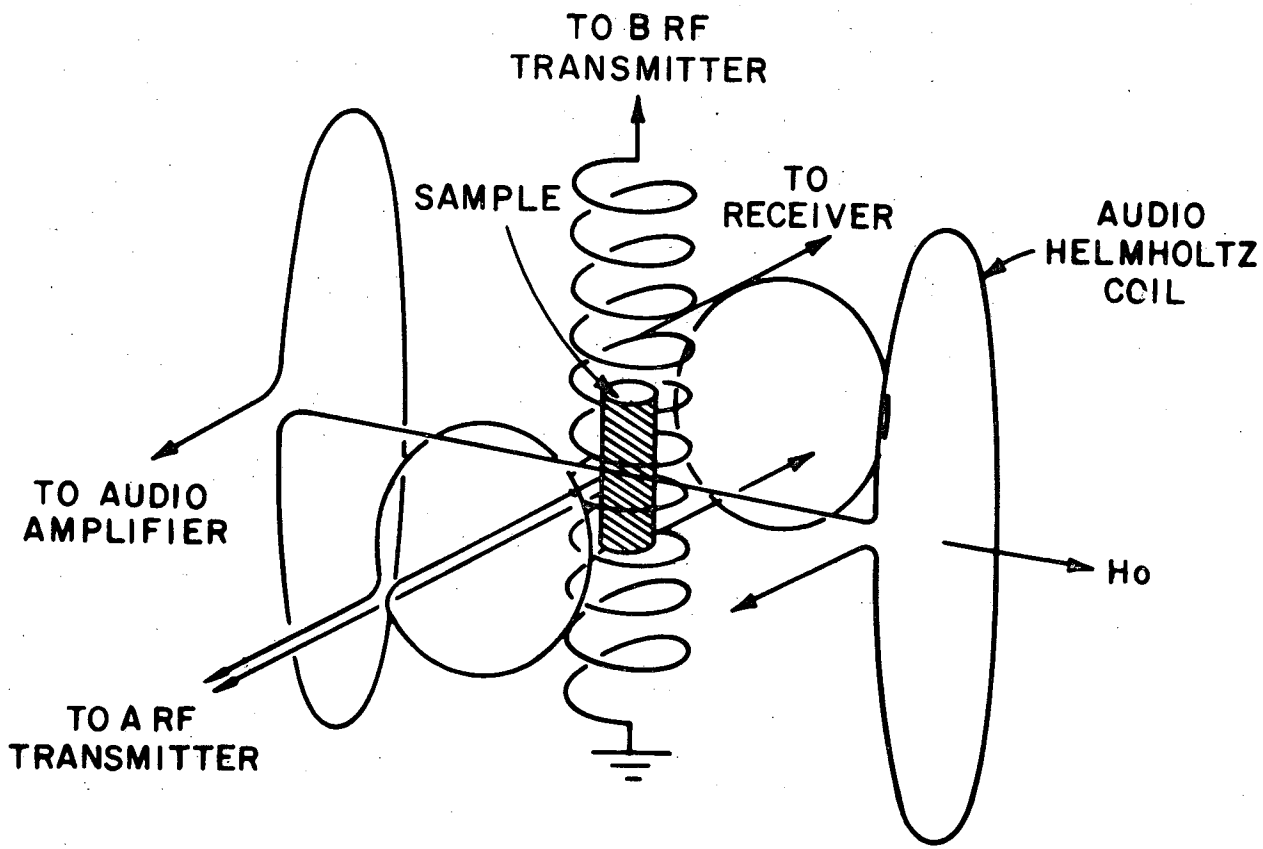
TO B RF
TRANSMITTER
SAMPLE
TO
RECEIVER
AUDIO
HELMHOLTZ
COIL
TO AUDIO
AMPLIFIER
Ho
TO A RF
TRANSMITTER

FIG. 4

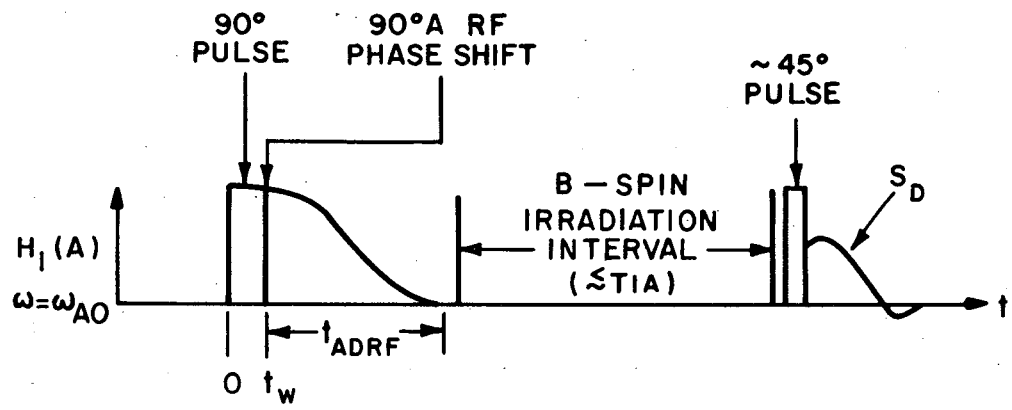
90°
PULSE
90°A RF
PHASE SHIFT
~45°
PULSE
B — SPIN
IRRADIATION
INTERVAL
(≲TIA)
S_D
H_1 (A)
$\omega=\omega_{AO}$
t_{ADRF}
0
t_w
t

FIG.5

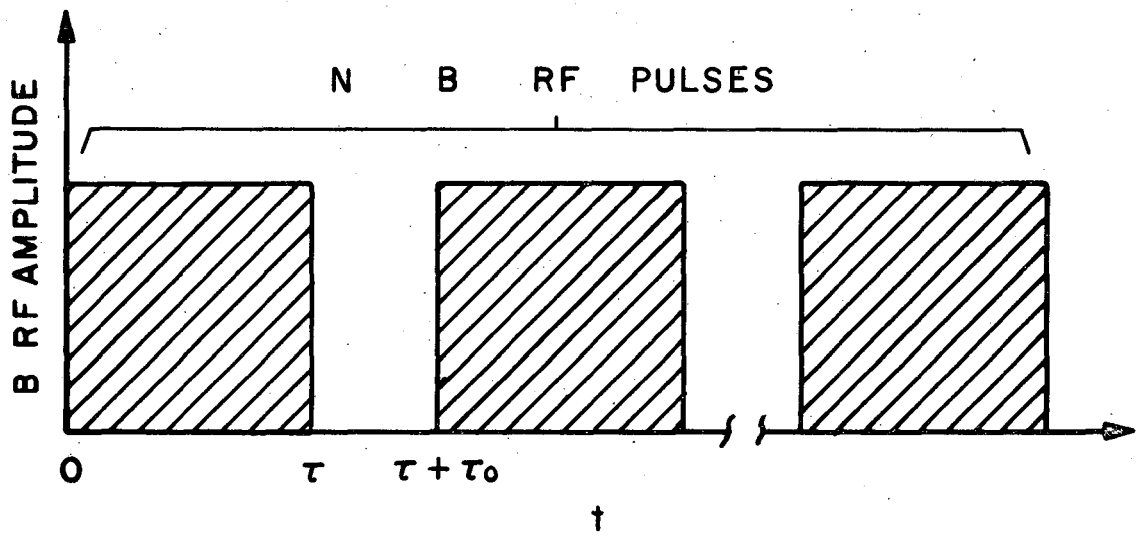

FIG. 6

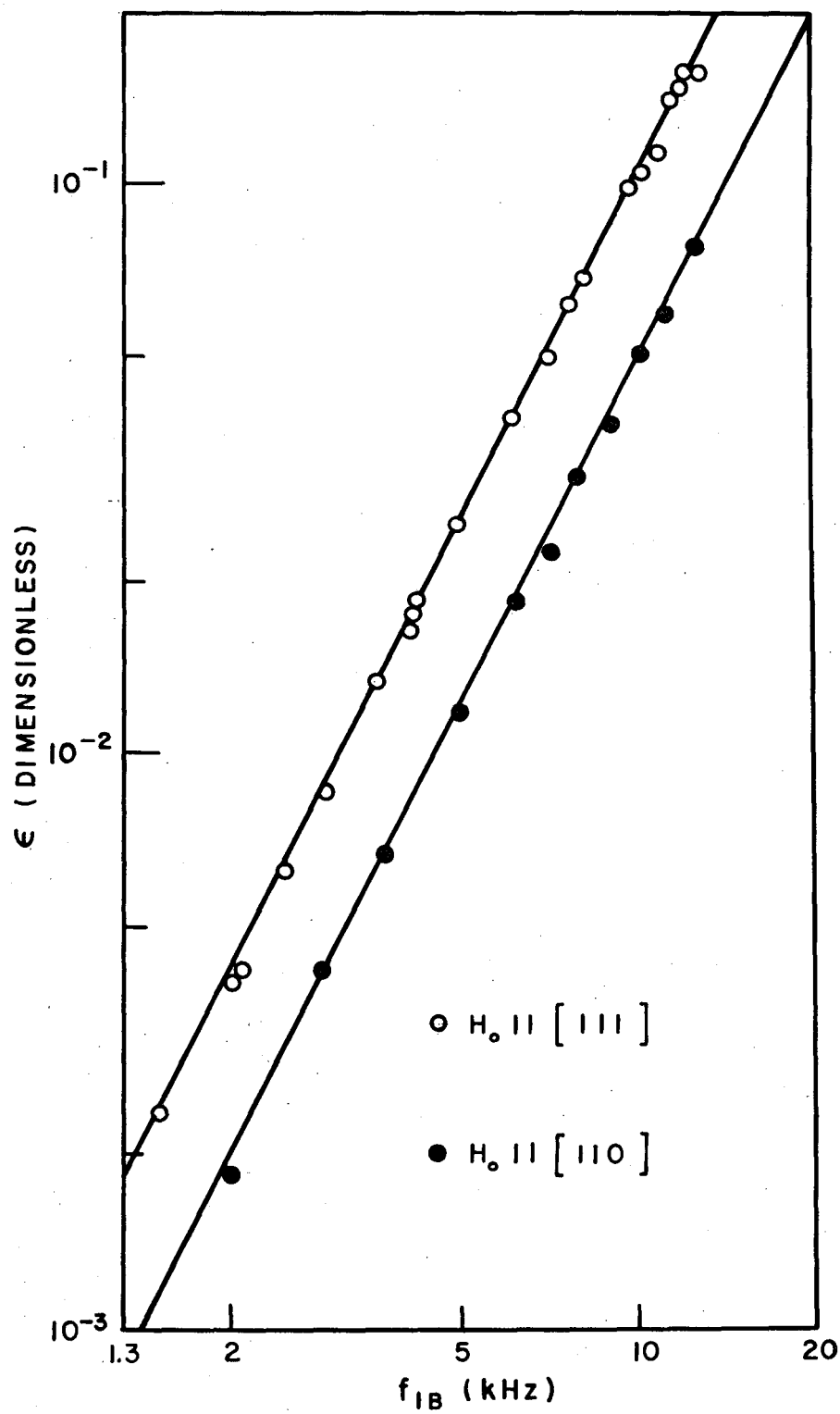
10^{-1}
10^{-2}
10^{-3}
ϵ (DIMENSIONLESS)
1.3
2
5
10
20
f_{1B} (kHz)
○ H_o ∥ [111]
● H_o ∥ [110]

FIG. 7

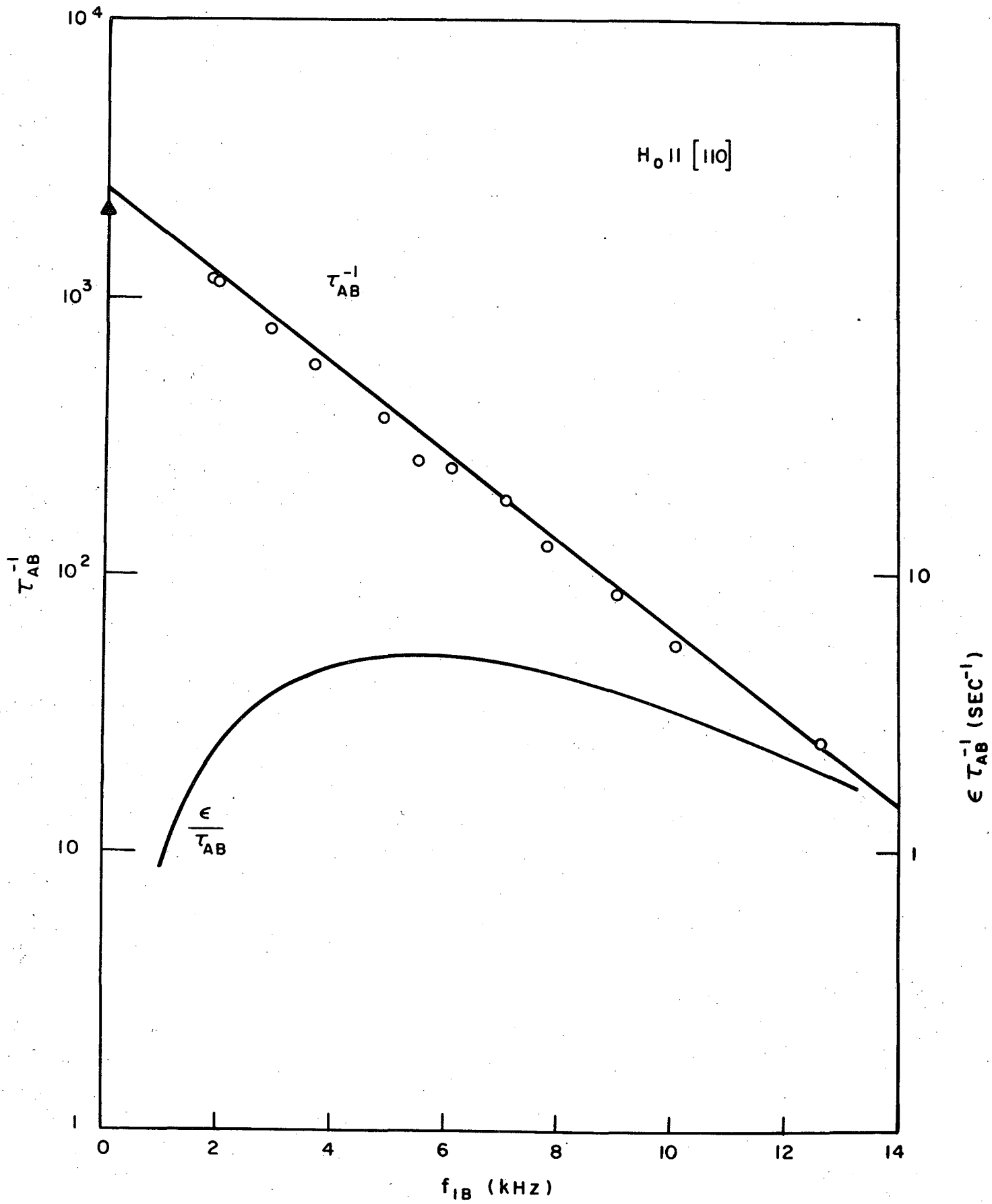
10^4
10^3
10^2
10
1
τ_{AB}^{-1}
$H_0 \parallel [110]$
τ_{AB}^{-1}
$\frac{\epsilon}{\tau_{AB}}$
10
1
$\epsilon\,\tau_{AB}^{-1}$ (SEC^{-1})
0
2
4
6
8
10
12
14
f_{1B} (kHz)

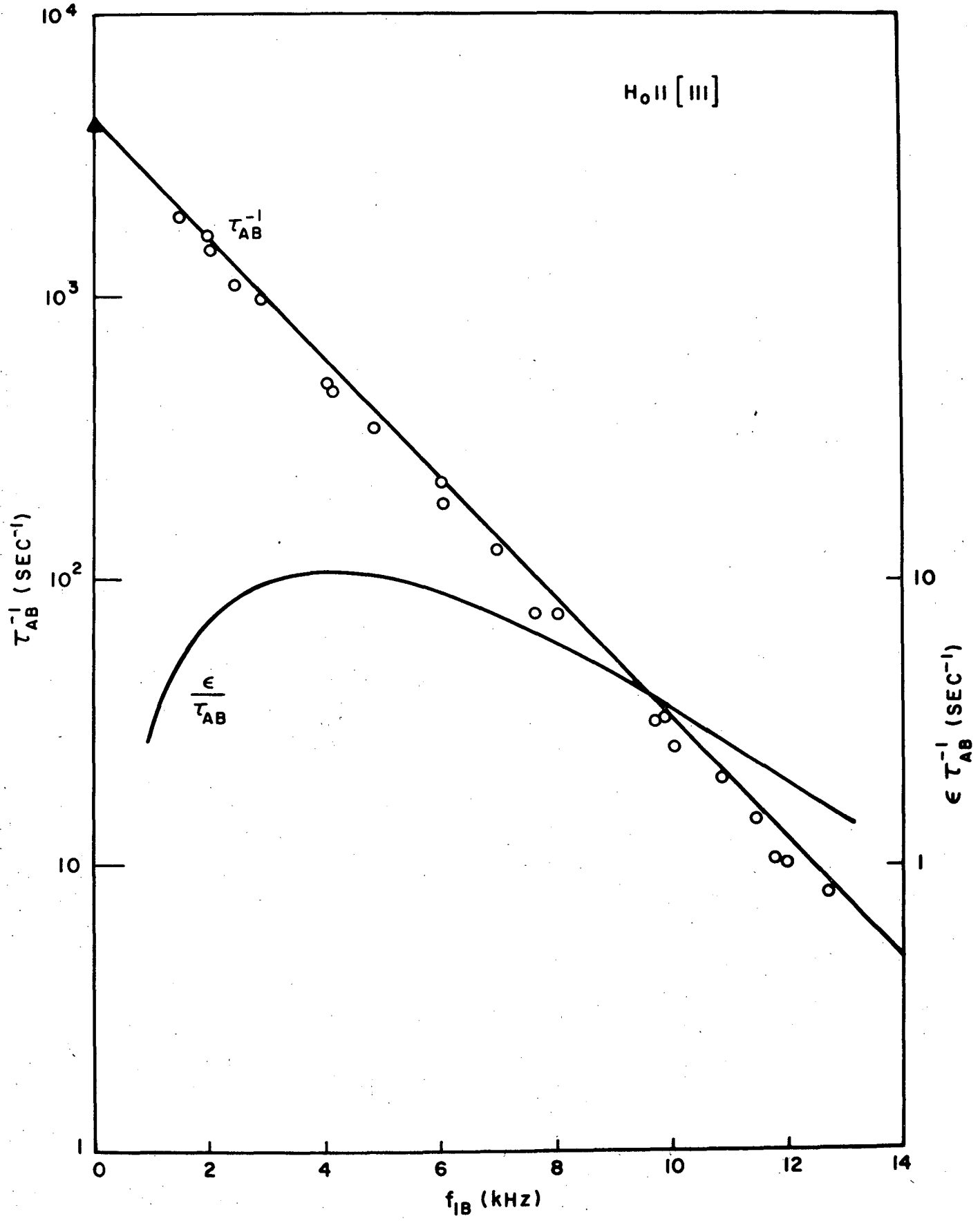
$H_0 \parallel [111]$
τ_{AB}^{-1}
$\frac{\epsilon}{\tau_{AB}}$
10^4
10^3
10^2
10
1
τ_{AB}^{-1} (SEC^{-1})
10
1
$\epsilon\,\tau_{AB}^{-1}$ (SEC^{-1})
0
2
4
6
8
10
12
14
f_{1B} (kHz)

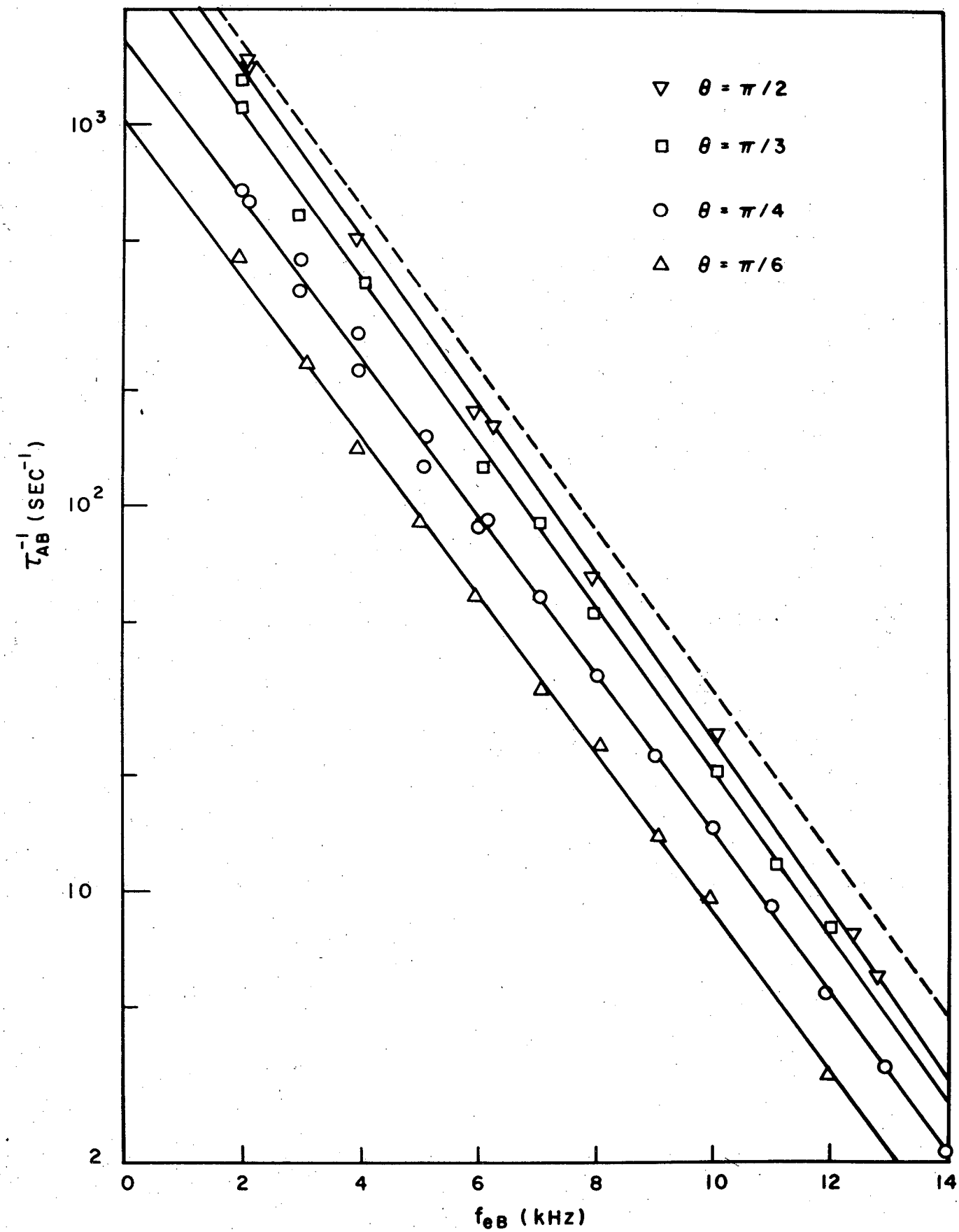
θ = π/2
θ = π/3
θ = π/4
θ = π/6
10^3
10^2
10
2
τ_{AB}^{-1} (SEC^{-1})
0
2
4
6
8
10
12
14
f_{eB} (kHz)

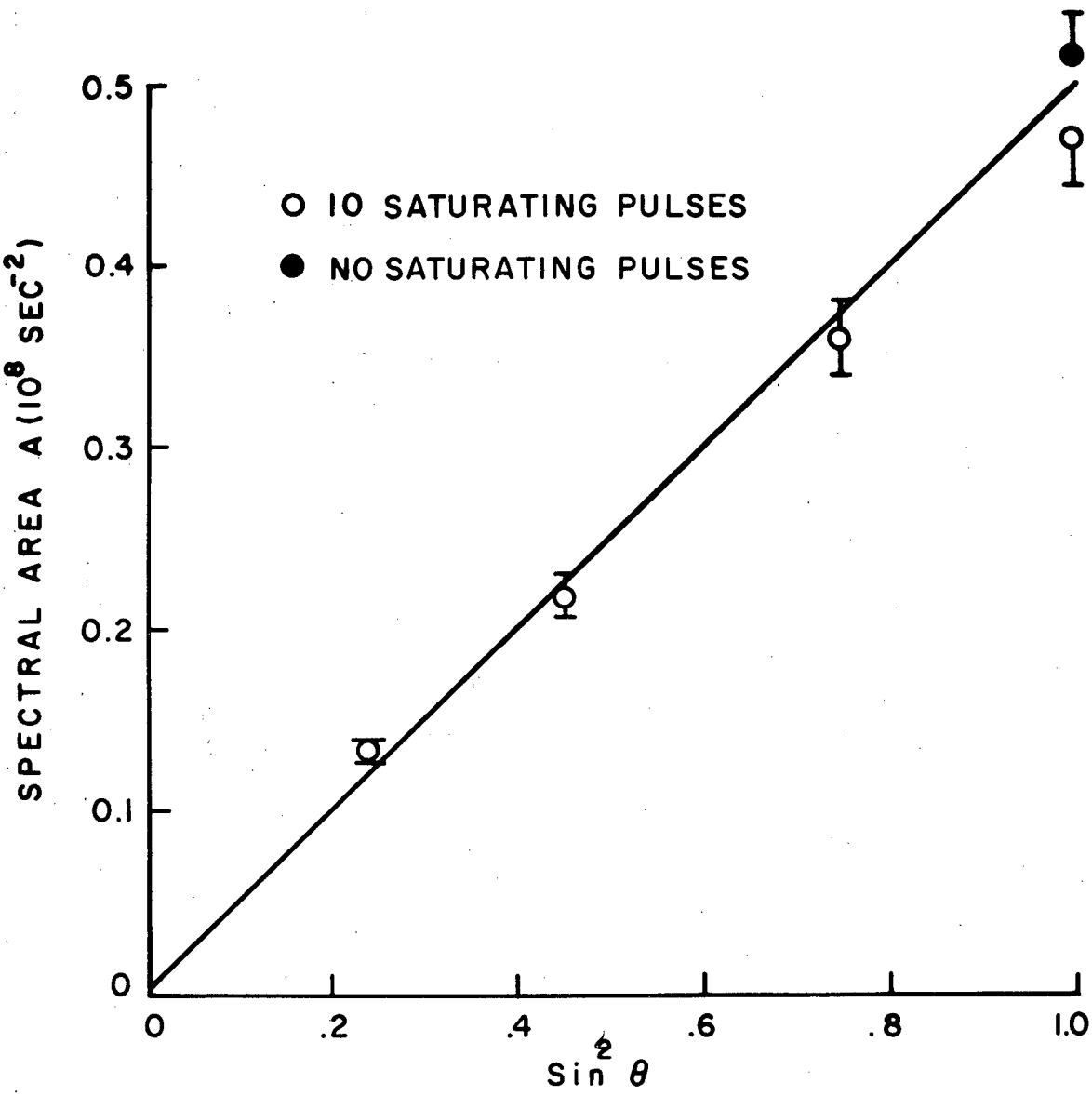
0.5
0.4
0.3
0.2
0.1
0
SPECTRAL AREA A (10^8 SEC^{-2})
O 10 SATURATING PULSES
● NO SATURATING PULSES
0
.2
.4
.6
.8
1.0
Sin^2 θ

FIG. 10

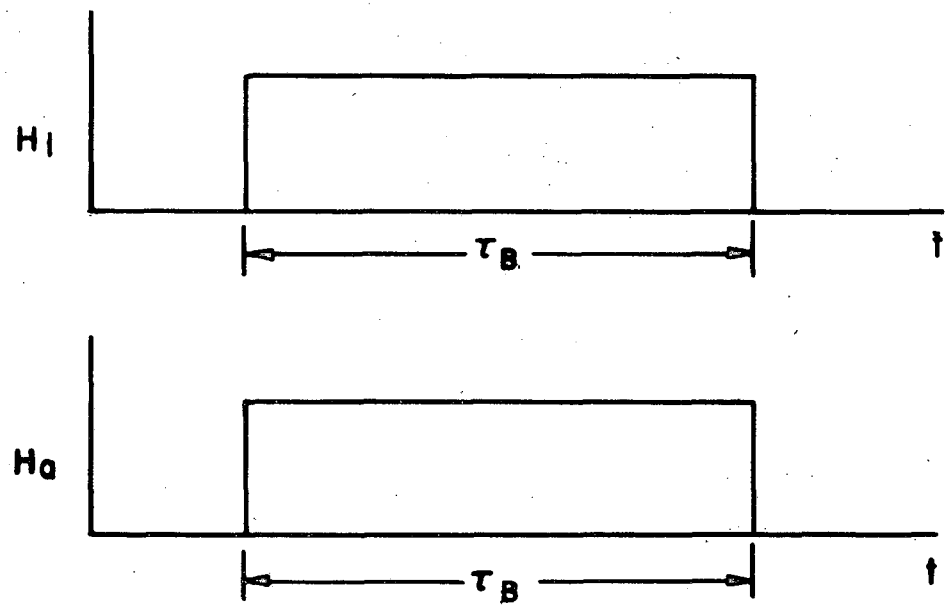

FIG. 11

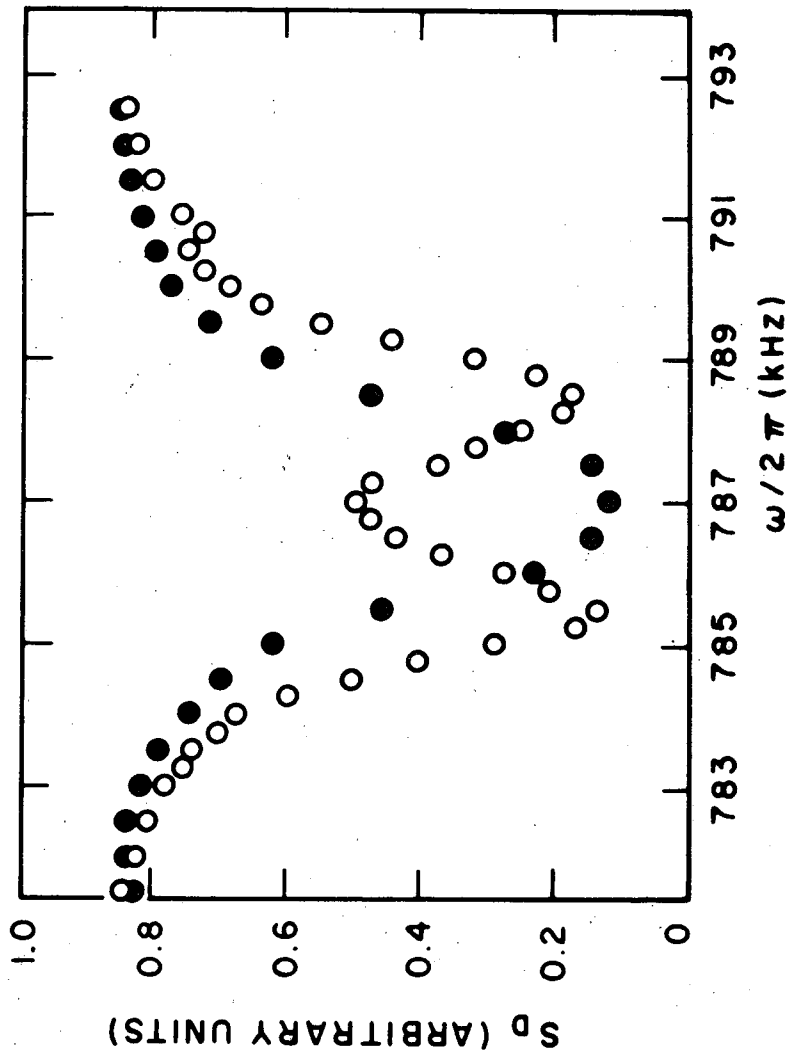
1.0
0.8
0.6
0.4
0.2
0
S_D (ARBITRARY UNITS)
783
785
787
789
791
793
$\omega/2\pi$ (kHz)

FIG. 12

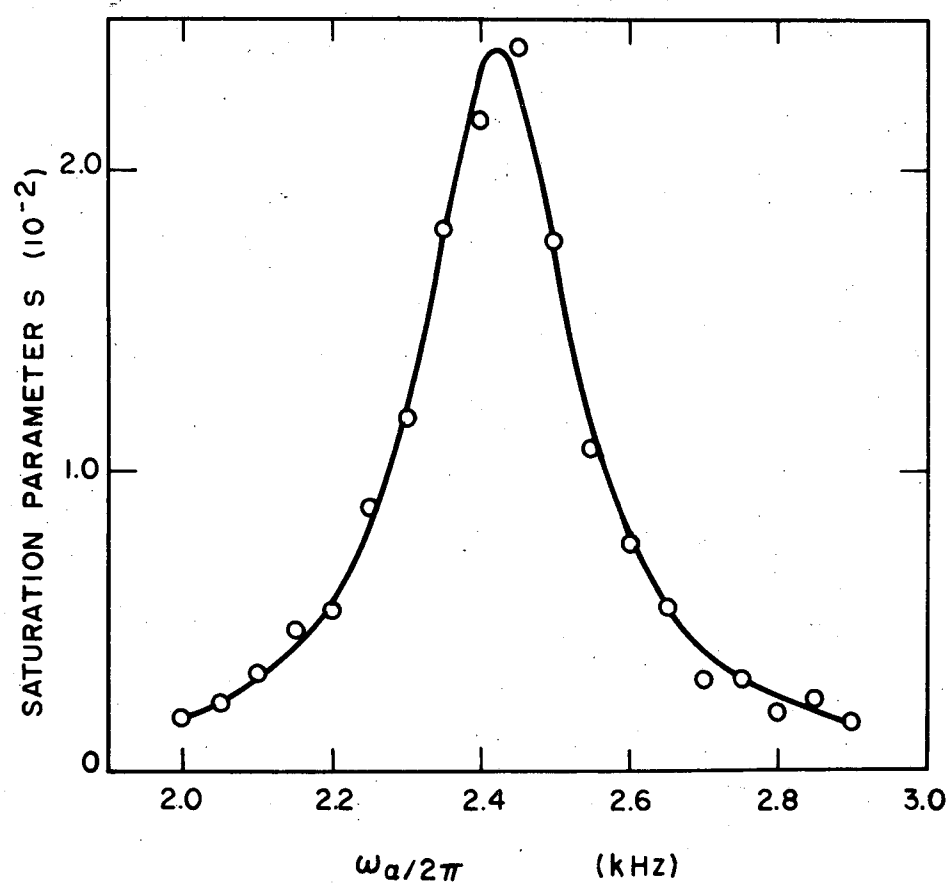
SATURATION PARAMETER S (10^{-2})
2.0
1.0
0
2.0
2.2
2.4
2.6
2.8
3.0
$\omega_a/2\pi$ (kHz)

FIG. 13

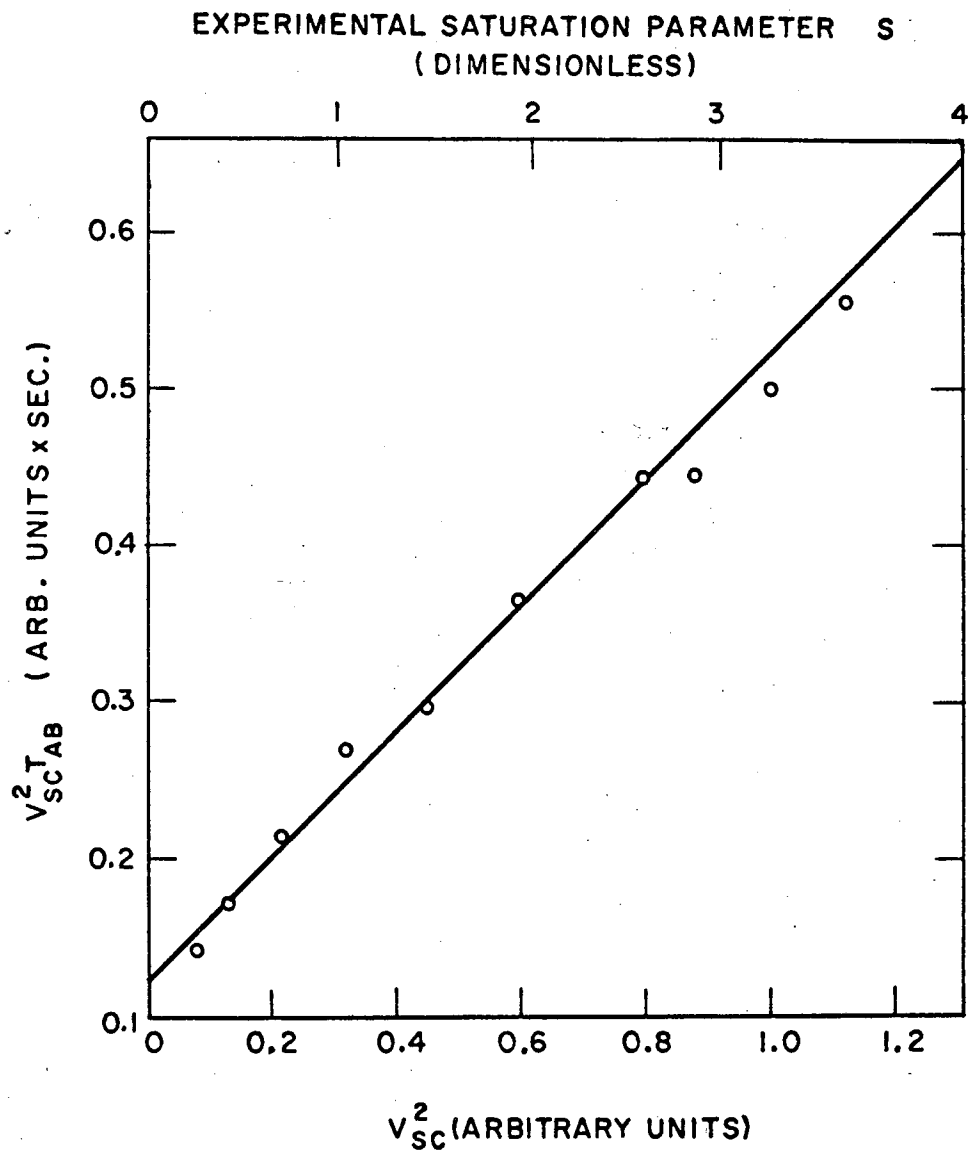
EXPERIMENTAL SATURATION PARAMETER S
(DIMENSIONLESS)
0
1
2
3
4
0.6
0.5
0.4
0.3
0.2
0.1
$V_{SC}^2 T_{AB}$ (ARB. UNITS x SEC.)
0
0.2
0.4
0.6
0.8
1.0
1.2
V_{SC}^2 (ARBITRARY UNITS)

FIG. 14

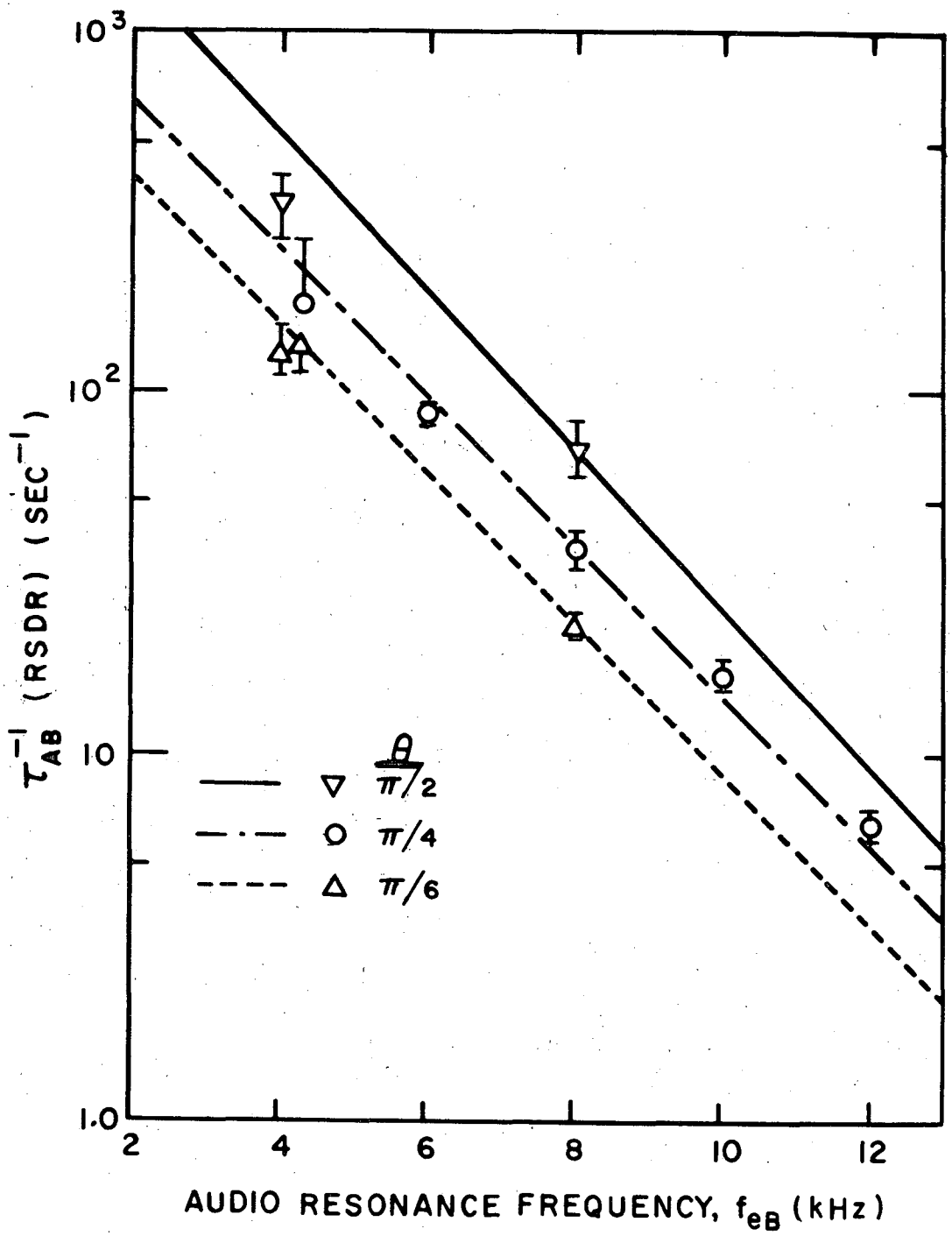
10^3
10^2
10
1.0
τ_{AB}^{-1} (RSDR) (SEC^{-1})
2
4
6
8
10
12
AUDIO RESONANCE FREQUENCY, f_{eB} (kHz)
θ
$\pi/2$
$\pi/4$
$\pi/6$

FIG. 15

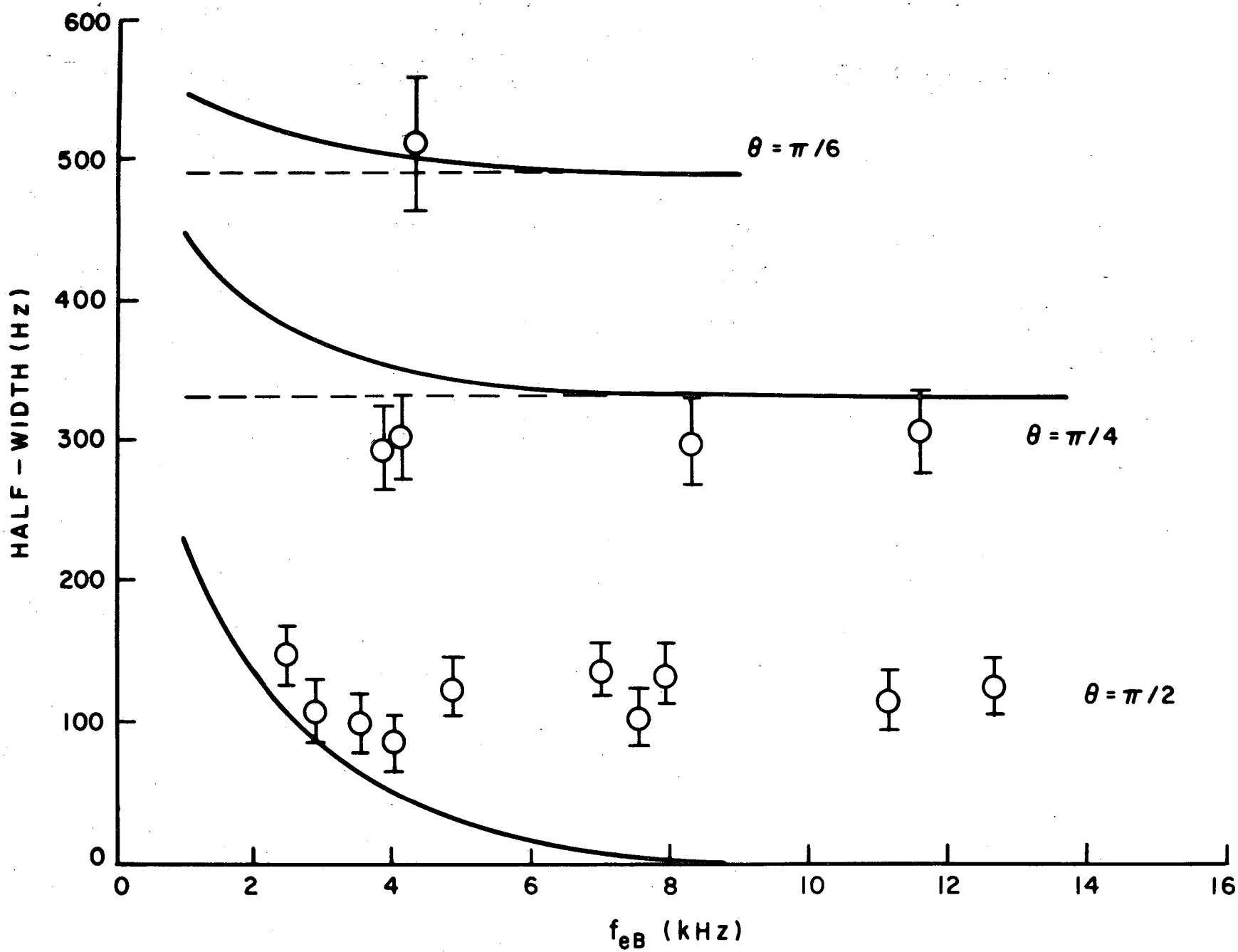
600
500
400
300
200
100
0
HALF - WIDTH (Hz)
0
2
4
6
8
10
12
14
16
f_{eB} (kHz)
$\theta = \pi/6$
$\theta = \pi/4$
$\theta = \pi/2$

FIG. 16

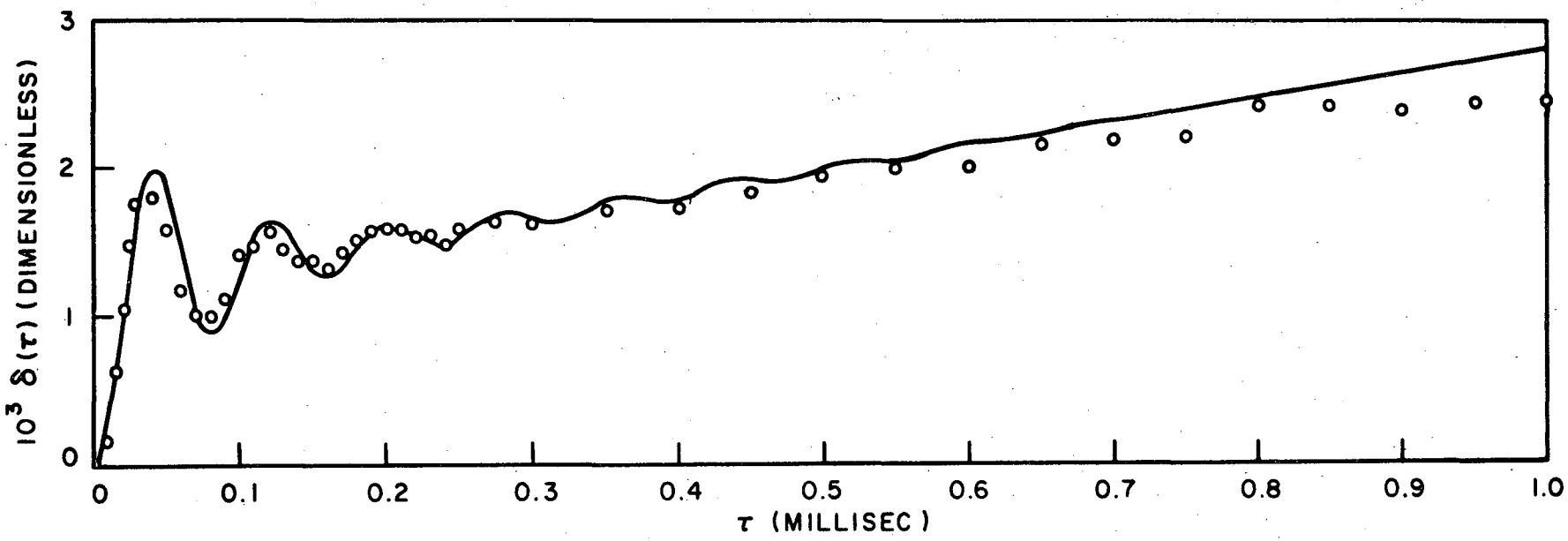
3
2
1
0
$10^3\ \delta(\tau)$ (DIMENSIONLESS)
0
0.1
0.2
0.3
0.4
0.5
0.6
0.7
0.8
0.9
1.0
τ (MILLISEC)

FIG. 17a

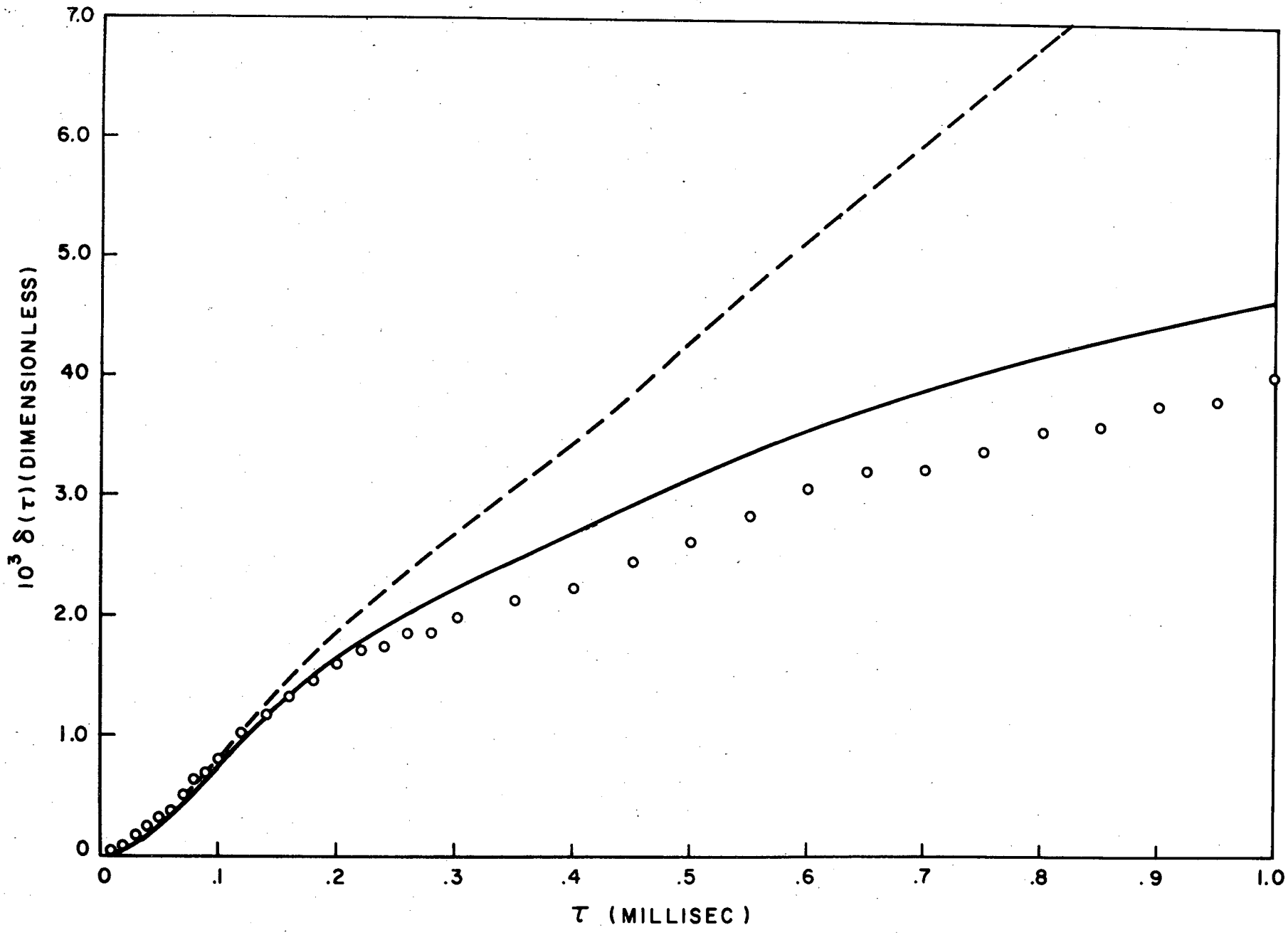
7.0
6.0
5.0
40
3.0
2.0
1.0
0
$10^3\,\delta(\tau)$ (DIMENSIONLESS)
0
.1
.2
.3
.4
.5
.6
.7
.8
.9
1.0
τ (MILLISEC)

FIG. 17b

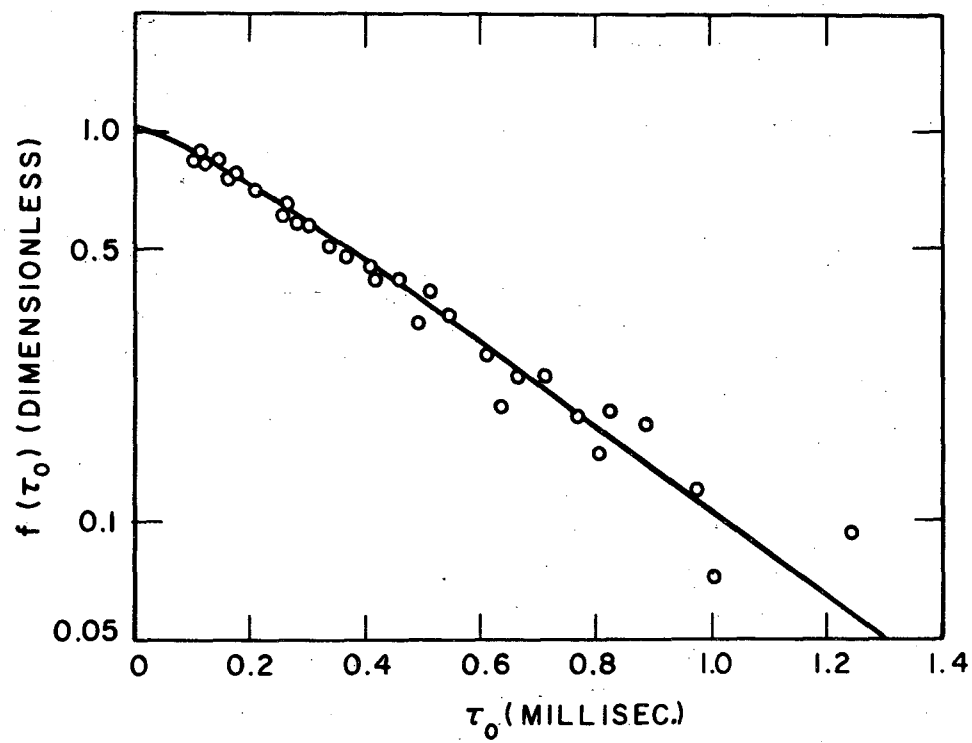
1.0
0.5
0.1
0.05
f (τ_0) (DIMENSIONLESS)
0
0.2
0.4
0.6
0.8
1.0
1.2
1.4
τ_0 (MILLISEC.)

FIG. 18

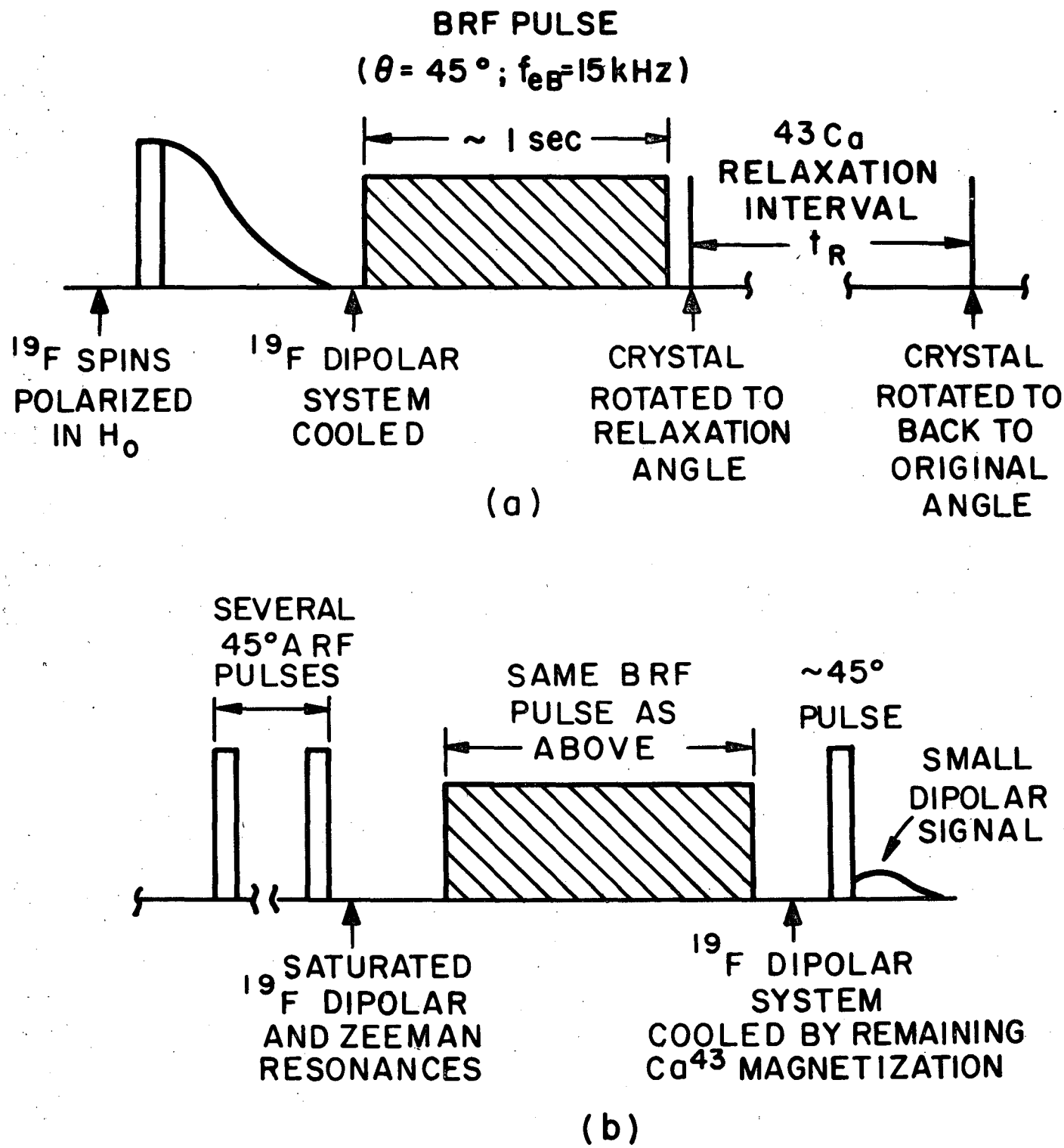
BRF PULSE
(θ = 45°; f_eB = 15 kHz)
~ 1 sec
43 Ca
RELAXATION
INTERVAL
t_R
19F SPINS
POLARIZED
IN H_0
19F DIPOLAR
SYSTEM
COOLED
CRYSTAL
ROTATED TO
RELAXATION
ANGLE
CRYSTAL
ROTATED TO
BACK TO
ORIGINAL
ANGLE
(a)
SEVERAL
45° A RF
PULSES
SAME BRF
PULSE AS
ABOVE
~45°
PULSE
SMALL
DIPOLAR
SIGNAL
19 SATURATED
F DIPOLAR
AND ZEEMAN
RESONANCES
19 F DIPOLAR
SYSTEM
COOLED BY REMAINING
Ca43 MAGNETIZATION
(b)

FIG. 19

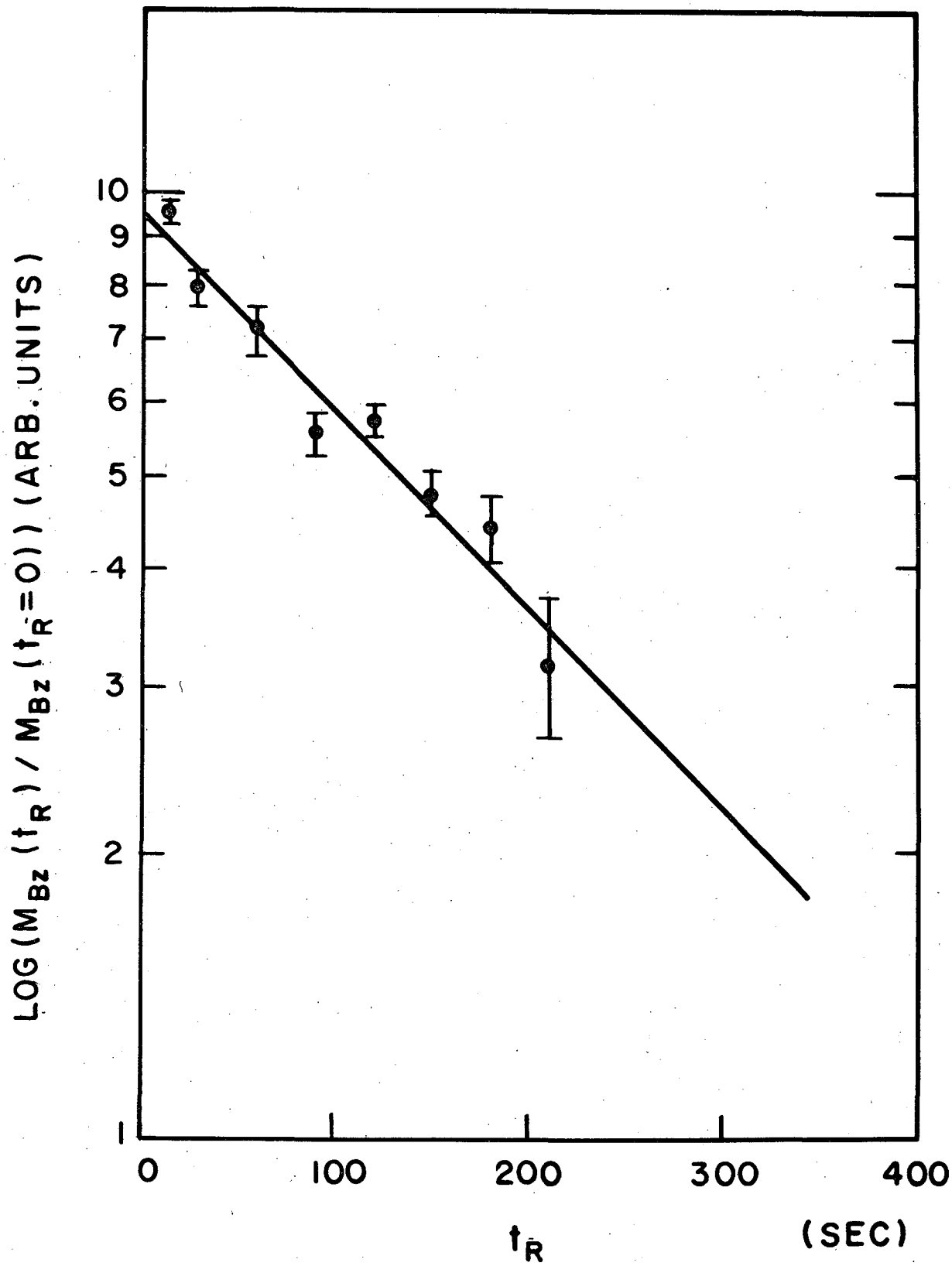
LOG (M_Bz (t_R) / M_Bz (t_R=0)) (ARB. UNITS)
10
9
8
7
6
5
4
3
2
1
0
100
200
300
400
t_R
(SEC)

FIG. 20

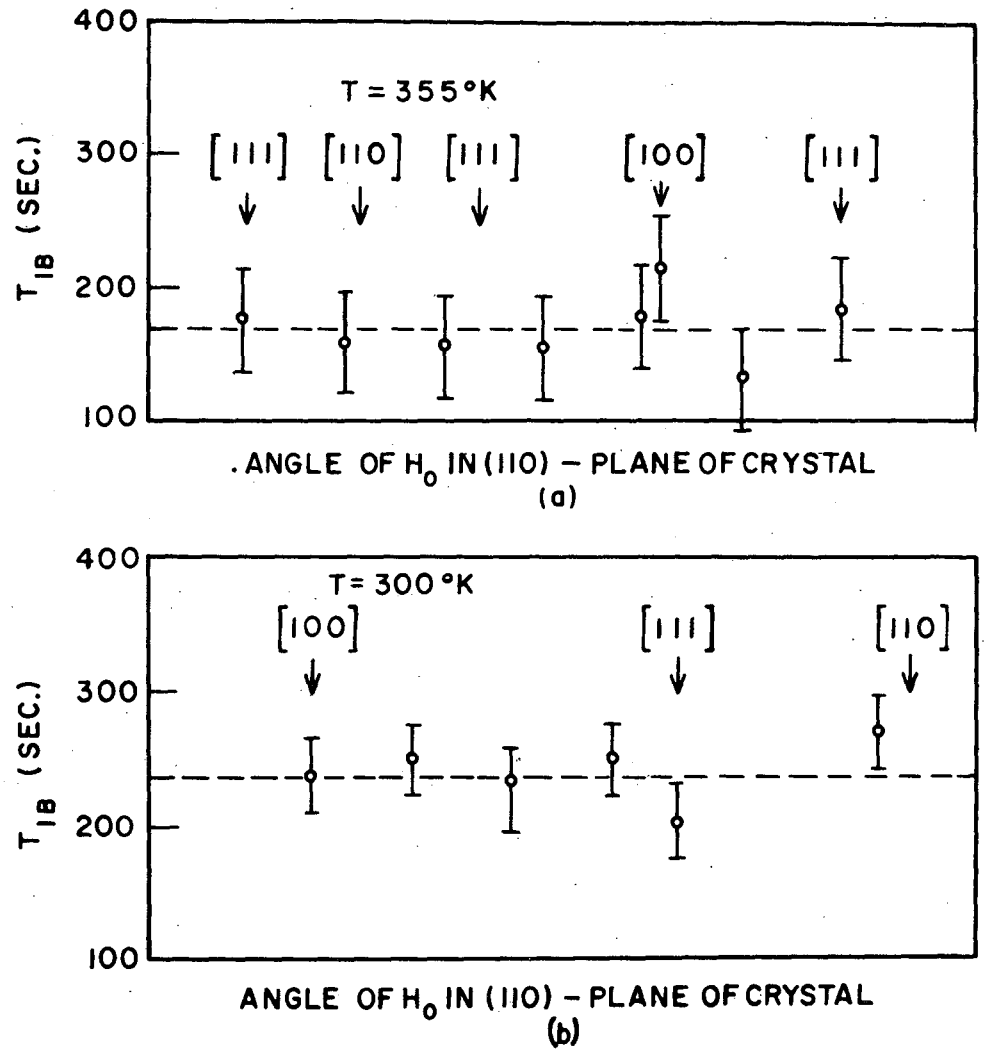
400
300
200
100
T_{1B} (SEC.)
T = 355 °K
[111]
[110]
[111]
[100]
[111]
ANGLE OF H_0 IN (110) – PLANE OF CRYSTAL
(a)
400
300
200
100
T_{1B} (SEC.)
T = 300 °K
[100]
[111]
[110]
ANGLE OF H_0 IN (110) – PLANE OF CRYSTAL
(b)

FIG. 21

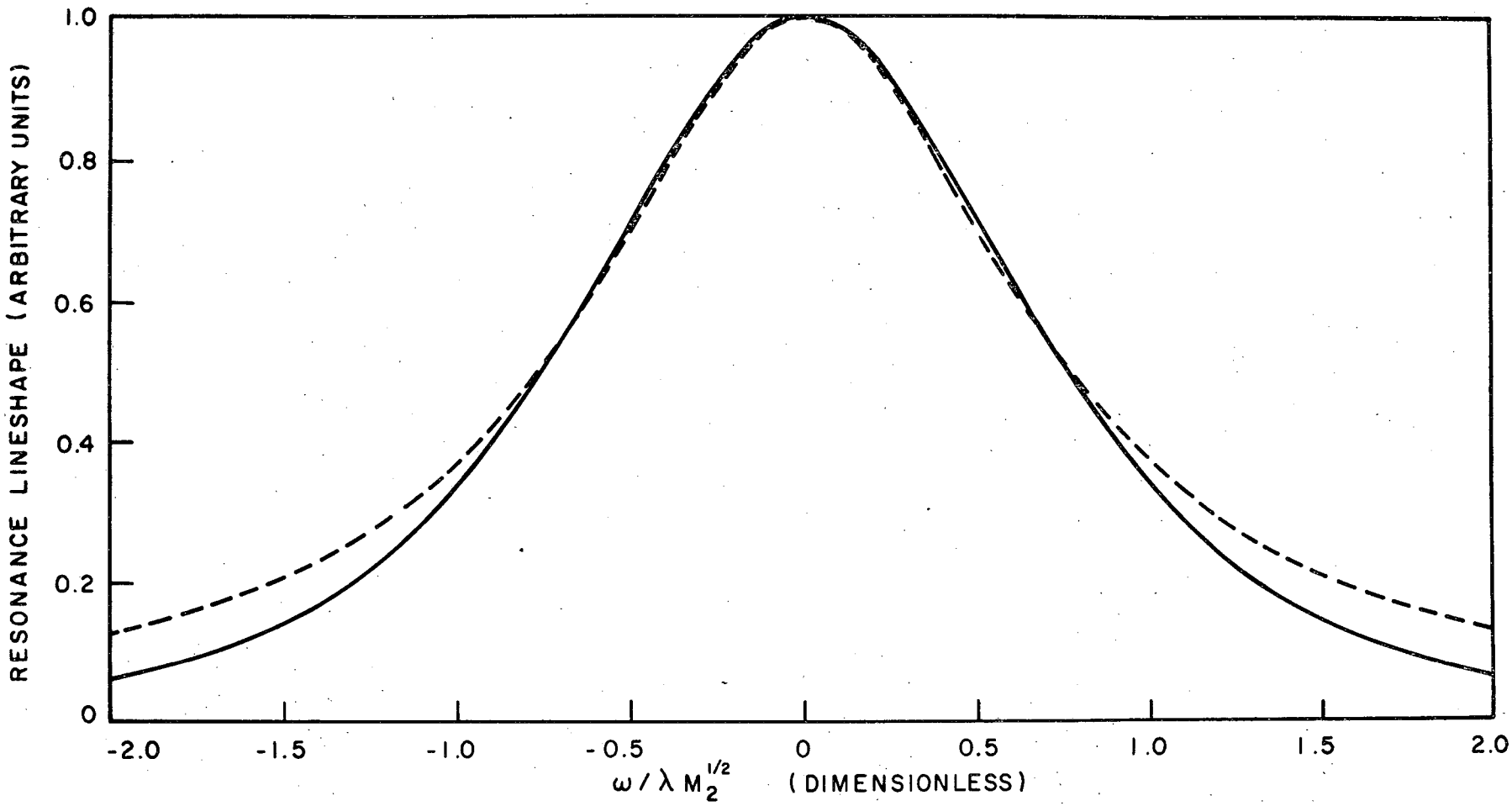
RESONANCE LINESHAPE (ARBITRARY UNITS)
1.0
0.8
0.6
0.4
0.2
0
-2.0
-1.5
-1.0
-0.5
0
0.5
1.0
1.5
2.0
$\omega / \lambda M_2^{1/2}$ (DIMENSIONLESS)

FIG. B.1

LEGAL NOTICE

This report was prepared as an account of Government sponsored work. Neither the United States, nor the Commission, nor any person acting on behalf of the Commission:

A. Makes any warranty or representation, expressed or implied, with respect to the accuracy, completeness, or usefulness of the information contained in this report, or that the use of any information, apparatus, method, or process disclosed in this report may not infringe privately owned rights; or

B. Assumes any liabilities with respect to the use of, or for damages resulting from the use of any information, apparatus, method, or process disclosed in this report.

As used in the above, "person acting on behalf of the Commission" includes any employee or contractor of the Commission, or employee of such contractor, to the extent that such employee or contractor of the Commission, or employee of such contractor prepares, disseminates, or provides access to, any information pursuant to his employment or contract with the Commission, or his employment with such contractor.

TECHNICAL INFORMATION DIVISION
LAWRENCE RADIATION LABORATORY
UNIVERSITY OF CALIFORNIA
BERKELEY, CALIFORNIA 94720